



POWER GENERATION BY HARVESTING  
AMBIENT ENERGY WITH A  
MICRO-ELECTROMAGNETIC GENERATOR

THESIS

James Shields, Captain, USAF

AFIT/GE/ENG/09-42

DEPARTMENT OF THE AIR FORCE  
AIR UNIVERSITY

**AIR FORCE INSTITUTE OF TECHNOLOGY**

Wright-Patterson Air Force Base, Ohio

APPROVED FOR PUBLIC RELEASE; DISTRIBUTION UNLIMITED.

The views expressed in this thesis are those of the author and do not reflect the official policy or position of the United States Air Force, Department of Defense, or the United States Government.

POWER GENERATION BY HARVESTING  
AMBIENT ENERGY WITH A  
MICRO-ELECTROMAGNETIC GENERATOR

THESIS

Presented to the Faculty  
Department of Electrical and Computer Engineering  
Graduate School of Engineering and Management  
Air Force Institute of Technology  
Air University  
Air Education and Training Command  
In Partial Fulfillment of the Requirements for the  
Degree of Master of Science in Electrical Engineering

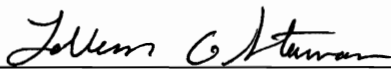
James Shields, B.S.C.E.  
Captain, USAF

March 2009

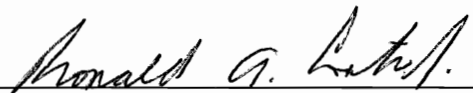
POWER GENERATION BY HARVESTING  
AMBIENT ENERGY WITH A  
MICRO-ELECTROMAGNETIC GENERATOR

James Shields, B.S.C.E.  
Captain, USAF

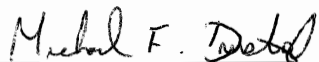
Approved:

  
LaVern A. Starman, PhD, Maj, USAF  
(Chairman)


26 Feb 09  
date

  
Ronald A. Coutu, Jr., PhD, Lt Col,  
USAF (Member)

24 Feb 09  
date

  
Michael F. Durstock, PhD (Member)

24 Feb 09  
date

  
Nancy Kelley-Loughane, PhD (Member)

24 Feb 09  
date

*Abstract*

This thesis investigated the potential power output of a micro-electromagnetic generator fabricated using typical microfabrication materials and techniques. The design was based on a desire to free bio-implanted or remote electronic devices from batteries and their finite power supplies. A micro-electromagnetic generator could harvest energy from the ambient environment and power such devices indefinitely. Designs for the stator coil and rotor magnet components of the generator were optimized to produce maximum current density based upon electromagnetic theory. The relative orientation of the coil to the rotor and material selection for each component were considered. Coils were fabricated using low-resistance gold. A method for overlaying two evaporated gold wires was devised and successfully fabricated in order to avoid side-wall thinning of the coils which has been shown to lead to high resistivities. Rotors were made with nickel, a ferromagnetic material. The required parameters for reduced stress plating using a nickel electroplating bath were investigated in order to pattern and deposit nickel for the rotors. Once fabricated, the rotors were magnetized through the use of an electromagnet. In addition, a testing apparatus that provided precise alignment, a method of rotation to simulate operational functionality, and power measurement capabilities was designed and assembled. Testing of the magnets showed that the nickel rotors were able to be highly magnetized when placed near a strong field. However, upon removal from the field the magnetization quickly dissipated. It was determined that the coercivity, or magnetic hardness, of electroplated nickel was too low for the rotor magnets to retain a field for any appreciable amount of time. Testing of the micro-generator revealed that power output did not exceed  $2\text{ nA}$ , which was expected given that the magnetic rotors did not retain their flux density. It was shown that nickel does not maintain the flux density required for a micro-electromagnetic generator and different materials should be investigated.

## *Acknowledgements*

First and foremost, I would like to express my gratitude and appreciation for my wife and my children for their patience and support during this thesis effort. I would also like to formally thank my thesis advisor, Maj. LaVern Starman, and my thesis committee members, Lt. Col. Ron Coutu, Dr. Michael Durstock and Dr. Nancy Kelley-Loughnane, for their guidance and insight. In addition, individuals at AFIT, AFRL/Sensors Directorate, and AFRL/Propulsion Directorate who provided support with fabrication and testing were invaluable, namely: Rich Johnston, Kevin Leedy, Capt Kelson Chabak, Paul Cassity, Larry Callahan, and Dr. Zafer Turgut. Finally, my fellow students were a tremendous asset to discuss ideas and provide critiques of my work. Thanks to all of them as well: Nick Coleman, Dan Gallagher, Adam Gubbels, Moe Kossler, Tom Lagoski, Tod Laurvick, Mimi Ledet and Luke Rederus.

James Shields

# Table of Contents

	Page
Abstract . . . . .	iv
Acknowledgements . . . . .	v
Table of Contents . . . . .	vi
List of Figures . . . . .	ix
List of Tables . . . . .	xii
List of Abbreviations . . . . .	xiii
I. Introduction . . . . .	1
1.1 Ambient Energy Harvesting . . . . .	1
1.2 Microelectromechanical Systems (MEMS) . . . . .	2
1.3 Problem Overview . . . . .	4
1.4 Research Intent . . . . .	5
1.5 Organization of Thesis . . . . .	6
II. Literature Review . . . . .	8
2.1 From Batteries to Harvesters . . . . .	8
2.2 Micro-Scale Energy Harvesting Research . . . . .	9
2.2.1 Electromagnetic Power Generation . . . . .	11
2.2.2 Piezoelectric Power Generation . . . . .	12
2.2.3 Electrostatic Power Generation . . . . .	14
2.2.4 Previous AFIT Research . . . . .	16
2.3 Identified Challenges . . . . .	16
2.4 Chapter Summary . . . . .	19
III. Methodology and Theory . . . . .	20
3.1 Electromagnetic Generators . . . . .	20
3.1.1 Theory of Electromagnetic Generators . . . . .	21
3.1.2 Generator Design Parameters . . . . .	22
3.2 Magnet Design . . . . .	23
3.2.1 Magnetic Material Selection . . . . .	24
3.2.2 Magnet Layout Design . . . . .	26
3.2.3 Nickel Deposition Process . . . . .	28
3.2.4 Magnetization of Nickel Deposit . . . . .	31

	Page
3.3 Coil Design . . . . .	33
3.3.1 Coil Material Selection . . . . .	33
3.3.2 Coil Layout . . . . .	34
3.4 Test Structure . . . . .	41
3.4.1 Rotation Mechanism . . . . .	41
3.4.2 Precise Alignment . . . . .	41
3.4.3 Power Output Measurement . . . . .	42
3.5 Chapter Summary . . . . .	43
IV. Fabrication . . . . .	44
4.1 Mask Fabrication and Substrate Selection . . . . .	44
4.2 Magnet Fabrication . . . . .	45
4.2.1 Photoresist Characterization . . . . .	45
4.2.2 Nickel Plating . . . . .	47
4.2.3 Magnetization . . . . .	57
4.3 Coil Fabrication . . . . .	57
4.3.1 Runner . . . . .	58
4.3.2 Dielectric . . . . .	61
4.3.3 Coil . . . . .	61
4.4 Test Structure Assembly . . . . .	63
4.5 Chapter Summary . . . . .	66
V. Testing and Results . . . . .	68
5.1 Rotor Magnets . . . . .	68
5.2 Stator Coils . . . . .	71
5.3 Testing Apparatus . . . . .	72
5.4 Micro-Generator . . . . .	75
5.5 Chapter Summary . . . . .	75
VI. Conclusions . . . . .	76
6.1 Scientific Contributions . . . . .	76
6.2 Lessons Learned and Recommendations . . . . .	76
6.2.1 Sample Selection . . . . .	76
6.2.2 LOR for Runner Deposit . . . . .	77
6.2.3 Use of a High Precision Rotary Stage . . . . .	77
6.2.4 Electromagnetic Modeling Tools . . . . .	77
6.2.5 Magnetic Material Selection . . . . .	77
6.2.6 Turbine Integration, Packaging and Power Con- conditioning . . . . .	78
6.2.7 Piezoelectric Research . . . . .	78
6.3 Conclusion . . . . .	79

	Page
Appendix A.     Supporting Calculations . . . . .	80
Appendix B.     Lithographic Mask Design . . . . .	82
Appendix C.     Fabrication Methods . . . . .	90
Appendix D.     Experimental Raw Data . . . . .	94
Bibliography . . . . .	98
Vita . . . . .	100

## *List of Figures*

Figure		Page
1.1.	Sandia National Labs MEMS Ratchet System . . . . .	3
1.2.	Penny Sized MEMS Combustion Engine . . . . .	4
2.1.	Alessandro Volta and the Voltaic Cell . . . . .	8
2.2.	Moore's Law vs. Battery Growth . . . . .	10
2.3.	Common Electromagnetic Generator Designs . . . . .	11
2.4.	Piezoelectric Generator Designs . . . . .	13
2.5.	Coulomb Force Generator Design . . . . .	15
2.6.	Coulomb-Damped Resonant Generator Design . . . . .	15
2.7.	MFPG Design . . . . .	17
3.1.	Demonstration of Faraday's Law . . . . .	21
3.2.	MFPG Coil and Magnet Design . . . . .	24
3.3.	Rotor Layout - Rectangular Arms . . . . .	27
3.4.	Rotor Layout - Segmented Toroidal Magnets . . . . .	27
3.5.	Nickel Electroplating Process . . . . .	29
3.6.	Concept Drawing of Generator Design . . . . .	32
3.7.	Resistance vs. Coil Turns Plot . . . . .	35
3.8.	Current Path Between Runner and Coil . . . . .	36
3.9.	Thinning of Coil Sidewalls Due to Runner Deposit . . . . .	37
3.10.	Original MFPG Coil Layout . . . . .	38
3.11.	6 and 12-Turn Arrayed Angled Coil Layout . . . . .	40
3.12.	Schematic of Generator Power Testing . . . . .	43
4.1.	Spin Curve for AZ P4620 . . . . .	46
4.2.	Exposure Comparison of AZ P4620 Lithography Patterns . . . .	47
4.3.	Delamination of Sprecher's Nickel Samples . . . . .	48
4.4.	Nickel Electroplating Samples NiStr7b and NiStr8 . . . . .	53

Figure		Page
4.5.	Successful Rotor Deposit . . . . .	55
4.6.	Rotor Deposit with Peeling . . . . .	56
4.7.	Fabricated and Diced Rotor Ready for Testing . . . . .	56
4.8.	Diced Rotor Lifted From Table with NIB Magnet . . . . .	57
4.9.	Runner Deposition Process . . . . .	59
4.10.	Runner Deposit for Concentric Coil . . . . .	59
4.11.	Residual Sidewalls from Runner Deposition . . . . .	60
4.12.	LOR Process . . . . .	60
4.13.	Nitride Deposition Process . . . . .	61
4.14.	Patterned Nitride Covering Runner . . . . .	62
4.15.	Completed 6-Turn Coil . . . . .	62
4.16.	SEM Images of Coil/Runner Interfaces . . . . .	63
4.17.	Eagle 860 Flip Chip Bonder Components . . . . .	64
4.18.	Custom Rotary Stage for Testing . . . . .	65
4.19.	Packaging Used for Coils During Testing . . . . .	66
4.20.	SEM Images of Coil Bonded to Package . . . . .	67
5.1.	Example of $B$ - $H$ Curve . . . . .	69
5.2.	Example of $B$ - $H$ Curve . . . . .	70
5.3.	Alignment of Coil and Rotor using Eagle 860 Flip-Chip Bonder	73
5.4.	Operation of Testing Apparatus . . . . .	74
A.1.	Resistance Calculations . . . . .	80
A.2.	Surface Area Comparisons . . . . .	80
A.3.	Plating Seed Surface Area and Current Density Calculations .	81
B.1.	Full L-Edit Mask . . . . .	82
B.2.	Submask Alignment Marks . . . . .	84
B.3.	Submask 1 - Magnet Deposit . . . . .	84
B.4.	Submask 2 - Coil Runner Etch and Deposit . . . . .	85
B.5.	Submask 3 - Coil Nitride Etch . . . . .	86

Figure		Page
B.6.	Submask 3 - Zoomed in Nitride Etch Holes . . . . .	86
B.7.	Submask 4 - Final Coil Deposit . . . . .	87
B.8.	Submask 5 - Magnet Nickel Plating Seed Etch . . . . .	88
B.9.	Submask 6 - Coil Plating Seed Etch . . . . .	88
B.10.	Submask 7 - Runner Plating Seed Etch . . . . .	89
D.1.	Rotor Referencing Scheme . . . . .	94
D.2.	Coil Referencing Scheme . . . . .	94

## *List of Tables*

Table		Page
3.1.	Generator Design Parameters . . . . .	23
3.2.	Magnetic Properties of Ferromagnetic Materials . . . . .	25
3.3.	Resistivity of Common MEMS Compatible Metals . . . . .	33
4.1.	Nickel Electroplating Experimental Data . . . . .	50
5.1.	Calculation of Resistance Based on Measured Dimensions . . .	72
B.1.	Functions of Micro-Generator Submasks . . . . .	83
C.1.	Runner Trough Etch and Deposit Process Follower . . . . .	90
C.2.	Nitride Deposit and Patterning Process Follower . . . . .	91
C.3.	Final Coil Deposit Process Follower . . . . .	92
C.4.	Nickel Electroplating Process Follower . . . . .	93
D.1.	Profilometer Measurements of Rotors . . . . .	95
D.2.	Resistance Measurements of Coils . . . . .	96
D.3.	Calculation of Predicted Resistance of Coils . . . . .	97

# *List of Abbreviations*

Abbreviation		Page
IC	Integrated Circuit . . . . .	1
MEMS	Microelectromechanical Systems . . . . .	1
RF	Radio Frequency . . . . .	2
BioMEMS	Biological MEMS . . . . .	3
ICD	Internal Cardiac Defibrillator . . . . .	4
AFIT	Air Force Institute of Technology . . . . .	4
MFPG	Microfluidic Power Generation . . . . .	5
rpm	Rotations Per Minute . . . . .	12
NTU	National Taiwan University . . . . .	13
PZT	Lead Zirconate Titanate . . . . .	13
CFPG	Coulomb Force Parametric Generator . . . . .	14
CDRG	Coulomb-Damped Resonant Generator . . . . .	14
Ni	Nickel . . . . .	16
Au	Gold . . . . .	16
emf	Electromotive Force . . . . .	21
L-Edit	Layout Editor . . . . .	26
$Si_3N_4$	Silicon Nitride . . . . .	35
Ti	Titanium . . . . .	35
Cr	Chromium . . . . .	36
Si	Silicon . . . . .	44
PR	Photoresist . . . . .	45
AFRL/RYS	Air Force Research Laboratory/Sensors Directorate . . . . .	48
CTE	Coefficient of Thermal Expansion . . . . .	48
Cu	Copper . . . . .	51
SEM	Scanning Electron Microscope . . . . .	55

Abbreviation		Page
NIB	Neodymium Iron Boron . . . . .	57
RIE	Reactive Ion Etch . . . . .	58
PECVD	Plasma Enhanced Chemical Vapor Deposition . . . . .	58
LOR	Lift Off Resist . . . . .	59
VSM	Vibrating Sample Magnetometer . . . . .	70
AFRL/RZ	Air Force Research Laboratory/Propulsion Directorate . .	70
PLD	Pulse Laser Deposition . . . . .	78

# POWER GENERATION BY HARVESTING AMBIENT ENERGY WITH A MICRO-ELECTROMAGNETIC GENERATOR

## I. Introduction

Can you think of a person that does *not* make use of a mobile electronic device (wireless phone, MP3 player, garage door opener, pacemaker, *etc.*)? It is very unlikely. Mobile electronics are an essential part of our current society. This is due, in no small part, to continuing advances in integrated circuit (IC) and microelectromechanical systems (MEMS) technology. Engineers paradoxically provide more capability and computing power even as the actual electronic devices become smaller. Typically, as these devices become smaller and more powerful, unhampered mobility tends to become a requirement, or at least highly desired.

For an electronic device to be mobile, however, a portable power source is required. For the majority of modern day mobile electronics, that power source is provided by a battery which inherently has severe drawbacks: mass, volume and most importantly, a finite power supply. Recently, much research has been applied in the MEMS domain to discover methods of harvesting energy from the ambient environment of these miniaturized mobile systems and converting that energy to electricity to power the circuitry of the device, thus eliminating the need for batteries and their shortcomings. This thesis will investigate one such method of harvesting that ambient energy.

### ***1.1 Ambient Energy Harvesting***

Energy sources to be potentially harvested and converted to electrical energy include solar, acoustic, thermal and any kinetic motion. Kinetic energy sources are numerous and can be harvested with a number of different methods. Within coal plants, nuclear plants, and hydroelectric dams the kinetic energy of the moving steam

or water is converted through the use of an electromagnetic generator and turbine. A company from Germany, EnOcean GmbH, created a wireless light switch that gleans the energy required to transmit the radio frequency (RF) signal to the lights from the kinetic motion of pushing in the switch [1].

Of course the potential sources of ambient energy depend entirely on the intended environment of the device to be used. If a device does not experience significant exposure to light, then solar harvesting is not a viable option. The environment that the electronic system is designed to operate in must be analyzed in order to identify energy sources that could be harvested. With reported growth rates as high as 78% within the energy harvesting market [1], it appears that there are numerous opportunities to move away from a battery solution and look to harvesting untapped ambient energy.

## ***1.2 Microelectromechanical Systems (MEMS)***

In recent years numerous gaming systems have introduced motion-sensitive controllers through the use of a MEMS accelerometer. MEMS technology is often associated with microelectronics, but there are distinct differences. This misconception is most likely due to the fact that they are both typically manufactured using the same micro and nano-lithographic processes and are often reliant upon one another within a fielded device. While microelectronics make use of silicon and other semiconductor materials to manipulate the flow of electrons and thereby process information, MEMS use those materials to create transducers or minute physical mechanisms such as mirrors, latches, or gears such as those shown in Figure 1.1.

A transducer is defined as “a device that is actuated by power from one system and supplies power usually in another form to a second system” [3]. By acting as a transducer, MEMS provide the capability to transfer information between the physical world and the microelectronic world. When a MEMS device is used to transfer information from the electronic world to the physical, then it is referred to as an actuator. If the MEMS device is used to transfer information from the physical world to



Figure 1.1: A complex MEMS ratchet system of gears created by Sandia National Labs [2].

the electronic, it is referred to as a sensor. The accelerometer that is used in gaming controllers is an example of such a MEMS sensor. The physical kinetic energy that is used to maneuver the controller is transduced to an electrical signal that can be passed to the gaming console.

A wide variety of other MEMS devices are also in use today. They range from something as simple as a beam structure used to measure the stress of a deposited thin film to devices as complex as a penny-sized combustion engine, as shown in Figure 1.2. The field of medicine is also making great use of MEMS technology and a relatively new field of engineering is emerging—BioMEMS. BioMEMS utilize MEMS and IC systems to provide technological solutions to medical problems.

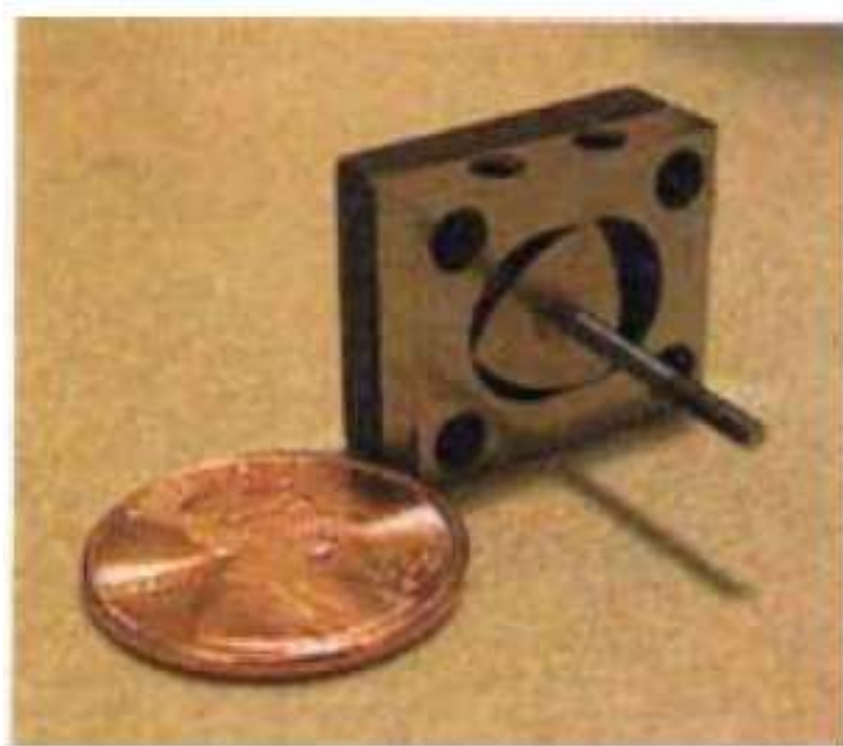


Figure 1.2: A mini combustion rotary engine designed and developed by a team at the University of California at Berkeley [4].

### ***1.3 Problem Overview***

As was discussed in the previous section, a rapidly progressing MEMS field is that of BioMEMS. Obviously, in order for some of these BioMEMS systems to be applicable to biological problems, they are often implanted into the body. Examples of such systems already in use today include pacemakers, internal cardiac defibrillators (ICDs) and biosensors. Many more bio-implanted devices are currently being researched and developed to be used in the future. Given that these devices are implanted in the body, replacing the battery usually requires another surgery similar to the initial implantation. For ICDs, this can be as frequent as every three years.

If one were to discover a method to harvest energy from the body to power the implanted BioMEMS device, it would then be self-sustaining and no additional surgeries would be required after implantation. In 2007, a previous student at the Air Force Institute of Technology (AFIT), Aaron Sprecher, proposed harvesting en-

ergy from blood flow similar to the way a hydroelectric dam harvests energy from the flow of water [5]. His design used a micro-sized electromagnetic generator to convert the energy of blood flow to electricity. Sprecher was unable to completely fabricate his design within the time frame he was allotted, but was able to propose a design, perform theoretical calculations, and begin characterizing fabrication methods. Currently, there are a number of unanswered questions about his proposed design. Primarily, how much power can one realistically harvest using his Microfluidic Power Generation (MFPG) approach? Will his predicted estimates match the experimental results? What parameters are most influential in optimizing the efficiency of the electromagnetic generator? Is it feasible to fabricate the device as it was originally envisioned?

#### ***1.4 Research Intent***

The goal of this thesis is to further investigate the feasibility of using a micro-electromagnetic generator to harvest energy from fluid flow and answer those questions that were proposed in the previous section. With the rapid advancements that are occurring in MEMS technology, it seems logical to believe that an electromagnetic generator design that is extensively used at the macro scale should be achievable at the micro scale as well. However, very little research has been accomplished to characterize electromagnetic generators at the micro scale, therefore, it is the intent of this thesis to fabricate the micro-electromagnetic generator portion of the MFPG design and thereby characterize the potential power output of such a device.

The original MFPG design included numerous components and assembly was complex. This thesis will focus on the fabrication and design of the generator portion only, thereby reducing complexity and allowing for full characterization of the potential power output. The following objectives will lead to such a characterization of the micro-electromagnetic generator:

1. Design and fabricate a MEMS-compatible magnetic rotor for a micro-generator.

2. Design and fabricate a MEMS-compatible stator coil that minimizes resistance and maximizes power output.
3. Determine how to best polarize the rotor magnet structures.
4. Design a simple testing apparatus for the generator that allows for power output measurements.
5. Perform the characterization tests for varying generator designs and parameters.

### **1.5 *Organization of Thesis***

This thesis will be organized in the following manner:

**Chapter 1 - Introduction** Provide an introduction to this thesis effort by pointing out the need to move away from batteries for mobile devices, provide an overview of MEMS engineering, identify the questions that need to be answered before fully fabricating the MFPG design, and lay out the goals of this effort.

**Chapter 2 - Literature Review** Discuss the current research in micro-power generation that applies to a bio-implanted system and the challenges associated with it. Provide background information of previous micro-generator research accomplished at AFIT.

**Chapter 3 - Methodology and Theory** Explicitly detail the problem solving approach for designing a micro-generator. Discuss the theory upon which proposed layouts and material selection was based. Present optimized designs and discuss testing requirements.

**Chapter 4 - Fabrication** Discuss the fabrication process of the rotor magnet, stator coil and testing apparatus. Present the characterization process for any steps that required characterization.

**Chapter 5 - Testing and Results** Discuss results of testing of the micro-generator and identify trends.

**Chapter 6 - Conclusions** Provide recommendations for future research and discuss the scientific contributions made during this effort.

**Appendix A - Supporting Calculations** Calculations performed for this thesis effort.

**Appendix B - Lithographic Mask Design** Provides details and images of the lithographic mask used for the micro-generator.

**Appendix C - Fabrication Methods** Compilation of process followers and fabrication methods used.

**Appendix D - Experimental Raw Data** Collection of the raw data collected from the micro-generator measurements and testing.

## II. Literature Review

This chapter will explore some of the state-of-the-art techniques of micro-power harvesting and their associated research; focusing on the techniques that could potentially be used with bio-implanted systems. In addition, the research that was previously conducted at AFIT will be discussed and analyzed. Finally a summary of the ongoing challenges associated with this field of research will be presented.

### 2.1 *From Batteries to Harvesters*

In 1800 Alessandro Volta invented the first voltaic cell battery and with it the potential to create portable electronic devices, see Figure 2.1 [6]. In today's wireless world, the battery has become indispensable. But even after two centuries, the battery still has its drawbacks as mentioned in Chapter I: mass, volume and a finite power supply. Increased mass and size are obviously undesirable for most portable systems on the market today, where smaller and lighter is always desired and often times advantageous, or even required, for specific system applications. However, the finite power supply limitation results in an incapacitating weakness for systems that once deployed are very difficult to access again, such as remote sensors or bio-implanted devices.

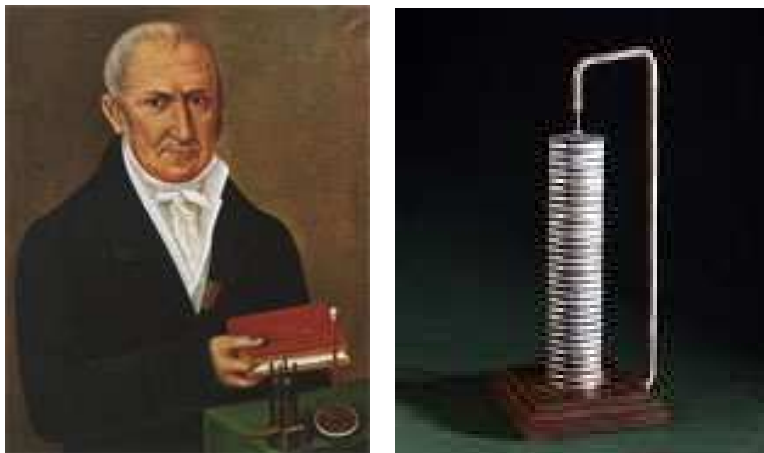


Figure 2.1: A portrait of Alessandro Volta and an image of his design of the first electric battery made of metallic disks and a salt solution, the voltaic cell [6].

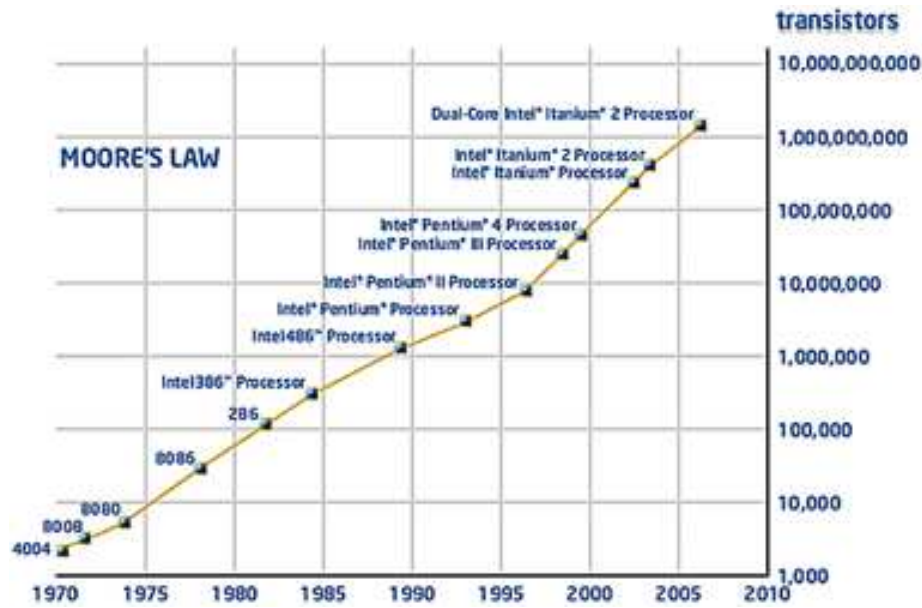
In 1965, Gordon Moore predicted a yearly exponential growth of the number of transistors on a computer chip, commonly referred to as Moore's Law [7]. It is interesting to note that although the exponential growth of Moore's Law has held true, the capacity increases for batteries over the years has followed a much slower, more linear progression. Figure 2.2(a) and (b) illustrate this. Nevertheless, advances in battery technology are taking place, albeit at a linear pace. It is very doubtful, however, that the engineering community will ever be able to produce a battery with an infinite energy supply. This leads to a non-debatable requirement to develop a capability to provide self-sustaining power supplies at a miniature to micro scale.

Until recently micro-scale power generation was not viewed as a viable source to replace batteries due to the relatively small amount of power that is generated at the micro scale. However, as MEMS and IC components continue to be reduced in size, the power requirements are also being reduced to the scale of tens to hundreds of  $\mu\text{W}$  [9], the same scale as micro-power generation. Industry has now reached a point that the small amounts of power that could potentially be harvested from ambient energy are sufficient to power current MEMS and IC devices.

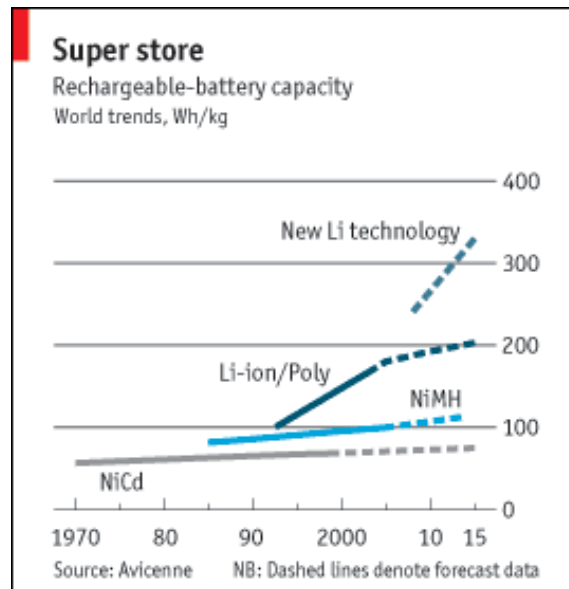
## ***2.2 Micro-Scale Energy Harvesting Research***

Throughout the most recent decade, numerous scientists and engineers across the world have taken great interest in energy harvesting at the micro-scale and many different approaches are being taken. Some techniques are based on energy harvesting techniques that are used every day at the macro scale such as solar, thermal, and electromagnetic systems which include wind, hydroelectric and fossil fuel generators. However, additional sources that become more applicable at the micro scale are also being investigated including piezoelectric and electrostatics.

Solar energy harvesting is a proven method. It is prevalently used in many systems. However, even though solar cell efficiency continues to increase, this harvesting technique does require a light source be readily available for prolonged periods of time.



(a) Moore's Law Graph [7]



(b) Battery Capacity Graph [8]

Figure 2.2: (a) Moore's Law predicts an exponential growth in transistor technology; a trend that has been followed since the 1970s. (b) Battery capacity growth has followed a much more linear trend. Note the logarithmic scale of transistor growth compared to the linear scale of battery capacity growth.

For most personal electronics and all bio-implanted systems this is not an option that would be applicable.

Thermal energy harvesting requires that thermal gradients be present. Again, although thermal gradients are available in some environments, this is not a viable option for bio-implanted devices given that there are no consistent and substantial temperature gradients in the body. Therefore, electromagnetic, piezoelectric, and electrostatic energy sources are the potential solutions for bio-implanted devices and each will now be investigated in depth in the subsequent sections [10].

*2.2.1 Electromagnetic Power Generation.* Electromagnetic generators at the macro scale are well understood energy sources. They have been used for decades in hydroelectric dams, fossil fuel plants and wind generators. The interest in the use of electromagnetic generators at the micro scale is largely based on the high power density and efficiency found in the macro scale systems. In fact, it has been shown that the flux density available from a permanent magnet is independent of its size and that current densities might even benefit from increased surface area and reduced volume, which bodes very well for MEMS devices [11]. Dr. David Arnold from the University of Florida [12] compared the three basic types of permanent magnet generators. Figure 2.3 provides illustrative examples of each type of permanent magnet generator.

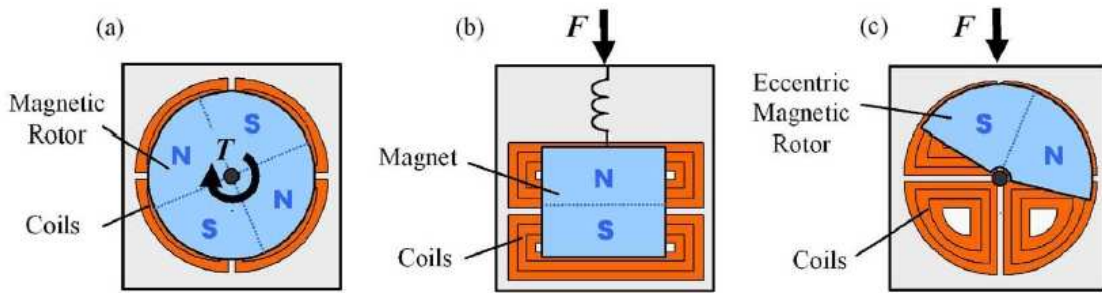


Figure 2.3: Types of Permanent Magnet generators: (a) rotational, (b) oscillatory and (c) hybrid, or eccentric, which converts linear accelerations into rotational kinetic energy [12].

Rotational generators require a continuous mechanical force in order to provide the required rotation. They do, however, provide relatively high power densities and electrical frequencies if rotated at a high speed. Two sources of rotational mechanical force have been investigated for this type of device: fluidic flow and heat engine [12].

Oscillatory generators are based on proof mass/spring/damper systems and numerous different configurations are being investigated. One benefit of the oscillatory generator is that energy is produced over a wide range of frequencies so that all movement will produce some energy, although the maximum power output is at the resonant frequency, which tends to be very high for MEMS devices. The power density is typically much lower in oscillatory generators than that of rotational generators [12].

The hybrid generator, or eccentric rotor, was first popularly introduced to self-power watches. Any acceleration in the direction of the pivot produces energy. These types of generators offer power densities on the same order as oscillatory generators but have a much wider frequency band response and are sensitive in two axes rather than just one [12].

All three configurations of the permanent magnet generator offer applications for bio-implanted energy harvesting. Fluid flow is a potential energy source for the rotational generator, whereas walking and general body movements are potential energy sources for the oscillatory and eccentric systems. The rotational system provides the highest power density options as long as high rotations per minute (rpms) are achievable. It appears that the eccentric system might provide higher power densities than the oscillatory within a bio-implanted system given that the eccentric motor harvests energy in two axes rather than only one. In addition, as pointed out earlier, the oscillatory will not be able to achieve max power density within a bio-implanted system due to the fact that the natural frequencies of the body tend to fall far below the resonant frequencies of MEMS devices.

*2.2.2 Piezoelectric Power Generation.* Piezoelectric materials have the property of producing an electric field when they experience compression or strain.

The typical technique of harnessing this property to harvest energy consists of building piezoelectric structures that are sensitive to accelerations. As these accelerations occur, the structures are simply compressed or stretched and thereby a current is produced. However, just like the oscillatory permanent magnet method, resonant frequencies are required in order to achieve the best results.

A proposed improvement on this technique makes use of an electromagnet to vary the strain in the host material and thereby alter and expand the piezoelectric material's frequency domain. This method creates a broadband frequency spectrum for the piezoelectric material, but requires the added complexity of another device to vary the host's strain [13].

A group at National Taiwan University (NTU) designed, fabricated and characterized two prototypes of a piezoelectric generator based on the acceleration-sensitive structures technique presented above. The first design, as represented in Figure 2.4(a), used a beam cantilever covered in PZT (lead zirconate titanate), a piezoelectric material. The size and density of the proof mass at the end of the cantilever determined the resonant frequency of the beam. The interdigitated electrodes extract the charges generated by the PZT as ambient vibrations are experienced and strain is induced in the cantilever. Using a  $3000 \times 1500 \times 30 \mu m^3$  cantilever, NTU was able to extract  $15 \mu W$  with a load resistance of  $210 K \Omega$  at a frequency of 1.5 KHz.

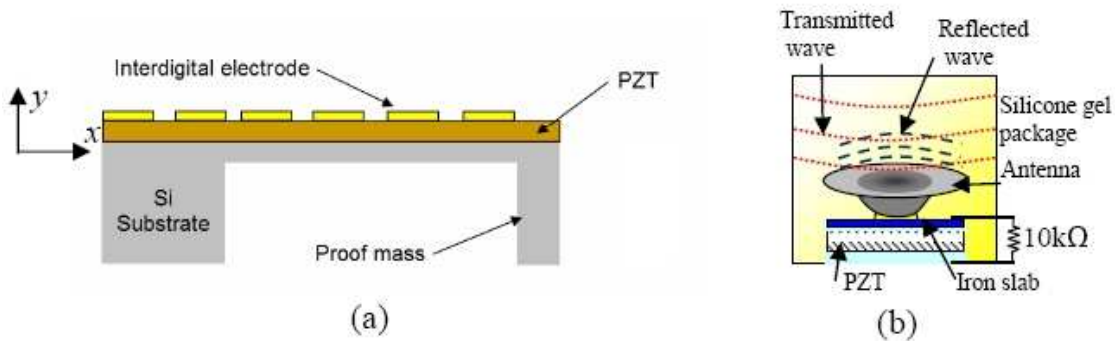


Figure 2.4: Schematics of NTU's piezoelectric MEMS generators: (a) low frequency cantilever design (b) high frequency disk shaped design [9].

The second design, represented in Figure 2.4(b), functions at much higher frequencies. The antenna is encased in a gel and sits on top of a PZT slab. Incoming high frequency acoustic waves, approximately 75 KHz, vibrate the antenna and thereby induce strain in the PZT slab underneath, resulting in charge being produced. Using a spherical gel package, NTU was able to achieve a maximum power output of -40 dB relative to the transmitted signal [9]. It must be noted that although this method is not technically harvesting naturally occurring ambient energy, it does propose an alternative solution to physically replacing batteries. One could potentially recharge batteries or capacitors by sending a signal, wirelessly, to a bio-implanted system.

Given that these piezoelectric devices are so sensitive to accelerations, they provide yet another option to harvest ambient energy for a bio-implanted device. The power density appears to be on the same scale as what has been found with the electromagnetic generator as well.

*2.2.3 Electrostatic Power Generation.* The last technique for power generation to be reviewed makes use of electrostatics at the micro scale. There are two types of electrostatic power generation devices that will be examined here. One is termed as a Coulomb Force Parametric Generator (CFPG) and the other is a Coulomb-Damped Resonant Generator (CDRG). The CFPG generator produces power via accelerations and is not tuned to a particular frequency. Dr. Paul Mitcheson led a group at the Imperial College London in designing a CFPG capacitor-based prototype device as envisioned in Figure 2.5. It is primed by placing a charge on the mass plate. When the device experiences accelerations of approximately  $3 \text{ m/s}^2$  (that of walking), the mechanical force will exceed the electrostatic force holding the plates together and the upper plate will break away. The charge that was placed on the mass is unable to drain and a voltage of approximately 250 volts is produced [14, 15].

The CDRG generator extracts energy using a damper that provides an opposing force against movement. The damper is provided by a structure with a trapped charge. Dr. Mitcheson designed a potential MEMS implementation of such a device based on

a comb drive structure, see Figure 2.6. The mass portion of the comb drive, sometimes referred to as the sled, has a charge placed upon it. External accelerations cause the sled to move and as long as the charge on the sled is not allowed to bleed off, the trapped charges will cause voltage variations in the stationary electrodes. With this type of device there is always a resonant frequency where optimal power output will

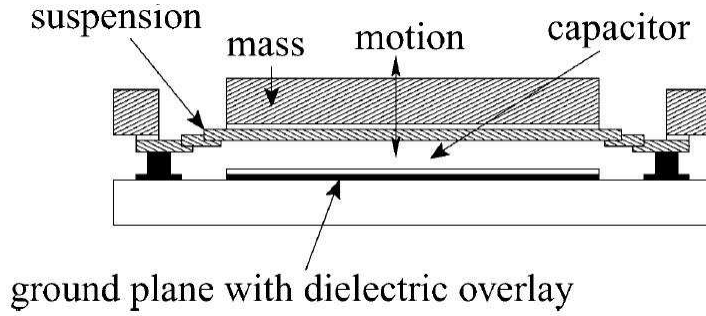


Figure 2.5: Potential implementation of Mitcheson's CFPG design. A charge is placed on the mass part of the comb drive and not allowed to bleed off. As the mass experiences acceleration, the trapped charge causes voltage swings to occur in the stationary electrodes, producing current [14].

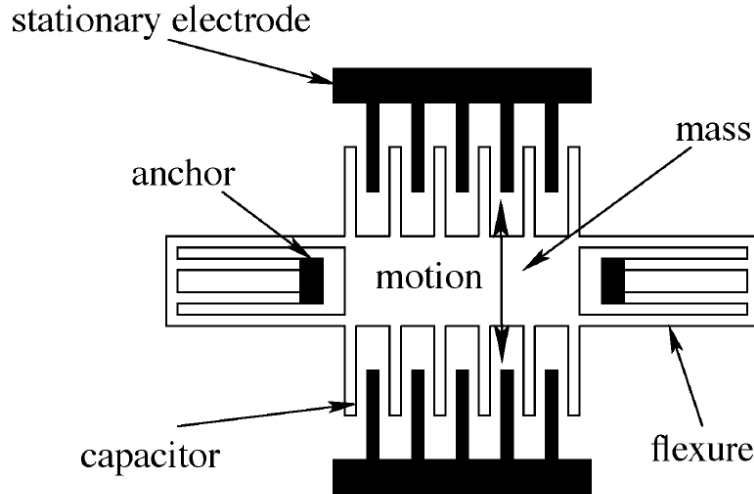


Figure 2.6: Potential implementation of Mitcheson's CDRG design. A charge is placed on the mass part of the capacitor and not allowed to bleed off. As the mass experiences acceleration the trapped charge causes voltage swings to occur, producing current [14].

occur. With MEMS devices of this type, the resonant frequency tends to be in the tens of KHz range [14], a range difficult to obtain in the human body.

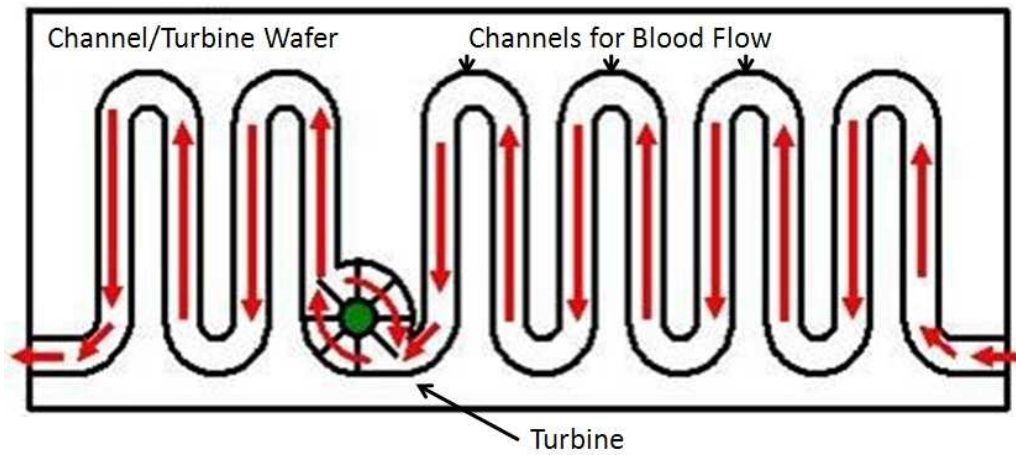
Both electrostatic generator methods discussed here, CFPG and CDRG, are potential candidates for bio-implanted devices. However, the high resonant frequencies required for power generation using the CDRG method might result in extremely low power output.

*2.2.4 Previous AFIT Research.* As mentioned previously, research into a potential power generation scheme was accomplished by Aaron Sprecher at AFIT and presented in his thesis in 2008. His device, the MFPG, was intended to harvest energy from blood flow in the capillaries of the body. Figure 2.7 provides a representation of the design he had envisioned. He based his generator design on a rotational permanent magnet generator and predicted a theoretical max power output of  $0.3325 \mu\text{W}$  for his dimensions. The design proposed used nickel (Ni) for the magnetic material and gold (Au) for the wire coil [5]. Both materials are frequently used within the MEMS process.

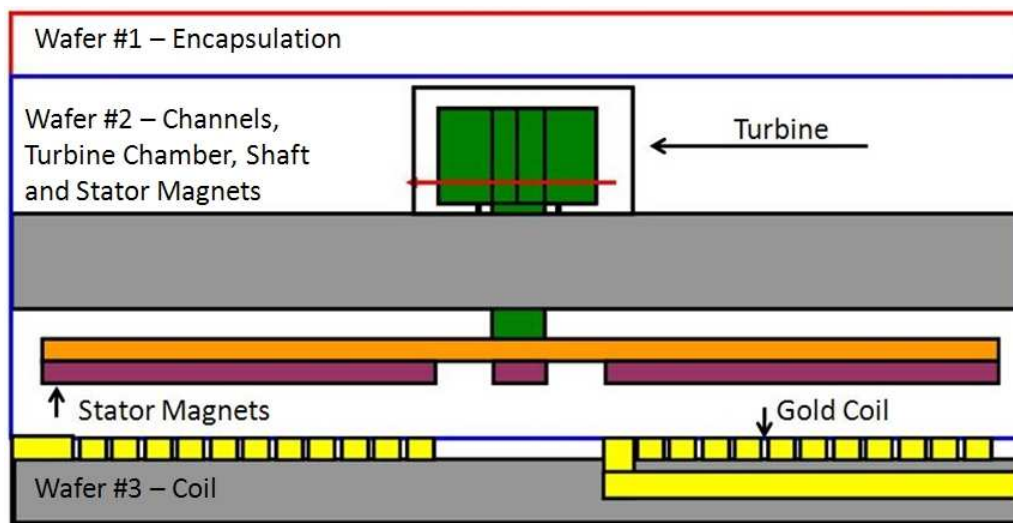
Being specifically engineered for bio-implanted systems, the MFPG offers a lot of potential. However, as mentioned in Chapter I, very little experimental data was collected due to problems that were encountered during fabrication. These issues will be addressed more fully in Chapter III. Also, it is unknown how much power can be realistically harvested from blood flow using this type of generator given that the device was never fully fabricated.

### ***2.3 Identified Challenges***

There are a number of challenges and opportunities for additional research within the micro-power generation community. For example, it appears that the theoretical calculations do not always agree with experimental results found in most of the research discussed here. This is largely due to the lack of accurate models for micro scale mechanical interactions. MEMS is a relatively new field of engineering



(a) MFPG Top View



(b) MFPG Side View

Figure 2.7: The MFPG was designed to harvest energy from blood flow. The device is assembled by stacking three wafers. (a) A top view illustrates the channels where blood would flow and the turbine used to harvest the energy. (b) The side view illustrates how the turbine is connected to the rotor magnets with a shaft. As the turbine and rotor magnets rotate, a current is induced in the gold wire coil below the magnets [5].

and there is still much to learn. Of particular interest is how permanent magnets scale at the micro level. Severe discrepancies have been noted between predicted values and experimental results [12]. Actually fabricating the devices discussed here and characterizing them would provide much data to potentially develop more accurate models for this area of research.

In addition, electromagnetic generators require low-friction. Given that only a small amount of ambient energy will be collected in a micro generator system, it is essential that each system be extremely efficient so as to maximize power output. Potential solutions include micro ball bearings, gas bearings, and magnetic bearings, all of which are currently being researched. However, even if one of these technologies was found superior, the integration of such a technology only leads to more complexity in the fabrication process [12].

Another challenge includes the fact that industry's capability to deposit and pattern certain ferromagnetic materials at the micro level has yet to approach their capability at the macro level. For electromagnetic generators, the use of high energy density magnetic materials such as CoPt, FePt, SmCo or NdFeB is essential, but microfabrication methods such as sputtering and evaporation are relatively primitive for these types of materials. In addition, to achieve optimal magnetic properties, high temperature anneals are required. The annealing process allows for more of the magnetic moments to align, creating stronger fields, but the high temperature also limits the types of materials that can be integrated with the magnets [12]. Piezoelectric materials are just as difficult to pattern and deposit at the micro scale. Numerous processes are currently being used, such as sol-gel deposition and "jet-printing," but a standardized, high resolution process is not currently available [9].

Along with discovering new harvesting techniques, engineers must also design new micro-power devices and circuits that convert and condition the supplied energy so as to properly power the IC portion of the integrated system. This has proven difficult due to the fact that some ambient energy harvesting techniques do not provide

continuous energy supplies, are not necessarily harmonic and often provide only short pulses of energy. The group at the Imperial College London claim to have designed a converter device for their electrostatic generator that takes all of these limitations into consideration by analyzing the system parasitics and selecting specific transistor devices that optimized their converter [15]. This converter, however, is applicable to only a CFPG type of electrostatic generator. Similar research needs to be applied to all the other types of generators discussed in this paper as well.

This thesis effort will focus on collecting more data applicable to two of these micro-power generation issues—matching experimental with theoretical data and patterning magnetic material at the MEMS level. A test apparatus will be designed and experimental power generation data will be collected. This experimental data can then be compared with the theoretical calculations and used to improve the models. In addition, it is anticipated that throughout the process of fabricating the magnets to be used in the micro-generator, a successful patterning process will be identified.

## ***2.4 Chapter Summary***

This chapter has reviewed multiple methods of micro power generation being researched today. Electromagnetic, piezoelectric and electrostatic generators appear to be the most logical solutions for bio-implanted devices. The benefits and difficulties associated with each type were discussed. In addition multiple challenges and potential research topics for this area of study were laid out.

Without a doubt there is much to learn and discover about micro power generation and the capability to harness the ambient energy that surrounds us every day. It is the intent of this thesis research to obtain more data for the community at large in order to increase the knowledge base for this area of interest.

### III. Methodology and Theory

As discussed in previous chapters, this research is based on the MFPG design presented by a previous student at AFIT, Aaron Sprecher [5]. The MFPG design proposed harvesting energy from blood flow in the human body. Blood flow actuated micro turbines which, in turn, rotated magnetic rotors above stator coils, thereby inducing a current in the coils. Given that the device was never fully fabricated or tested, this thesis will build upon the original generator design and characterize the potential power output of the proposed design.

The process of designing and fabricating a micro-electromagnetic generator requires knowledge of multiple engineering disciplines including: electromagnetism, microfabrication techniques, and microelectronic device physics. This chapter will present the methodology utilized in this research effort alongside the associated theory and design approaches. Primarily, it is essential to understand how electromagnetic generators function. By investigating how they work, one can identify what parameters optimize performance, and design to those optimizations.

#### ***3.1 Electromagnetic Generators***

Electromagnetic generators form the basis for the majority of today's energy production. Coal, nuclear, wind, and hydroelectric power generation all make use of electromagnetic generators. All of these generators consist of a turbine, rotor and stator. The rotor and stator make up what will be referred to as the active generator, meaning that they contain the magnetic and conductive coil components of the generator, and therefore are the primary source of power generation within the device.

The turbine makes direct contact with a fluid flow, such as steam, wind, water, *etc.*, and is shaped such that the interaction with the fluid flow causes the turbine to rotate. The rotor is attached to the turbine via a shaft and is the moving portion of the active generator. It consists of either an array of magnets or an array of conductive coils. The stator is stationary and is composed of coils if the rotor is magnetic and of

magnets if the rotor is an array of coils. As the fluid flow pushes through the turbine, it rotates the turbines, and therefore the rotor as well. This rotation induces a current in the coils and power is transduced from the kinetic energy of fluid flow to electric energy.

*3.1.1 Theory of Electromagnetic Generators.* Electromagnetic generators function on the principle of electromagnetic induction, also known as Faraday's Law. Faraday's Law states that when a magnet and a coil are relatively close, any time changing magnetic flux results in a current flow in the coil. Quantitatively, Faraday's Law is expressed as

$$\xi = -N \frac{d\Phi_B}{dt} \quad (3.1)$$

where  $\xi$  is the electromotive force (emf) for voltage,  $N$  is the number of turns of the coil and  $d\Phi_B/dt$  is the rate of change of magnetic flux with time [16]. Figure 3.1 provides an illustration of this law. As the bar magnet is moved within the coil, a current is induced in the coil and the galvanometer, or ammeter, is deflected. The

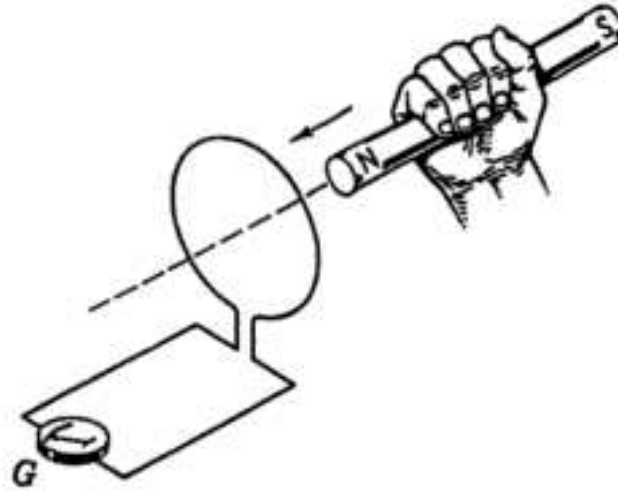


Figure 3.1: As the bar magnet is moved in and out of the coil, the galvanometer registers current flow. However, the current only flows during motion of the magnet or coil. No current flows when the coil and magnet are at rest [17].

galvanometer is deflected in the opposite direction as the magnet is withdrawn from the coil.

In addition, Maxwell's 4th equation, known as the Ampère-Maxwell Law, states that

$$\nabla \times B = \mu_0 J + \mu_0 \epsilon_0 \partial E / \partial t. \quad (3.2)$$

This law defines the relationship of the curl of the magnetic field ( $\nabla \times B$ ) to the current density ( $J$ ) and displacement current ( $\partial E / \partial t$ ).  $\mu_0$  is the permeability of free space and  $\epsilon_0$  is the permittivity of free space. It is through the use of Ampère-Maxwell's Law that one can also determine the direction of the current flow induced by using the right-hand rule. The right-hand rule, as it pertains to magnetic fields, states that if one curls their right hand in the direction of the  $B$  field then the direction that your thumb is pointing is also the direction of current flow.

Therefore, using Equation 3.1 and Equation 3.2 it is shown that a time changing magnetic field will induce a current within a wire in that field and the current is optimized when the current flow, the magnetic field and the direction of motion are all mutually orthogonal. These laws form the basis for the development of a micro-generator.

*3.1.2 Generator Design Parameters.* The driving factor for designing the micro-generator is to maximize power output for the device. Equation 3.1 states that the number of turns in the coil and the rate of change of the magnetic field directly affect the amount of power output. Equation 3.2 states that the magnitude of the  $B$  field and orientation of the  $B$  field to the coil will affect the current density and electric field induced as well. It can also be inferred that the closer the magnet is to the coil then the stronger the coil will be affected by the magnetic field. The amount of power that is consumed in the coil of the generator will have a direct affect on the amount of power delivered to the load as well. This consumption of power can be reduced by decreasing the resistance of the coil. All of these considerations are compiled in Table 3.1 for quick reference.

Table 3.1: Generator Design Parameters

Parameter	Increasing/Decreasing	Influence on Power Output
$B$ Field Strength	Increasing	$\uparrow$
# of Turns in Coil	Increasing	$\uparrow$
$d\Phi_B/dt$	Increasing	$\uparrow$
Purely Orthogonal Orientation	Increasing	$\uparrow$
Magnet/Coil Distance	Decreasing	$\uparrow$
Resistance of Coil	Decreasing	$\uparrow$

In addition, it must be recognized that MEMS and microelectronics fabrication is typically a very planar process. This means that fabrication is usually accomplished by alternating minute etching and deposition processes on a 2-dimensional surface. However, as shown in Figure 3.1, the magnet in most generators is moved in the direction normal to the coils, which requires a 3-dimensional fabrication process. Such a design, although possible, adds a lot of complexity to the microfabrication process. In order to keep the fabrication process as simple as possible, it is the intent of this effort to use an optimized 2-dimensional planar design for the coil and magnet orientation.

The original MFPG design took the planar scheme into account and planned to use a concentric circle stator coil below a rotor magnet. Figure 3.2 provides an illustration of the coil and rotor that were originally envisioned. A wire covered by silicon nitride forms a path for current to flow out from the center of the coil. By revolving the rotor in close proximity above the single coil, a current should be induced in the coil. The theory and MFPG design discussed in this section were applied to the new designs of the coil and magnet presented in the next couple of sections.

### 3.2 Magnet Design

Per Table 3.1, the power output optimization parameter that is solely dependent on the magnet is the strength of the  $B$  field. Therefore, maximizing the  $B$  field of the magnet will be a top priority for the design. This section will discuss the process for

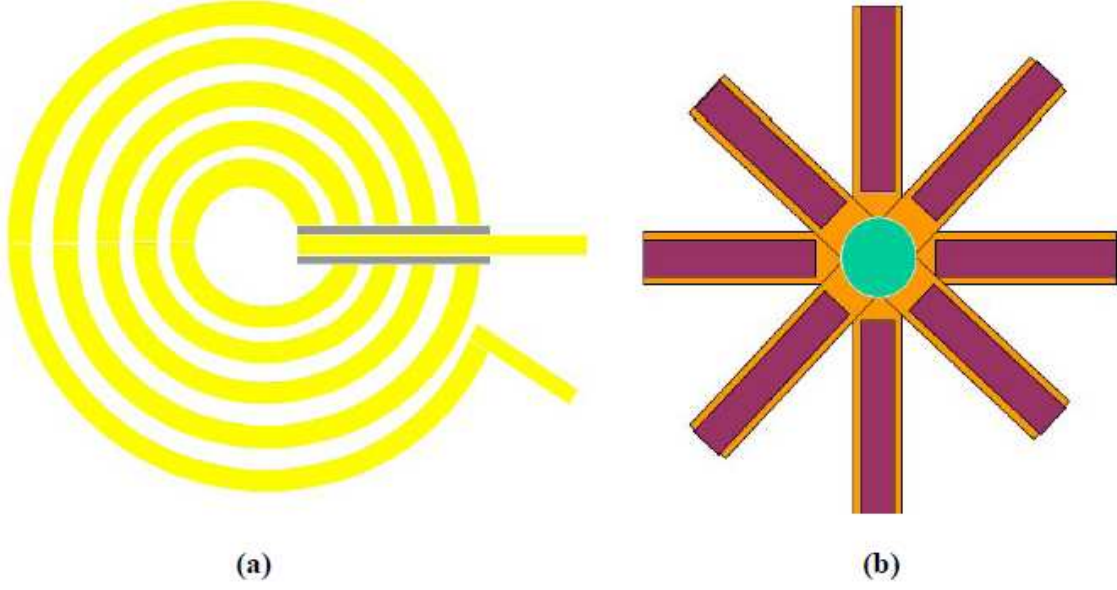


Figure 3.2: Initial envisioned design of the MFPG. (a) Bottom view of gold induction coil with nitride layer (grey) shown where the wires cross. (b) Rotor magnet with 8 rectangular arms [5].

selecting the material to fabricate the magnet, designing the layout of the magnet, and the process to be used for fabrication.

*3.2.1 Magnetic Material Selection.* The magnetic strength of materials is defined by the orbital and spin motion of electrons within the material. If the electron moments are aligned, then magnetic properties will be observed. Generally, it can be stated that the higher a material's permeability,  $\mu$ , the more magnetic it is. Permeability is defined as

$$\mu = \mu_0 \mu_r \quad (3.3)$$

where  $\mu_0 = 4\pi \times 10^{-7} \text{ H/m}$  is the absolute permeability of free space and  $\mu_r$  is known as the relative permeability of the material.

Materials generally fall into three types of categories: ferromagnetic, diamagnetic, and paramagnetic. Ferromagnetic materials, such as iron or nickel, have a  $\mu_r$  significantly greater than unity which causes them to be easily magnetized. If the material effectively retains the magnetization, it is commonly referred to as a permanent

Table 3.2: Magnetic Properties of Ferromagnetic Materials [19]

Material	Treatment	Initial Relative Permeabil- ity ( $H/cm^2$ )	Maximum Relative Permeability ( $H/cm^2$ )	Coercive Force ( <i>Oersteds</i> )	Remanent Flux Density ( <i>Gauss</i> )
Iron, 99.8% pure	Annealed	150	5000	1.0	13,000
Iron, 99.95% pure	Annealed in hydrogen	10,000	200,000	0.05	13,000
78 Permalloy	Annealed, quenched	8,000	100,000	0.05	7,000
Superpermalloy	Annealed in hydrogen, controlled cooling	100,000	1,000,000	0.002	7,000
Cobalt, 99% pure	Annealed	70	250	10	5,000
Nickel, 99% pure	Annealed	110	600	0.7	4,000
Steel, 0.9% C	Quenched	50	100	70	10,300
Steel, 30% Co	Quenched	—	—	240	9,500
Alnico 5	Cooled in magnetic field	4	—	575	12,500
Silmanal	Baked	—	—	6,000	550
Iron, fine powder	Pressed	—	—	470	6,000

magnet. Diamagnetic materials, such as plastic or gold, have a  $\mu_r$  of unity or less and are not capable of being magnetized. Paramagnetic materials have a  $\mu_r$  only slightly greater than unity and are weakly magnetic. Aluminum is an example of this type of material. When it experiences a magnetic field of sufficient strength, it demonstrates some magnetic properties. However, if additional energy is transferred into the material, the moments will quickly return to a random pattern and the magnetic properties will weaken [18].

Given that a strong magnetic field is desired for the micro-electromagnetic generator, only ferromagnetic materials were examined to determine which could be used for this design. Table 3.2 provides a list of some ferromagnetic materials. Of this list, only nickel is commonly used with MEMS processes and offers a relatively high potential remanent flux density. In addition, nickel is one of the materials that AFIT

has the ability to deposit. An 80%/20% nickel/iron alloy has been electroplated in MEMS processes as well and offers a higher permeability [20], however, AFIT does not have this material readily available for deposition. A pure nickel deposition will be used for this effort.

*3.2.2 Magnet Layout Design.* It is not completely clear how the layout of the magnets will affect the power output of the device. As discussed earlier, most electromagnetic generators operate in a 3-dimensional environment, whereas, the micro design is intended to be a planar scheme. No relevant research was found that addressed how to best layout the magnetic portion of the generator with such a planar design. There are, however, two aspects of the layout that are important and did play into the proposed designs.

First, it was decided that the magnets should be attached to the rotor and the coil should be the stator portion of the generator, just as was originally envisioned with the MFPG. The reasoning is that the coils will be attached to a load. Keeping the load and coil stationary would reduce design complexity significantly. The magnets, however, do not require any physical interface with another component and are therefore the best choice for the rotor.

In addition, it is known that a time-varying change in magnetic field will be required to induce the current per Faraday's Law. For a planar design, such as that proposed with the MFPG, this translates into a gap between magnets. The gap allows for the coils to experience variations in the magnetic fields. When a magnet is directly over the coils, a strong magnetic field will be experienced. As the magnet moves off of the coil, the field is decreased. The rate of change of the field will be defined by the speed of rotation of the turbines.

In order to identify some trends and determine if the magnet layout really makes an appreciable difference in power output, a few different layouts were evaluated. All layouts were created using the Layout Editor (L-Edit) of MEMS Pro<sup>TM</sup> Version 6.0. The rotor layouts are of two different varieties: rectangular arms and segmented

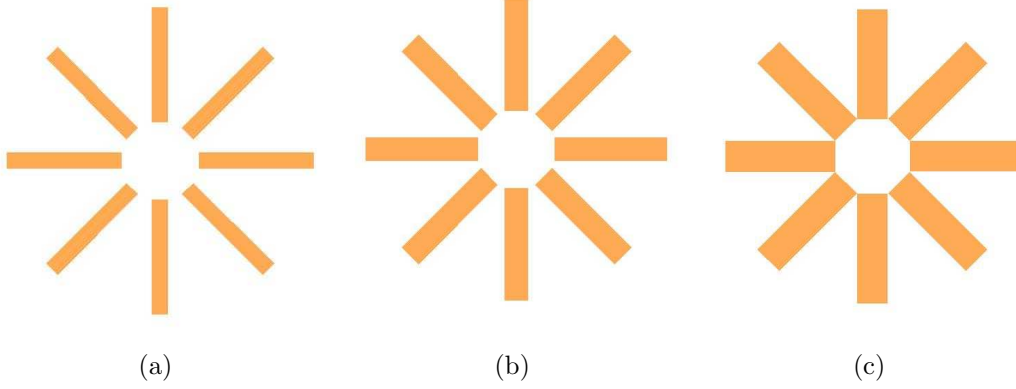


Figure 3.3: Rectangular Magnet Layout. Each arm is  $580\ \mu m$  long with varying width. Arm width is  $80\ \mu m$  for (a),  $120\ \mu m$  for (b) and  $160\ \mu m$  for (c). Inner diameter of the ring is  $400\ \mu m$ .

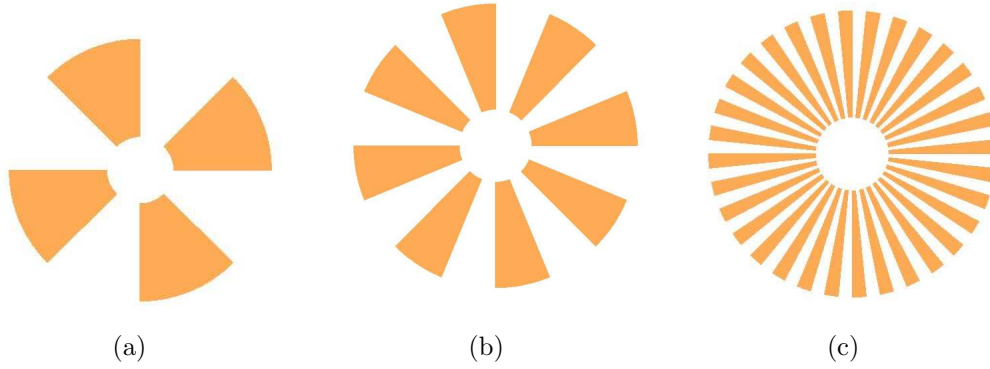


Figure 3.4: Segmented Toroidal Magnet Layout. Each arm is  $580\ \mu m$  from center to edge. Arm width varies from center to edge but (a) has 4 equally distributed arms, (b) has 8 and (c) has 32. Inner diameter of the ring is  $400\ \mu m$ .

toroidal arms. All are annular in shape with the inner ring being  $400\ \mu m$  in diameter and the outer ring being  $1560\ \mu m$  in diameter. Figure 3.3 provides images of the three types of rectangular magnets that were fabricated. The variation of these three types is the actual width of each arm. The arms in Figure 3.3 (a), (b) and (c) are  $80\ \mu m$ ,  $120\ \mu m$  and  $160\ \mu m$  wide respectively. The original MFPG design used the rotor with  $80\ \mu m$  wide arms.

Figure 3.4 contains the images of the three segmented toroidal designs. The toroidal design provides evenly spaced arms with variations in the number of arms. The benefit of this design over the rectangular design is that the toroid magnetic

fields should be much more evenly distributed from the center of the coils to the edge of the coils than the fields produced by the rectangular arms. Experimentation will determine if this favorably affects power output or not.

*3.2.3 Nickel Deposition Process.* The actual deposition of the nickel will play a very important role as well. As discussed earlier, magnetism is a result of the vector sum of multiple electron spins. Therefore, the more massive the nickel deposit, the stronger the magnetic field because more nickel atoms are contributing to the vector sum. However, a balance must be found given that the final generator should be micro-sized. In addition, to maximize the remanent flux density of the nickel, the deposition needs to be as uniform and deformity-free as possible.

Nickel is typically deposited by sputtering, evaporation, or electroplating within the microfabrication community. Electroplating is the conventional MEMS process for depositing relatively large amounts of nickel of more than 1 to 2  $\mu m$ . It allows one to deposit large amounts of metal onto a MEMS structure in a reliable and measurable way.

The nickel electroplating process at local facilities has not been fully characterized. Due to that fact, a significant portion of this research will investigate the plating process in an attempt to characterize it so that deposited nickel for the rotor magnets will be as pure and clean of defects as possible with the provided tools. The typical process of electroplating is represented by Figure 3.5. Passing a current between two electrodes that are immersed in a conductive solution of nickel ions causes the anode, usually a nickel plate or bar, to dissolve. The cathode, however, attracts the ions in the solution. As the ions touch the cathode, the cathode neutralizes the charge of the ion and a nickel atom is deposited on the cathode [21]. A reverse current is also possible and would cause the exact opposite to occur, the cathode would give off ions and the anode would have nickel deposited on it.

There are numerous parameters that play a significant role in the results of the electroplating process. They include:

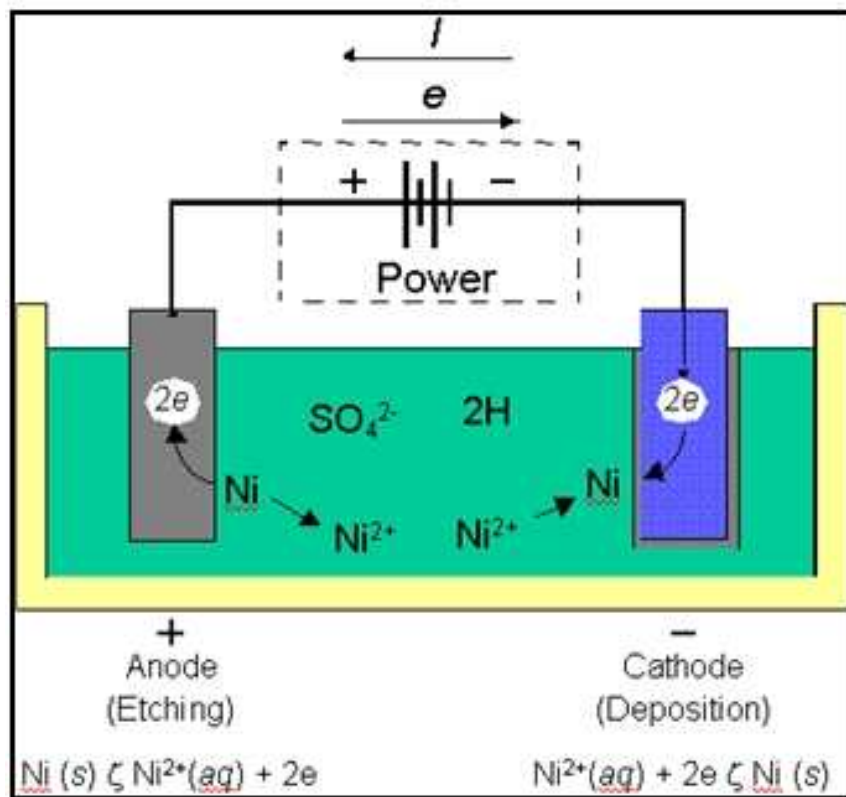


Figure 3.5: Process of Electroplating Nickel. An applied current flow causes nickel ions to be removed from the anode and deposited on the cathode. [5].

- Wafer Preparation: The best results will be achieved by using a fresh, clean wafer. One must avoid having any oxidation or other foreign material on the surface of the wafer prior to being placed in the electroplating bath. If a foreign material is on the substrate prior to the plating process, then the new material will not be able to adhere as well as if there was a clean surface to be plated to.
- Seed Layer: The seed layer is of the utmost importance. It provides an interface between the wafer material and the metal to be electroplated. Electroplating would not occur without a seed layer and certain metals provide better seeds for nickel than others. The best seed layers for nickel plating will be investigated later in this research.
- Bath Composition and State: There are numerous solutions of nickel baths available for purchase. Some provide lower stress while others offer a more shiny

surface. In addition, as the bath is used over time the composition is changed and the pH is changed, which will alter results over time. The temperature of the bath during the process is another critical parameter that must be adjusted to obtain desired results. One must also consider that when the bath is stored at high or low temperatures, this could potentially lead to the solution becoming hydrolyzed. Hydrolysis is the decomposition of the original solution molecules, and for some plating baths, the hydrolyzed solution is less soluble and tends to lead to increased tensile stress [21].

- Forward and Reverse Current Density: The current density determines how rapidly the plating process will occur. A reverse density is typically used in order to produce an even distribution across the surface being plated. The edges of the sample usually experience a much higher current than the center and, therefore, are plated more rapidly. A reverse current causes some of that excess to be released. A correct balance of the two should produce a uniform distribution across the surface.
- Duty Cycle: Not only must one consider the amount of forward and reverse current to use, but the amount of time that each direction is applied should be considered as well. The duty cycle is usually expressed as a ratio such as “60/40”. This denotes that 60% of the duty cycle is made up by the forward current and the 40% is made up of the reverse current.
- Time: The total amount of time the sample is in the bath with the current being applied determines the thickness of the plating. It can be expressed in two forms: minutes or amp-minutes. Minutes is the amount of time that the sample is actually in the bath. Amp-minutes denotes the number of minutes that a full amp of current is being applied to the sample. This is usually the number that is input into the electroplating power supply. The relationship is therefore stated: amp-minutes is equal to the average forward current multiplied by plating time.

- Position of Anode: The proximity of the anode to the sample makes a significant difference in the plating process, for if the anode is placed closer to the sample cathode, then the plating process will be accelerated. Therefore, the forward and reverse current and the amount of time in the bath will have to be altered in order to account for this.

As one can see, many parameters will affect the process for depositing the magnetic material. Chapter IV will discuss the fabrication process used for the microgenerator and Chapter V will present the results observed from depositing the nickel.

*3.2.4 Magnetization of Nickel Deposit.* In determining the proper method for magnetizing, or polarizing, the rotor arms one must consider the orientation to be used with the rotor magnets and stator coil. As discussed earlier in this chapter, in order to maximize current density, one must ensure that the direction of field variation, direction of the  $B$  fields, and the flow of current are all mutually orthogonal. Figure 3.6 provides a representation of an orientation that provides such orthogonality. This figure contains one of the varieties of magnetic rotors (grey) and stator coils (gold) to be fabricated. The arrows provide an illustration of the magnetic field lines produced when the magnets are polarized top to bottom as shown. When rotated, the field lines will be perpendicular to the direction of rotation as well as to the direction of current flow in the coils, satisfying the requirements for optimal current density.

Given that nickel is a ferromagnetic material, significant polarization can be accomplished by placing the deposited nickel in a strong external magnetic field. This external magnetic field aligns the electron spins within the nickel, thereby magnetizing the nickel. By adding heat to the process, the alignment occurs more quickly. The extra energy allows more atoms to align properly faster. As long as the nickel does not experience excessive heat or kinetic energy, then it will remain polarized.

Optimally this polar alignment would be accomplished *in situ* as the nickel is deposited. However, available resources do not allow for this. For this reason a Hall Measurement System manufactured by LakeShore will be used to polarize the nickel

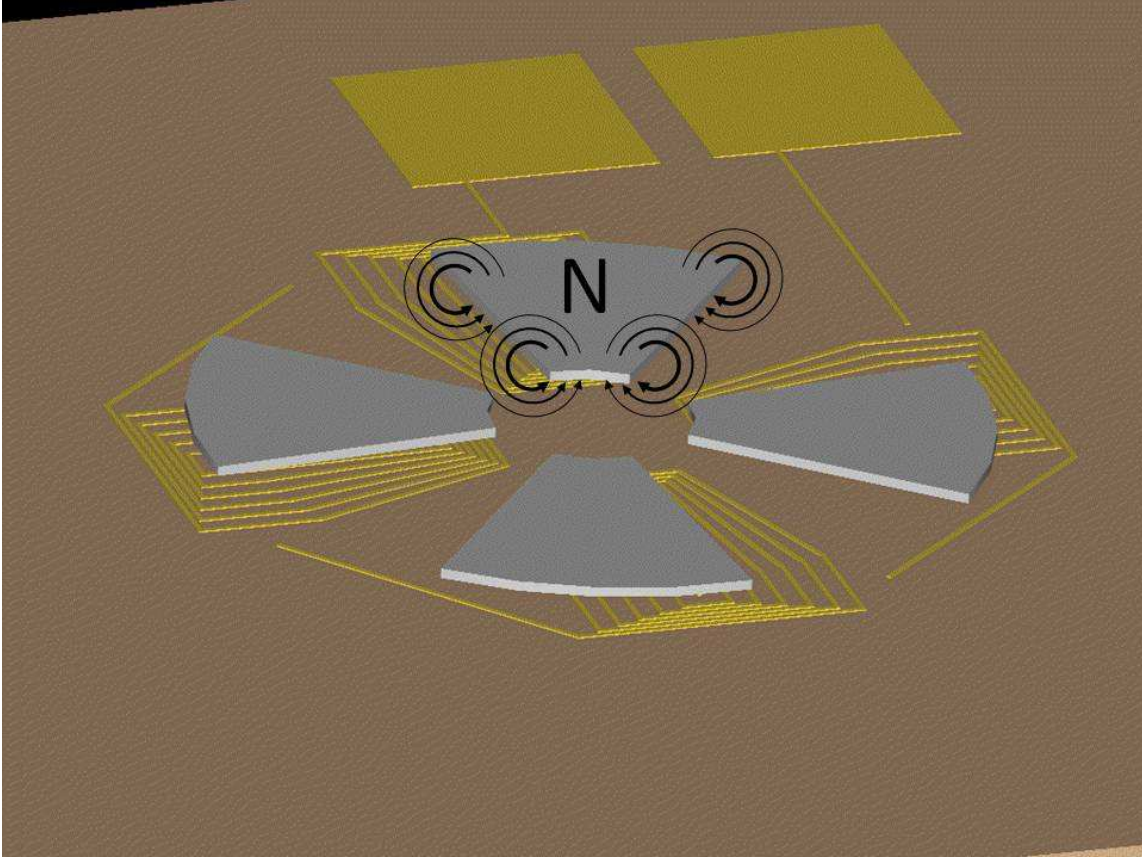


Figure 3.6: Orientation of the rotor magnets and stator coils of the micro-generator using the 4-arm segmented toroidal rotor and 6-turn arrayed angular stator. The rotor magnets (grey) are polarized top/bottom, meaning that the top of the rotors are the north pole, marked with an "N", and the bottom is the south pole.  $B$  field lines are represented by the arrows. All rotor arms are polarized the same. As the rotor revolves above the coils (gold) a current is induced in the coils.

after deposition. The Hall Measurement System can provide strong, controllable magnetic fields through the use of an electromagnet. The fabricated rotor magnets will be placed in the Hall System and the electromagnets will be turned on to a predetermined field strength. This should provide enough of a field to polarize the rotor magnet domains. A magnetic field probe will be used to measure the strength of the resulting flux density of the magnets.

Table 3.3: Resistivity of Common MEMS Compatible Metals at 20° C [22,23]

Material	Resistivity $\rho$ ( $\Omega - m$ )
Copper	$1.678 \times 10^{-8}$
Gold	$2.214 \times 10^{-8}$
Aluminum	$2.65 \times 10^{-8}$
Tungsten	$5.28 \times 10^{-8}$
Zinc	$5.9 \times 10^{-8}$
Nickel	$6.93 \times 10^{-8}$
Chromium	$12.5 \times 10^{-8}$
Titanium	$42 \times 10^{-8}$

### 3.3 Coil Design

Referring back to Table 3.1, we can see that two parameters are purely dependent on the coil design: resistance of the coil and the number of turns in the coil. In addition, one must ensure that the orientation of the coil to the magnet induces the desired current. All of these parameters will be discussed in this section as well as the resulting coil designs for this effort.

*3.3.1 Coil Material Selection.* Resistance is a measure of how easily a current can flow in a material. Analytically it is defined by the equation

$$R = \frac{\rho L}{A} \quad (3.4)$$

where  $R$  is resistance,  $\rho$  is the resistivity of a material,  $L$  is the length of the path the current is flowing through and  $A$  is the cross sectional area of that path. Resistivity is a material constant and, by Equation 3.4, is directly proportional to resistance. Table 3.3 provides a list of some metals commonly used with microelectronics and their respective resistivity values. Copper has the lowest resistivity, but oxidizes quickly when exposed to air. Oxidation causes difficulty in making good metal-to-metal connections when multiple depositions are used. Gold was selected as the material for the coils because it has the second lowest resistivity and does not oxidize. Low resistivity leads to low resistance and, thereby, less power loss in the coils.

*3.3.2 Coil Layout.* In designing the layout of the coils, numerous aspects need to be taken into consideration to optimize the power output of the micro-generator. These include the following:

- Cross-Sectional Area and Length of Wires in the Coil
- Design Current Path from Center of Coil Without Shorting the Circuit
- Orthogonality of Current Flow to  $B$  Field and Flux

*3.3.2.1 Cross-Sectional Area and Length of Wires in the Coil.* Equation 3.4 defines resistance as inversely proportional to the cross-sectional area of the wires and directly proportional to the length of the wire. Given that information, the coil layout should be as short in length as possible with a cross-sectional area as large as possible in order to lower resistance and thereby maximize power output.

Cross-sectional area is easily varied by increasing the amount of gold that is deposited for each coil, thereby changing the thickness of the coil. Width of the coil could also be varied to increase cross-sectional area. It was decided to keep width constant among all the coils to assist in standardizing the testing of the generator power output. All coils presented in this thesis have a wire width of  $10\ \mu\text{m}$ .

Regarding the length of the wire coils, there is a tradeoff that needs to be managed. As discussed at the beginning of this chapter, one of the parameters that plays into the efficiency of the overall generator is the number of turns in the coil. However, as you increase the number of turns, you also increase the length of the current path and therefore the resistance and power lost in the coil, as illustrated with the plot in Figure 3.7. It must also be remembered that this is to be a micro-generator. Increasing the number of turns translates into significant increases in size of the layout footprint due to the planar nature of the design. For example, a 12-turn angled coil requires 51% more device surface area than the 6-turn angled coil. For this effort, coils with 14, 12, and 6 turns were designed and fabricated.

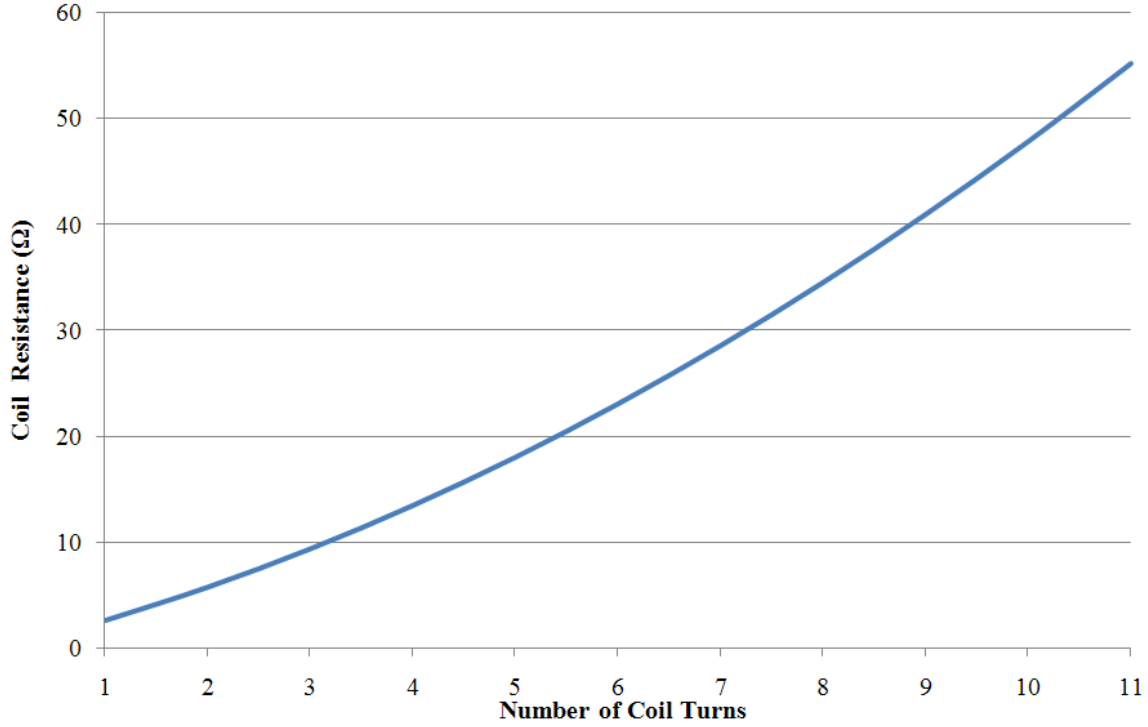


Figure 3.7: Resistance versus the number of turns in the angled coil. This plot shows how resistance increases as additional turns are added to an angled coil. An additional turn requires an increase in the length of the coil which causes an increase in resistance. Note the slight downward bow of the line as well. This is caused by the fact that each additional turn is slightly longer than the previous turn due to the concentric circles.

*3.3.2.2 Design Current Path from Center of Coil Without Shorting the Circuit.* Since this micro-generator design is intended to be planar, the coils will be based on a concentric circle model. This inherently leads to a requirement to create a current path from the center of the coil to the outside of the coil without shorting the circling coil. The MFPG design suggested running a wire underneath the coil from the center [5]. Silicon Nitride ( $Si_3N_4$ ), a very effective dielectric commonly used in the MEMS process, was used as a barrier between the circling coil and the runner line. A hole etched through the nitride layer provides a via from the coil to the runner.

Using this method, Sprecher found that the resistance of the coils was higher than he had predicted. He attributed this to two potential factors. One was the use of titanium (Ti) as an adhesion layer for the gold deposit. Ti serves to promote adhesion

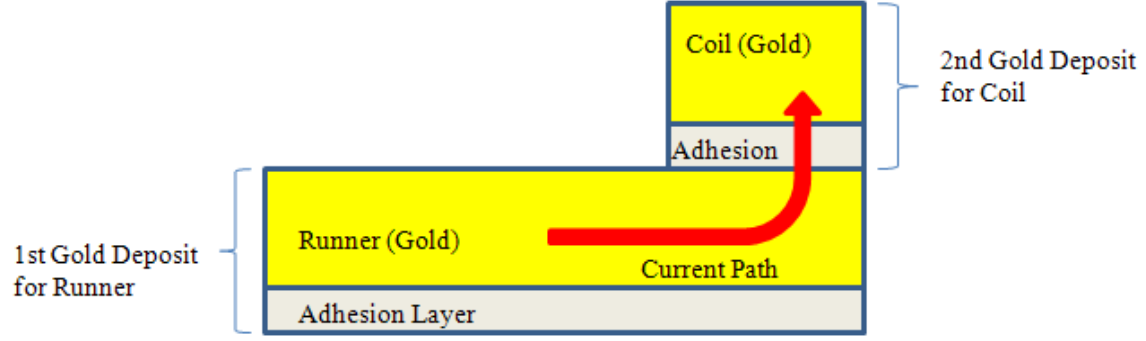


Figure 3.8: The effective resistance of the runner and coil is affected by the adhesion layer of the coil deposit due to the current path. The current does not flow in adhesion layer of the runner because it can freely flow in the gold, following the path of least resistance. However, the adhesion layer of the coil is unavoidable and will contribute to the effective resistance.

between the substrate and the evaporated gold. Referencing Table 3.3 one can see that Ti has a resistivity 30 times greater than that of gold. The effective resistance of the runner deposit will not be affected by the adhesion layer because current always follows the path of least resistance, meaning that it will flow in the gold and not in the titanium. Figure 3.8 depicts the current path in the runner and in the coil. However, if a runner is used as just discussed, then the second gold deposit for the coil will also require a Ti adhesion layer. This Ti layer, which is typically 200 Å thick, will serve as an unavoidable path for the current as it flows between the runner and the coil and will increase the effective resistance of the coil [5]. Since the thickness is only 200 Å for these adhesion layers, the increase in resistance is almost negligible, in the range of tens of  $\mu\Omega$ . Should this increase in effective resistance be too detrimental to the power output, an improvement to address the Ti issue is to use Chromium (Cr) as an adhesion layer instead of Ti. The resistivity of Cr is almost 4 times less than that of Ti and is commonly used as an adhesion layer as well and would reduce the effective resistance even more. The resistance calculations can be found in Appendix A.

The other potential factor that Sprecher identified as a cause for increased coil resistance was the thinning of the gold coil deposit where it overlapped the runner wire [5]. When gold is deposited via evaporation the resulting deposit is non-conformal

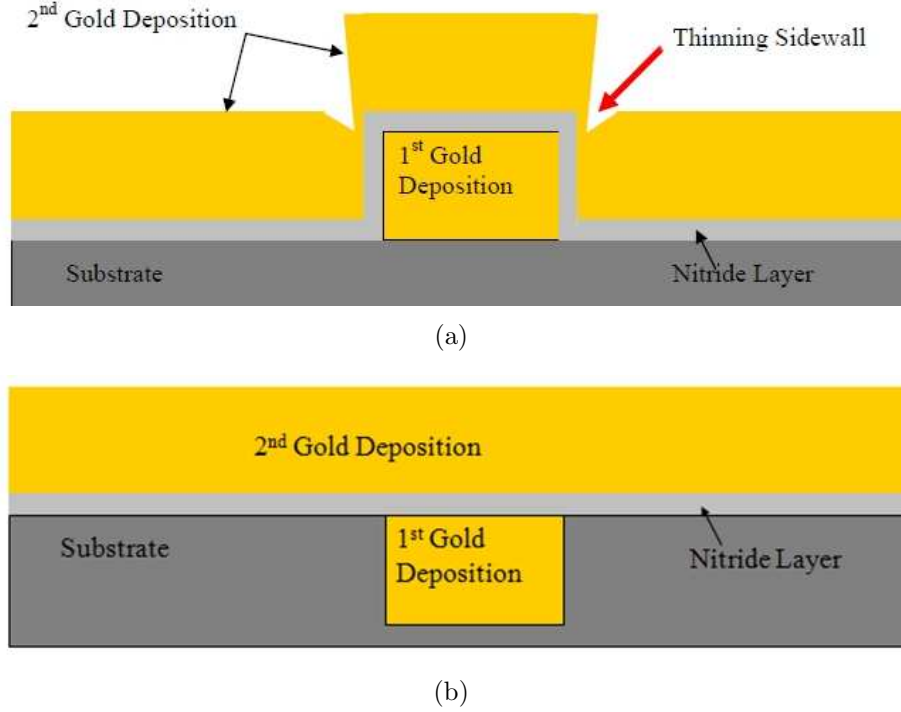


Figure 3.9: (a) Representation of the thinning sidewalls that could occur as evaporated gold is deposited over a previous runner deposit. (b) Potential solution to the thinning sidewalls is to create a trough for the runner wire [5].

in nature. This means that the material is deposited mostly on the top and does not adhere well to side walls. Given that the runner, encased by the nitride, has created sidewalls for the coil deposit, this could cause very thin gold deposits for each intersection of the runner and the coil. Figure 3.9 (a) provides an illustration of this sidewall thinning. Should this occur, not only would the resistance of the coil be increased due to the smaller cross-sectional area of the thinning walls, but it could also lead to burning out, and an open circuit, if too much current is drawn through such a small amount of wire.

Sprecher proposed etching a trough for the runner prior to the actual runner deposit to eliminate the sidewall thinning [5]. Figure 3.9 (b) provides an illustration of such a solution. This will be the method adopted for the current effort.

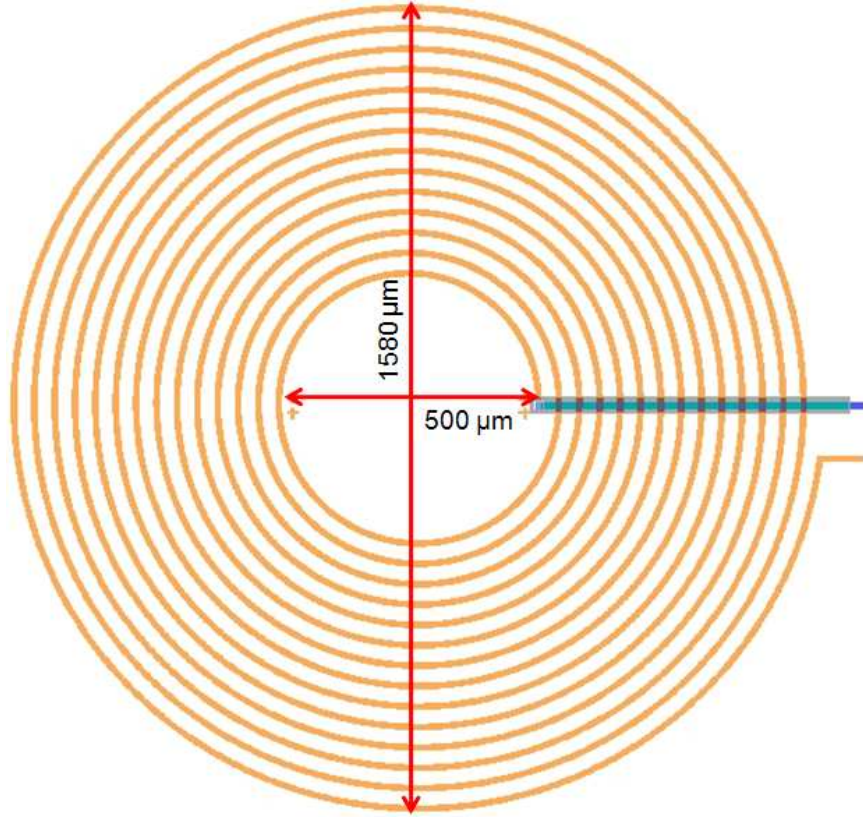


Figure 3.10: Original MFPG Coil Layout. A single concentric coil with 14 turns (gold) had a runner (blue) covered by silicon nitride (grey) providing a path from the center of the coil [5]. The line widths are  $10\ \mu\text{m}$  and the line spacing is  $30\ \mu\text{m}$ .

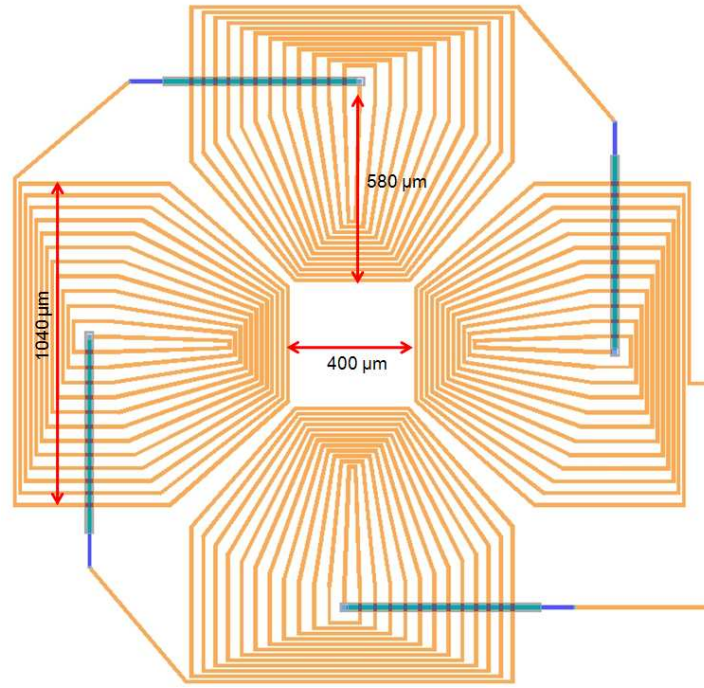
*3.3.2.3 Orthogonality of Current Flow to  $B$  Field and Flux.* The flow of current in the coil layout needs to be mutually orthogonal to the direction of change in field strength and  $B$  field lines. This was the driving parameter in the development of new coil layouts.

The original MFPG design used a single concentric coil. Figure 3.10 provides the L-Edit image of the design used for testing in this effort. Notice that the runner covered with silicon nitride was used to provide a current path out of the center of the coil just as was originally proposed in Sprecher's work. However, it must also be pointed out that the original design intended the center of rotation of the rotor magnet to be the center of the coil. If a top/bottom polarization is used for the magnets with this design, the  $B$  field lines will be orthogonal to the current flow,

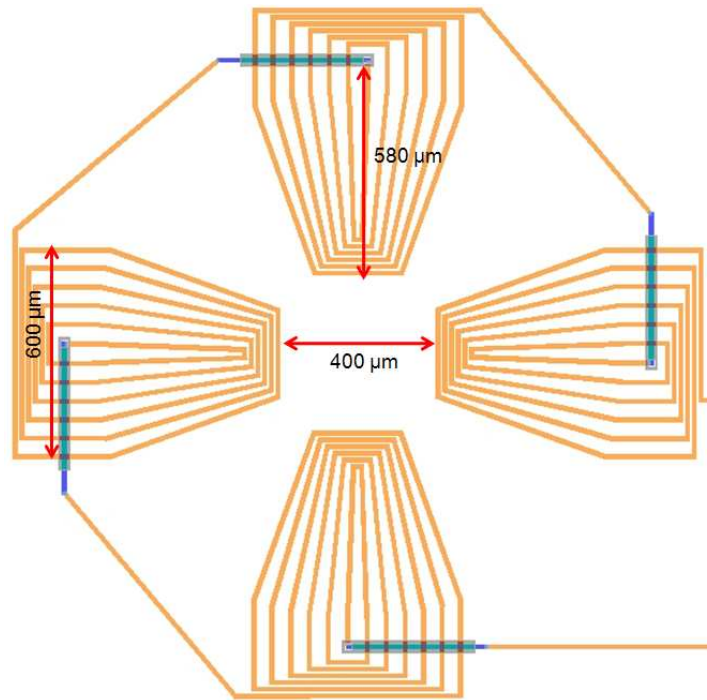
however, the direction of the magnetic flux would be in the same direction as the intended flow of current. As discussed earlier, this would lead to a less than optimal current density, if any at all. The next two designs presented offer a variation of the original MFPG design that should optimize the current density.

The object of the new design is to have the direction of current flow purely orthogonal to the direction of magnetic flux caused by the rotation of the rotor magnets. In order to do this, the coil wires need to be aligned with radial lines from the center of rotor rotation. This requirement led to a new design consisting of an interconnected polar array of angular coils centered on the rotor magnets center of rotation. Figures 3.11 (a) and (b) provide images of the angular coil designs developed using L-Edit. As shown in Figure 3.11, the runner wire was covered by silicon nitride to provide the current path from the center of the coils for both designs. The difference between the two is simply the number of turns contained in each coil. Figure 3.11 (a) contains 12 turns and (b) contains 6.

It turns out that the 6-turn angular coil aligns very well with the 4-arm toroidal rotor as can be observed in Figure 3.6. It is anticipated that this combination of rotor and coil placement will provide the highest power output of all potential combinations of the rotors and coils presented in this chapter. In order to understand the reason for such an assumption, one must recall the right-hand rule as it pertains to the Ampère-Maxwell Law discussed at the beginning of this chapter. Using the right-hand rule with the  $B$  fields at the edge of each magnet arm, such as those illustrated in Figure 3.6, one can recognize those fields induce currents opposite in direction of one another; the current on one side of the magnet flows in the opposite direction as that on the other side of the arm. Therefore, optimally the arm will be the same size as the coil, or very close, so that the currents are effectively combining for maximum current density. If multiple magnets are covering one coil then the currents might completely cancel with each other and the effective current flow would be zero.



(a)



(b)

Figure 3.11: An array of 4 interconnected angular coils (gold) distributed evenly around the center of rotor rotation provides current paths purely orthogonal to the direction of rotation. A runner (blue) covered by nitride (grey) provides a current path from the coil centers. (a) has 12 turns whereas (b) only has 6. Line widths are  $10\ \mu\text{m}$ . Line spacing is  $7\ \mu\text{m}$  on the inside and outside of the array and varies along the polar rays.

### 3.4 Test Structure

The original MFPG design was intended to function using a turbine actuated by blood flow in order to move the rotor. Such a design is very complicated and exceeds the scope of this effort, therefore, in order to test the power output of the stator coil and rotor magnet designs presented in this chapter, a test structure is required. The general idea for the test structure is to align a rotor and an inverted coil within close proximity, revolve the rotor, and measure the output current of the coil. The test structure, therefore, needs to perform three main functions: provide a rotation mechanism for the rotor, allow for precise alignment of rotor and coil, and measure power output.

*3.4.1 Rotation Mechanism.* The testing apparatus should simulate the rotation that might be provided by a turbine interfacing with blood flow. Sprecher calculated the rotation rate provided by typical human blood flow to be approximately 39.3 RPM [5]. This rotation rate will serve as a starting point for the current research. In addition, the rotation device needs to be able to provide a consistent planar surface given that it will serve as a stage for the rotor and will be placed within tens of  $\mu m$  to the stator coils. Any fluctuations could cause the stator and rotor to come in contact and damage the devices.

Difficulty arises in finding a device that is accurate to such a slow rotation rate. Devices considered included a photoresist application spinner, rotary stage for optics tables, and a servo motor produced for a robot system built by LEGO<sup>TM</sup> Mindstorms NXT. Spinners are typically only accurate to about 100 RPM. Optics table rotary stages meet the rotation rate requirements and are excessively accurate but one was not available for this research. The LEGO<sup>TM</sup> motor is available and provides a variable RPM that meets the requirements.

*3.4.2 Precise Alignment.* The center of rotation of the rotor must be aligned very accurately with the center of the stator design in order for correct functionality.

This requires a tool that can provide minute alterations in orientation in all 6 degrees of freedom as well as imaging to verify alignment. Microstages, such as those fabricated by Klinger Scientific, can provide such precise control of orientation within a few microns. Multiple microstages are available and will be used in this effort.

Imaging is more complicated. Given that the stator and rotor must be in close proximity, it is very difficult to see between them to observe if they are correctly aligned. A solution is to take advantage of a system that is already designed for such imaging. A flip-chip bonder uses a special optical tool to align two microelectronics devices and bond them together. AFIT has an Eagle 860 flip-chip bonder. It is expected that a custom stage with micro controls and rotation capability could be built and used with the optics of this bonder. In order to facilitate with the alignment, rotors and stators will both be fabricated and centered on small chips of the same size,  $5000 \times 5000 \mu m^2$ .

*3.4.3 Power Output Measurement.* A technique for measuring the power output of the device must be considered as well. Power is defined by

$$P = \frac{V^2}{R} \quad (3.5)$$

where  $P$  is power in watts,  $V$  is voltage in volts, and  $R$  is resistance in ohms. In order to measure the power output of any device, a predetermined load, or resistance, can be placed in the circuit. The voltage drop across that load can be measured and, using Equation 3.5, one can determine the power output of the system.

Therefore, in order to measure the power output of the micro-generator, a resistor will be placed between the two electrodes of the coil. Two large gold pads connected to the coil will be included on the stator chips to facilitate the measurement. A wire bonder will connect a small wire to each pad and a resistor will be placed between them. A multimeter will be used to measure the voltage drop across the resistor and the power output will be determined using Equation 3.5 for multiple

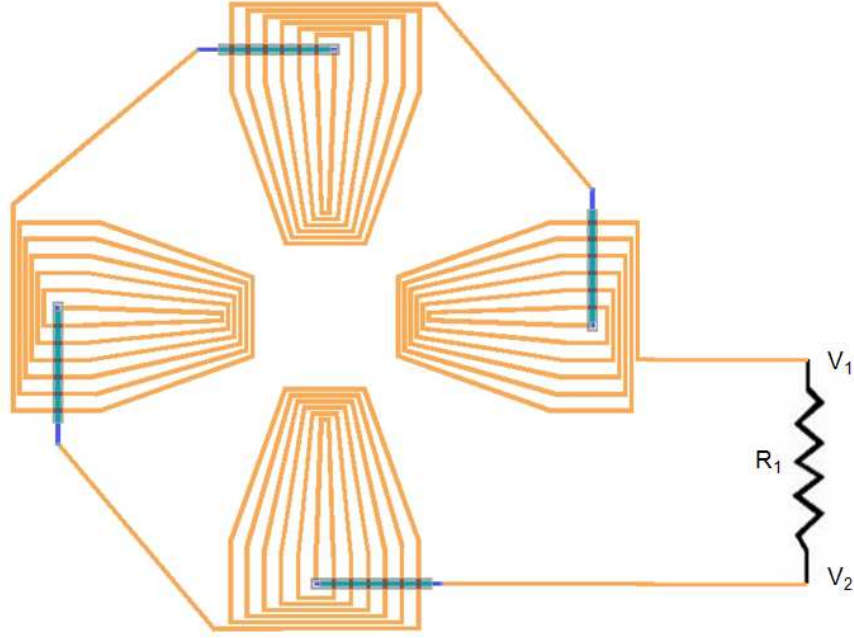


Figure 3.12: General schematic for testing power output of generator. The power output of the device can be derived from the voltage drop ( $V_2 - V_1$ ) across a known resistance ( $R_1$ ).

combinations of coils and stator magnets. Figure 3.12 illustrates a basic model of how the voltage will be measured.

### 3.5 Chapter Summary

This chapter focused on the problem solving approach used in this effort by detailing the design process for a micro-generator. Theory, materials and varying layout considerations were analyzed and discussed. The final coil and magnet layouts to be fabricated and tested, as drawn in L-Edit, were presented and the test apparatus design was detailed.

## IV. Fabrication

This chapter will discuss the physical results of applying the methodology and theory presented in Chapter III as it pertains to fabricating the micro-generator rotor magnets, stator coil and testing apparatus. Most steps of the fabrication process required a characterization of the tools in order to determine optimal settings. The characterization process will be discussed where appropriate and the selected fabrication parameters will be presented. Appendices B and C will serve as essential references for this chapter. Appendix B contains all information and imaging relevant to the lithographic mask used, and Appendix C contains details and step-by-step process followers of the successful fabrication methods found in this research.

### 4.1 *Mask Fabrication and Substrate Selection*

The first step in the fabrication process was to have a lithographic mask fabricated for patterning the designed features. The layout for the mask was created by compiling the L-Edit designs presented in the last chapter and dividing them into the separate processing steps. AFIT has its masks fabricated by Photo Sciences, Inc. of Torrance, CA. The mask substrate is a 4 inch square, but only a 3 inch diameter circle of that mask is available for patterning purposes. Given that each of the devices to be fabricated require only  $5000 \times 5000 \mu m^2$ , multiple smaller masks were included on a single 4 inch mask. In total, 7 distinct masks with dimensions of  $45 \times 15 mm^2$  were included. Details and images of the layouts contained on the mask are available in Appendix B.

A glass slide, similar to a microscope slide, was used for the substrate of the rotors. Originally transparent glass slides were selected to facilitate alignment of the coil and rotor. However, the current test structure does not require a transparent substrate, therefore future efforts could make use of other substrates if desired.

A silicon (Si) substrate was selected for the coil fabrication. Given that troughs need to be etched into the substrate for the runners, a substrate that can be etched

consistently was required. Crystalline silicon etches much more consistently than amorphous glass.

## 4.2 *Magnet Fabrication*

The magnet fabrication process utilized in this effort consisted of:

1. Depositing a seed layer.
2. Creating a pattern using the photolithography mask and photoresist.
3. Electroplating sufficient nickel material for the magnets.
4. Magnetizing the resulting devices.

This section will investigate the process used to accomplish each of these steps. (Given that the seed layer material selection is closely associated with the electroplating process, seed layer deposition will be discussed within the electroplating section of this chapter.)

*4.2.1 Photoresist Characterization.* Photoresist (PR) is a light-sensitive material that is used in photolithography processes. It is typically spun onto the surface of a wafer at high speeds to produce a uniform film thickness. It is then baked on a hot plate to evaporate off any solvents and to improve adhesion to the wafer. Once baked onto the wafer, the PR is exposed to a particular wavelength of light and developed using a specially formulated developer. For positive PRs, the exposed portion will dissolve off. A mask is used to define the pattern to be created [24].

Photoresists typically used at AFIT have a thickness of 1 to 2.5  $\mu m$ . However, for the micro-generator rotor magnets, the nickel deposit should be as thick as possible in order to produce stronger magnetic fields. Sprecher's original design proposed thicknesses of 20  $\mu m$  for the nickel deposit [5]. If 20  $\mu m$  thick nickel was deposited using the typical AFIT PRs, a mushroom shape would be created once the nickel deposit exceeded the height of the PR and would more than likely fuse together. Therefore, a thicker PR was investigated for this effort.

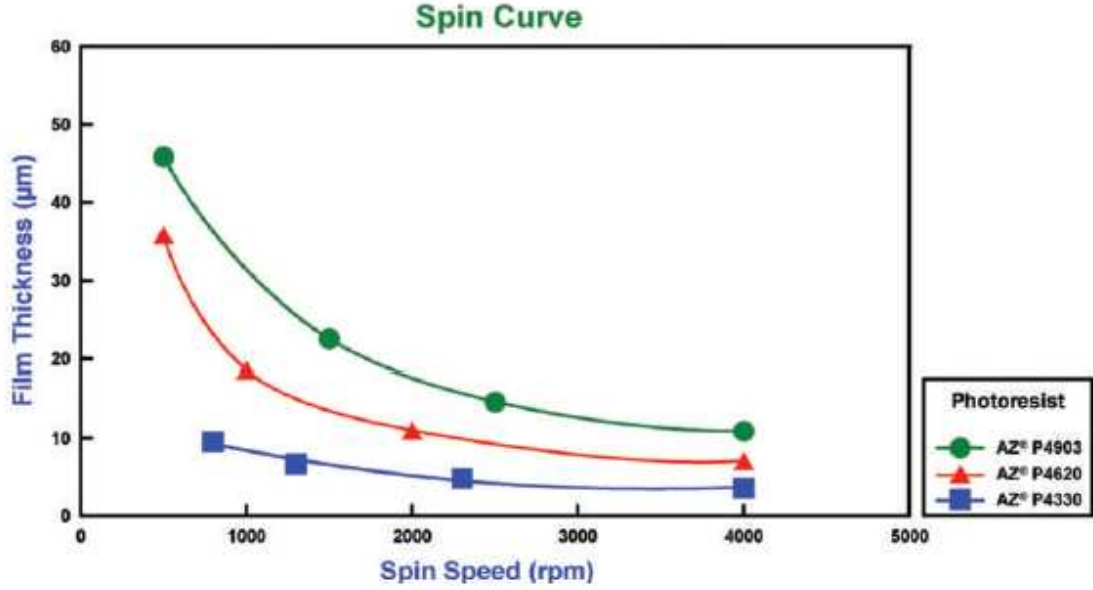


Figure 4.1: Spin Curve for AZ P4620. Provides associated thicknesses relative to spin speeds for the P4620 photoresist [25].

AZ P4620 is a PR produced by AZ Electronic Materials. It can be deposited to thicknesses ranging from 3 to 60  $\mu\text{m}$  [25]. This PR was selected to provide the pattern for the nickel deposit. Figure 4.1 provides a chart mapping spin speed to thickness for P4620.

The datasheet for this PR listed a double application process to acquire a 24  $\mu\text{m}$  thick film as well as a single application process that resulted in greater than 20  $\mu\text{m}$  thick film [25]. Both were investigated and the double application process was identified as the best choice given that it provided a more uniform and consistent PR spread.

The datasheet also listed a recommended constant exposure dose of between 1500  $\text{mJ}/\text{cm}^2$  to 1750  $\text{mJ}/\text{cm}^2$  [25]. Through experimentation using AFIT's EVG 620 mask aligner, it was found that this recommended dose was more than twice what was actually needed. Figure 4.2 provides images of the results of two different exposure doses. As can be observed in Figure 4.2 (a), the 1600  $\text{mJ}/\text{cm}^2$  exposure resulted in very rounded edges, indicative of over-exposure. A reduced exposure,

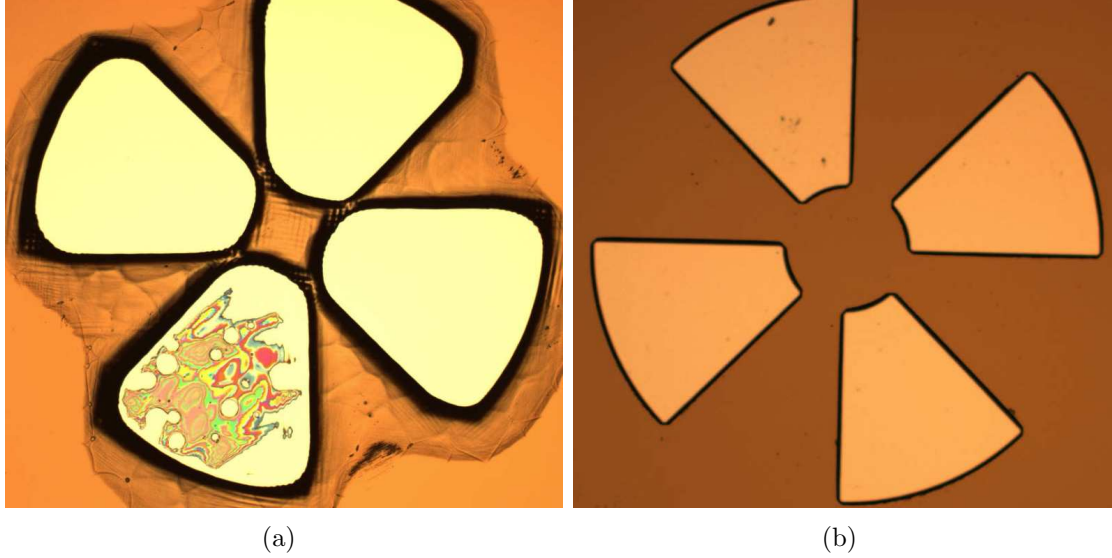


Figure 4.2: Exposure comparison of AZ P4620 lithography patterns. The recommended fixed dose exposure was higher than what was required with AFIT’s EVG 620 Mask Aligner. Using a fixed dose of  $1600 \text{ mJ/cm}^2$  resulted in very rounded edges as represented in image (a). A fixed dose of  $750 \text{ mJ/cm}^2$  produced much sharper lines, represented in image (b).

shown Figure 4.2 (b), produced much cleaner lines. The optimal dosage was found to be  $680 \text{ mJ/cm}^2$  with the EVG 620.

In addition, the high viscosity of the P4620 and the rectangular shape of the substrate slides resulted in significant edge beading. Some beading was measured to be 50% thicker than the center of the slide. With such variation in thickness a single exposure and development time could not be used for the entirety of the slide. For this reason only two rows of rotors were patterned in the center of each slide instead of the three rows originally planned. Doing so successfully avoided the edge beads and allowed for clean patterning. The entire process follower for the successful  $24 \mu\text{m}$  thick AZ P4620 application can be found in Appendix C.

*4.2.2 Nickel Plating.* This section will analyze the fabrication experiments completed in order to characterize the nickel electroplating bath as well as discuss the resulting process selected for the rotor magnet deposition.

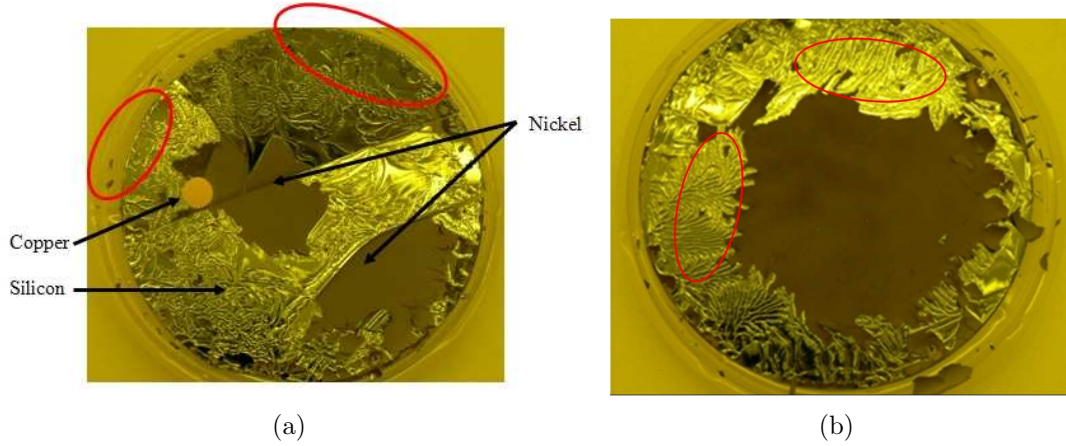


Figure 4.3: Delamination of Sprecher’s nickel electroplating samples. The delamination was caused by the high tensile stress introduced during the electroplating process and began immediately after being removed from the bath. For the first sample, (a), the circles identify where the delamination began. The second sample, (b), experienced such high stress that 30 microns of substrate, identified by the circles, were ripped up with the nickel deposition [5].

#### 4.2.2.1 Characterizing the Nickel Electroplating Bath With Full Wafers.

The nickel electroplating process described in Chapter III was used by Sprecher in an attempt to deposit enough nickel material to create a magnet. He used the nickel electroplating equipment at the Air Force Research Laboratory/Sensors Directorate (AFRL/Ry) located near AFIT. AFRL/Ry has a FutureFab bench that contains a nickel sulfamate solution in the bath. The power supply for the system is manufactured by Dynatronix.

The results of Sprecher’s experiments were not optimal. He plated two full patternless Si wafers to try to characterize the bath. Figure 4.3 provides images of the samples a few days after the electroplating. The brown area is where the nickel remained attached to the substrate. The silver area is where the tensile stress of the nickel was so great that it pulled away from the Si substrate. Tensile stress occurs when a material with a high coefficient of thermal expansion (CTE) is placed on a material with a low CTE. As the two materials cool, the deposited material with a relatively high CTE, in this case the nickel, contracts more rapidly than the Si substrate leading to tensile stress between the layers. As can be seen in Figure 4.3,

the tensile stress was tremendous, as the deposited material was unable to remain attached to the substrate.

It was assumed that something was wrong with the nickel sulfamate solution in the bath and that an additive, saccharin, needed to be placed in the nickel plating solution in order to reduce the stress [5]. Saccharin has been shown to reduce the tensile stress in the plating process. However, it also reduces the purity of the nickel being deposited and therefore would most likely reduce the magnetic properties as well [26]. AFRL/RY ordered the saccharin to be deposited into the bath, but it did not arrive in time for Sprecher to perform more experiments prior to the completion of his thesis work.

A few months after Sprecher completed his thesis work, a lab notebook containing plating experiment information that was completed in 2004 was discovered by AFRL/RY. The experiments were performed by Matthew Williams in an attempt to characterize AFRL/RY's nickel electroplating bath. The data contained in this notebook was compiled and can be found as part of Table 4.1. All experiments up to NP50 were conducted by Williams, whereas ASNi1 and ASNi2 were Sprecher's samples previously mentioned. Williams varied many of the plating parameters to determine optimal settings for nickel deposition using AFRL/RY's nickel plating equipment [27]. Even though not all of the parameters for each sample were recorded in the notebook, much information can be gleaned from the data presented in Williams' work.

Upon inspection of the data, some trends were observed. It appears that high deposition rates, greater than  $0.1 \mu\text{m}/\text{A} - \text{min}$ , tend to lead to increased peeling and cause the surface to become more cloudy. As discussed earlier, peeling is caused by an increased tensile stress. In addition, it also seems that an optimal balance between the forward current density and the reverse current density must also be found in order to avoid tensile stress. Samples NP21 to NP25 demonstrate this. The first samples had a lower reverse current density and the deposition rate was high, leading

Table 4.1: Nickel Electroplating Experimental Data [5, 27]. Yellow highlighting indicates changes from previous run.

Sample Name	Seed Layer (Å)	Fwd Cur (A)	Rev Cur (A)	Dty Cyc	A-min	Time (min)	Near Anode	Center Thickness (μm)	Delta (Edge/Center)	Deposition Rate (μm/min)	Peeling Pitting?	Cloudy?	Notes
Mat1	2000 Cu	0.8	0.8	50/50	12	15		3.000	1.5000	0.2000			
Mat2	2000 Cu	0.8	0.8	50/50	12	15		0.065	0.6923	0.0043	No		No additional deposit, possibly oxidation
Mat2b	cont.	0.8	0.8	60/40	12	15		No Change	N/A				
NP20	200 Ti/2000 Cu	0.8	0.8	60/40	12	15		0.030	1.6667	0.0020	No	No	
NP21	200 Ti/2000 Cu	0.8	0.2	60/40	12	15		1.600	1.8750	0.1067	Edges	Cloudy	
NP22	200 Ti/2000 Cu	0.8	0.4	60/40	12	15		1.000	1.6000	0.0667	Little on Edges	Little	
NP23	200 Ti/2000 Cu	0.8	0.5	60/40	12	15		0.700	1.7857	0.0467	No	Shiny	
NP24	200 Ti/2000 Cu	0.8	0.55	60/40	12	15		0.710	0.0000	0.0473	No	No	Less Metal on Edges (high Rev?)
NP25	200 Ti/2000 Cu	0.8	0.525	60/40	12	15				0.0000			
NP25b	cont.	0.8	0.525	60/40	12	15		1.400	2.0000	0.0933	No	Slight	
NP26	200 Ti/2000 Cu	0.8	0.525	60/40	12	15	Yes	1.000	1.3000	0.0667	No	Some	
NP27	200 Ti/2000 Cu	0.8	0.525	60/40	40	50	Yes	3.300	1.2121	0.0660	No	Very Shiny	
NP28	Patterning Tests												
NP29	Patterning Tests												
NP30	200 Ti/1000 Ni	0.8	0.525		8	10	Yes	0.600	1.3333	0.0600	No	Very Shiny	
NP31	200 Ti/1000 Ni	0.8	0.525		45	56.25	Yes	3.270	1.2232	0.0581	Some Pitting	Very Shiny	
NP32	Patterning Tests												
NP33	200 Ti/1000 Ni	0.8	0.525	60/40	45	57	Yes	3.800	1.5263	0.0667	Reduced Pitting	Shiny	Bath Changes
NP40 (2")	1000 Ni	0.4	0.262				Yes						Error
NP41 (2")	1000 Ni	0.2	0.131				Yes						Error
NP42 (2")	1000 Ni	0.4	0.262		20	50	Yes	4.800		0.0960	No		Edges look thin
NP43			0.26		14								
NP50	mounted on quartz												
ASNi1	200 Cr/700 Cu	10		40/60	18	39.5		8.000		0.2025	Yes	N/A	Serious Peeling
ASNi2	200 Cr/700 Cu	10		40/60	18	39.5		8.000		0.2025	Yes	N/A	Serious Peeling
NiStr1	1000Ni	0.8	0.52	60/40	45	56.25	Yes	2.930	1.8771	0.0521	Very little on Edges	On edges	
NiStr2	1000Ni	0.8	0.5	60/40	45	56.25	Yes				Little on Edges	On Edges	
NiStr3	1000Ni	0.8	0.5	60/40	45	56.25	Yes				Very little on Edges	On edges	Not as bad as NiStr1
NiStr4	1000Ni	0.8	0.35	60/40	45	56.25	Yes	N/A			Yes	N/A	Moved Anode Closer...stripped seed and chunks everywhere
NiStr5	1000Ni	0.5	1.5	75/25	40	80	Yes	N/A	0.0000		No	No	Stripped Seed no new plate
NiStr6	1000Ni	0.8	0.35	60/40	40	50	Yes				Yes	N/A	Serious Peeling
NiStr7a	1000Ni	10		40/60	18	39.5	Yes	8.000		0.2025	Yes	N/A	Serious Peeling
NiStr7b	200 Ti/2000 Cu	0.8	0.525	60/40	40	50	Yes	3.000	1.5833	0.0600	No	Very Shiny	
NiStr8	200 Ti/1000 Ni	0.8	0.525	60/40	40	50	Yes	3.600	1.3333	0.0720	No	Cloudy on edge	

to some peeling. However, as an optimal reverse current was approached, the peeling stopped.

It was also noted that even though the deposition rate of NP26 was the same as that of NP22, no peeling occurred with NP26 and it had a more uniform deposition. This seems to indicate that the deposition rate might not be the best method of stress control. There were two parameters that were changed between these two samples: proximity to the anode and the reverse current. Further testing was required to identify which parameter induced the high stress.

Williams also tried different seed layers. It appears, from the recorded data, that there was not much difference between the 200 Å Ti/2000 Å Copper (Cu) seed and the 200 Å Ti/1000 Å Ni seed. In fact the two runs with the least peeling and shiniest surfaces were done with these two seeds, samples NP27 and NP33. AFIT does not have the capability to deposit Cu, therefore the 200 Å Ti/1000 Å Ni will be used as the seed for this effort.

After compiling this data and combining it with the results of Sprecher's experiments, samples ASNi1 and 2, some additional experiments were designed and conducted by this author and some of the staff at AFRL/RV on full 3-inch wafers. Table 4.1 contains the parameters from the most recent full wafer experiments as well, NiStr1 to NiStr8. It must be noted that the saccharine additive was not added to the solution before the most current experiments began. Therefore the solution that was used by Sprecher and the solution that was used for the current sample set, NiStr1 - 8, are the same.

Of the new batch of experiments, the most informative were NiStr3, NiStr4 and NiStr6. NiStr3 had very little peeling. For NiStr4, two parameters were varied from NiStr3, proximity to the anode and reverse current; similar to the variation of NP22 and NP26 previously mentioned. Serious peeling was observed with NiStr4. Sample NiStr6 was an attempt to identify whether the excessive stress of NiStr4 was due to moving the anode closer or reducing the reverse current. For NiStr6, the anode was

left in the normal position and only the reverse current was reduced. The stress was still present. Therefore it is concluded that the stress is at least partially caused by the change in reverse current. In addition, since moving the anode closer to the sample should only increase the deposition rate (which can easily be varied by altering the forward current), the anode should be left in the normal position for all additional plating runs.

NiStr7a, NiStr7b, and NiStr8 were duplicates of previous processes in order to verify that one could recreate the results of previous experiments. NiStr7a was a duplicate of Sprecher's work. The only difference was the seed layer. A nickel seed was used instead of a chromium/copper seed. The results however were almost identical. (An image was unavailable but it appeared very similar to Figure 4.3.) Upon closer inspection of the parameters that were used and the deposition rate, one can recognize that high stress would be expected. These parameters produce a deposition rate of more than  $0.4 \mu m/A - min$  and no reverse current was used.

NiStr7b and NiStr8 used the same process as NP27 and NP33, respectively, and produced the best results seen during this round of experimentation. In addition, the results mirrored Williams' tests. Given that successful platings were accomplished using the same bath but different parameters, it was determined that the saccharine additive was not needed to reduce the stress. Images of the wafers after the electroplating process can be seen in Figure 4.4. The forward and reverse current densities used for these wafers ( $17.5 mA/cm^2$  and  $11.5 mA/cm^2$ ) will be the starting point for the parameters to be used on the patterned samples discussed in the next section.

In summary, lessons learned from characterizing AFRL/RYS's nickel plating bath with full size wafers include:

1. High stress deposits lead to delamination of the nickel deposit.
2.  $200 \text{ \AA}$  Ti/ $1000 \text{ \AA}$  Ni provides a good seed layer for nickel and will be used as the seed for this effort.

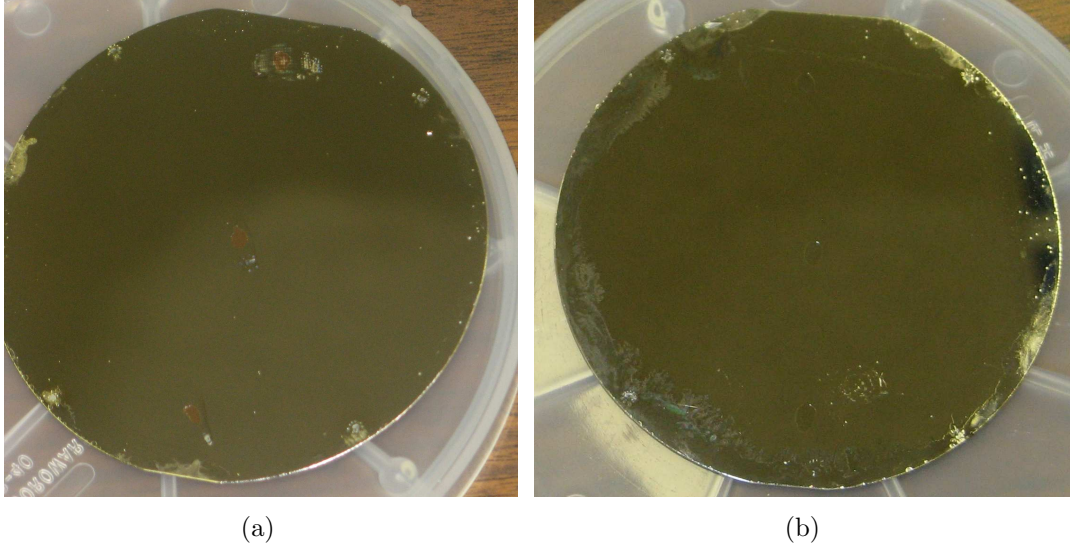


Figure 4.4: Samples (a) NiStr7b and (b) NiStr8 after electroplating process. No delamination is observed.

3. Deposition rate is not a good method of stress control. Various deposition rates should be achievable with success.
4. A proper balance of forward and reverse current densities is the best method of stress control. A forward to reverse current ratio of 1.52 with a 60/40 duty cycle was found to be successful.

#### 4.2.2.2 Characterizing the Electroplating Bath With Patterned Samples.

As discussed in Chapter III and the previous section, the determining factor for the deposition rate and quality of the deposit was the balance of the forward and reverse current density. Current density is a function of the current and the area of the sample to be plated. A 3-inch wafer has a surface area of  $45.6 \text{ cm}^2$ . For all the experiments discussed in the previous section the entirety of the surface of the wafer was being plated, therefore the current density can be calculated by dividing the forward and reverse current by the entire surface area. Using the forward and reverse current parameters from NP27 and NP33, the optimal forward and reverse current density can be found to be  $17.5 \text{ mA/cm}^2$  and  $11.5 \text{ mA/cm}^2$  respectively, as mentioned in

the previous section. (Calculations were accomplished using MathCad<sup>TM</sup> and can be found in Appendix A).

To calculate the forward and reverse currents to use for patterned samples, the new surface area of the exposed seed needs to be calculated. Calculating the exposed surface after patterning was simplified greatly through the use of a tool found in L-Edit. Using the area calculation tool, it was found that the covered portion of the slide had an area of  $6.592\text{ cm}^2$ . However, in order for a sample to function with the electroplating system, electrodes must be directly attached to the seed of the sample. To make this contact, one half of the alignment squares from each side of the sample had to be removed with acetone and must be accounted for in the exposed surface area calculations. Subtracting the final covered area from the actual area of the entire slide provides an exposed seed area of  $0.439\text{ cm}^2$ . Multiplying this area by the forward and reverse current density from NP27 and NP33 gives the forward and reverse currents for the patterned samples,  $0.0077\text{ A}$  and  $0.0051\text{ A}$ .

AFRL/RYS Dynatronix power supply has a forward and reverse current resolution of only  $0.001\text{ A}$  and it has difficulty controlling currents below  $0.010\text{ A}$  effectively. Therefore, small currents such as those just calculated are difficult to achieve with accuracy. In addition, the current parameter input into the power supply controller is not exactly what is actually passed through the sample. A current monitor does provide the actual current draw during deposition so that the input can be adjusted to provide the desired current flow. Considering these limitations, it is not surprising that the use of the currents calculated in the previous paragraph was not successful and resulted in the removal of the seed layer or very minimal deposit, less than  $1\text{ }\mu\text{m}$ .

In order to overcome the inaccuracies at small currents, larger currents were used. During characterization of the full wafers, it was inferred that higher plating rates and current densities should be achievable as long as a proper balance of forward and reverse currents is maintained. Based on this conclusion, the currents were adjusted to  $0.081\text{ A}$  for forward current and  $0.053\text{ A}$  for reverse current, which main-

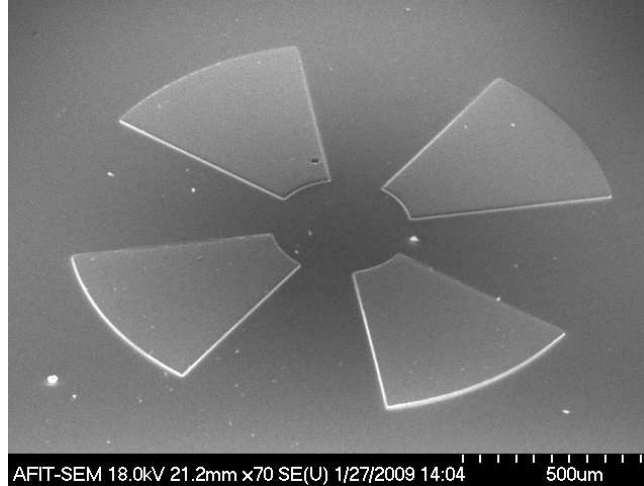


Figure 4.5: SEM image of successfully plated toroidal rotor. This rotor is  $8\ \mu\text{m}$  thick and no peeling is observed.

tains the ratio of forward to reverse current previously found of 1.52. These currents lead to current densities of  $182\ \text{mA}/\text{cm}^2$  and  $121\ \text{mA}/\text{cm}^2$  respectively. The resulting deposition rate was approximately  $0.4\ \mu\text{m}/\text{min}$  and no peeling or discoloration was observed. Figure 4.5 provides a scanning electron microscope (SEM) image of one of the successfully electroplated rotors resulting from this process. The variation in plating thickness across the slide was significant, however, resulting in rotors with thicknesses of up to  $14\ \mu\text{m}$  on the edges and only  $7\ \mu\text{m}$  thick in the middle.

In an effort to reduce the thickness variation, the reverse current was slightly increased relative to the forward current leading to a forward/reverse ratio of 1.463, with forward current at  $0.06\ \text{A}$  and reverse current at  $0.041\ \text{A}$ . Peeling was once again observed. Figure 4.6 provides an SEM image of the resulting delamination. It appears even slight changes in the forward to reverse ratio will affect the stress of the deposit.

Given that the ratio needs to stay the same, it appears that an appropriate method to reduce the variation in thicknesses would be to use a different shaped sample. The rectangular samples used in this effort allowed for one electrode attachment on each end and lead to high current densities on the edges near the electrodes and smaller current densities toward the center of the sample. Round samples would al-

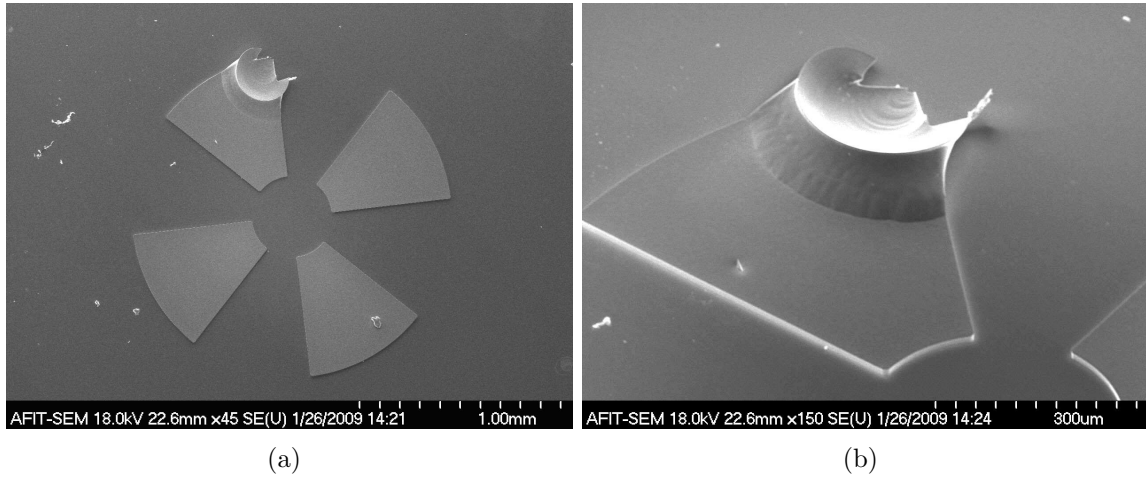


Figure 4.6: Delamination was observed when the forward to reverse current ratio was changed from 1.52 to 1.463. (a) provides an SEM image of the rotor and (b) shows a zoomed in image of the buckling that occurred due to stress.

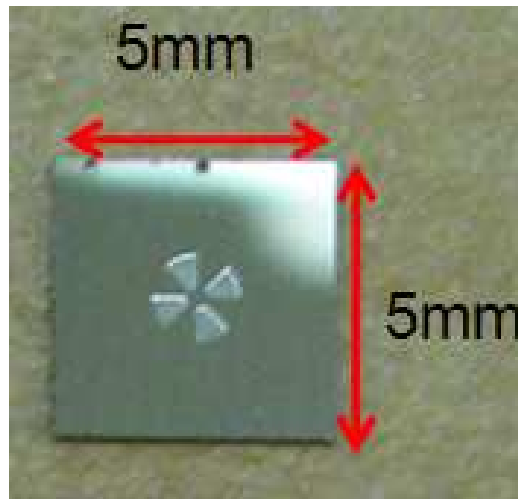


Figure 4.7: Fabricated and Diced Rotor Ready for Testing.

low the use of four electrodes and would spread the current more evenly than the rectangular samples allowed.

Once the rotors were deposited, the AZ P4620 was removed using AZ 400K developer and acetone. The full process follower for the successful plating of nickel can be found in Appendix C. The slide samples were then sent to AFRL/RV for dicing into separate  $5000 \mu m \times 5000 \mu m$  chips. Figure 4.7 is an image of one rotor after fabrication and dicing.

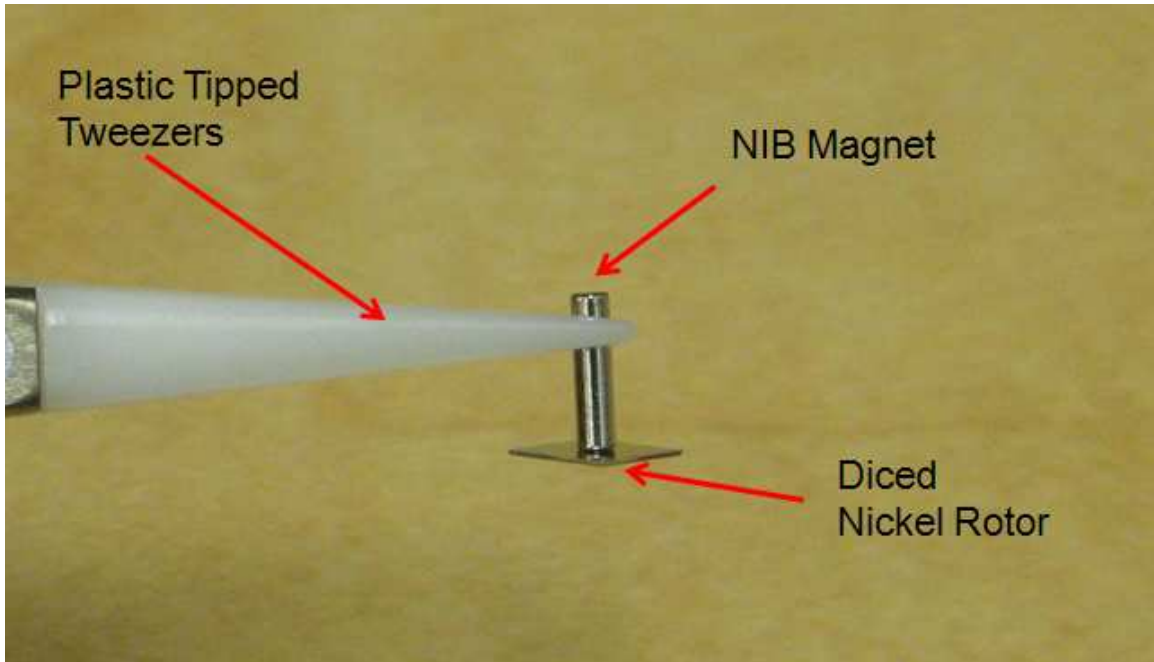


Figure 4.8: Diced Rotor Lifted From Table with NIB Magnet.

*4.2.3 Magnetization.* Magnetization was accomplished using a LakeShore Hall Measurement System. A flux density of 3000 Gauss was applied for 2 minutes at room temperature. In addition, some rotors were heated to a temperature of  $350^{\circ}C$  on a hot plate and then placed on top of a Neodymium Iron Boron (NIB) permanent magnet that had a residual flux density of approximately 3000 Gauss as well. Figure 4.8 provides an image of the nickel as it was magnetized with a NIB magnet. Obviously sufficient nickel was plated and polarized so as to create enough force to lift the sample from the table. The residual magnetization of the rotors will be discussed in the next chapter.

### ***4.3 Coil Fabrication***

The fabrication of the coil is more complex than that of the rotors, however, very little additional characterization was required due to the fact that the equipment utilized is frequently used at AFIT and AFRL/RV. In order to quantify how coil resistance affects the power output, multiple coil thicknesses were fabricated:  $0.5\ \mu m$ ,  $0.75\ \mu m$  and  $1\ \mu m$ . The coil fabrication process followed these steps:

1. Apply and pattern PR for runner trough etch and gold deposit.
2. Reactive ion etch (RIE) a trough to the same depth as the thickness of the runner.
3. Evaporate gold to desired thickness and clean off PR and excess gold, leaving behind patterned runner flush with the surface of the substrate.
4. Deposit dielectric using a Plasma Enhanced Chemical Vapor Deposition (PECVD).
5. Apply and pattern PR for excess dielectric removal.
6. RIE the excess dielectric.
7. Apply and pattern PR for final coil deposit.
8. Evaporate gold to desired thickness and clean off excess gold, leaving behind patterned coil.

*4.3.1 Runner.* It was intended for the top of the runner deposit to be flush with the surface of the substrate so as to avoid the sidewall thinning issue discussed in the previous chapter. RIE is a method of providing very accurate anisotropic etches and was used to etch a trough in the silicon substrate for the runner deposit. Given that the trough and the gold deposit for the runner require the same mask, only one PR application was used for both process steps. Shipley 1818 was used as the PR and was spun on at a thickness of  $1.8\ \mu\text{m}$ . The PR was patterned using the runner mask and sent to AFRL/RV for RIE. Each sample was etched to the depth of the intended thickness of the deposit. Gold was then evaporated onto the samples to the desired thickness, 0.5, 0.75 or  $1\ \mu\text{m}$  using a  $200\ \text{\AA}$  seed layer of Ti. The PR and excess gold was then removed in a sonic acetone bath. Figure 4.9 graphically illustrates the fabrication process and Figure 4.10 provides an image of the runner following the gold deposition.

The resulting profile was inspected using AFIT's Zygo Interferometer. The gold deposit was only slightly thicker than the depth of the trough resulting in a ridge of approximately  $0.01\ \mu\text{m}$  above the surface of the wafer for the  $0.5\ \mu\text{m}$  gold deposit.

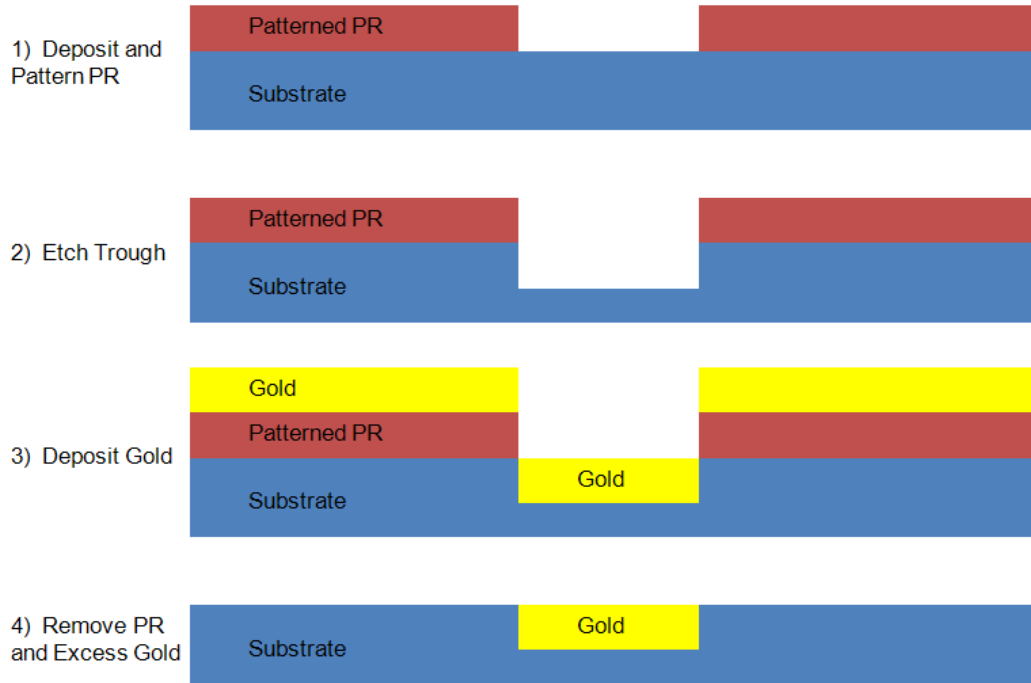


Figure 4.9: Illustration of the process for creating the coil runners.

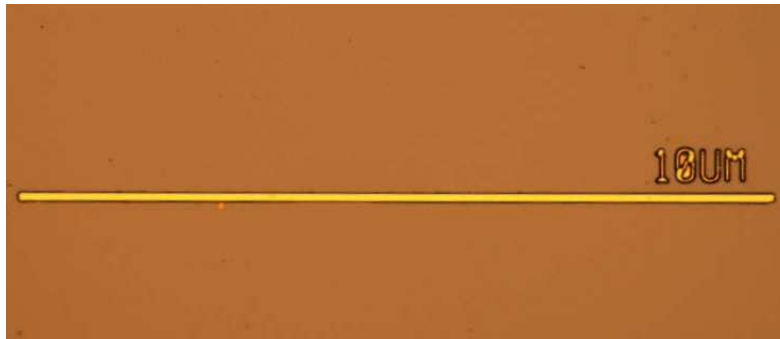


Figure 4.10: Image of the runner for the concentric coil. The line width is  $10\ \mu\text{m}$ .

The  $0.75$  and  $1\ \mu\text{m}$  deposits produced ridges in the range of a few tenths of a  $\mu\text{m}$ , however these larger ridges appear to be only on the edges of the runners, whereas the center is recessed completely into the substrate. Figure 4.11 provides an SEM image of the runner with nitride deposited to illustrate this anomaly. Most likely these sidewalls were a result of using only PR and not Lift Off Resist (LOR) for the lithography of the runner. LOR provides a method for clean depositions with no sidewalls, as shown in Figure 4.12. Although not used in this effort, the combined application of LOR and PR is recommended for future runner depositions.

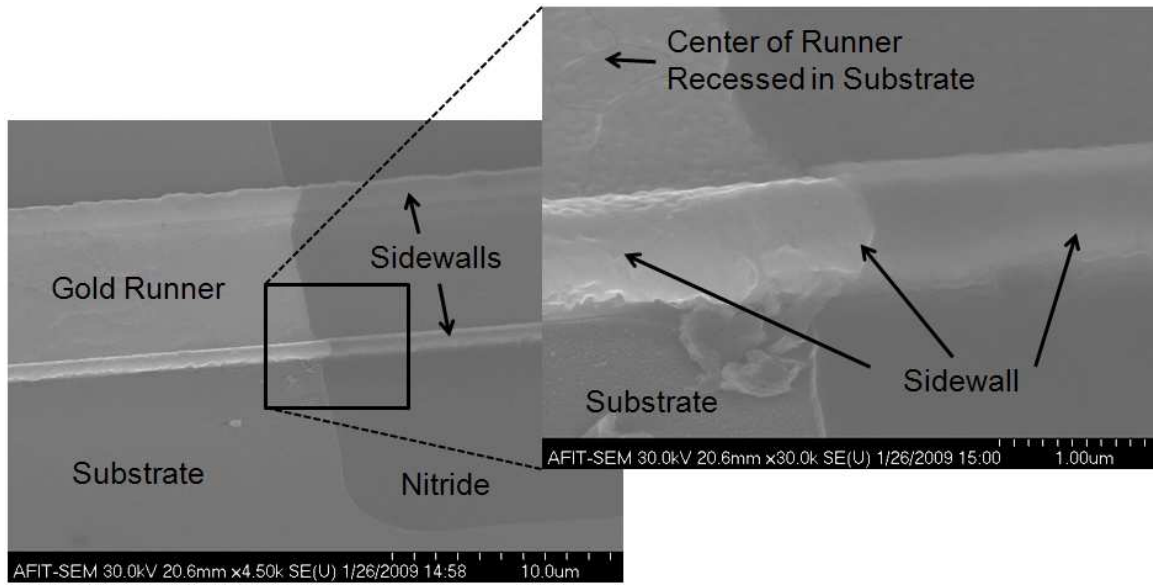


Figure 4.11: SEM image depicting the sidewalls found on the edges of the runner. The dielectric nitride is visible as well and provides a good reference to see the sidewalls. The image on the right provides a zoomed-in image of the sidewall anomaly.

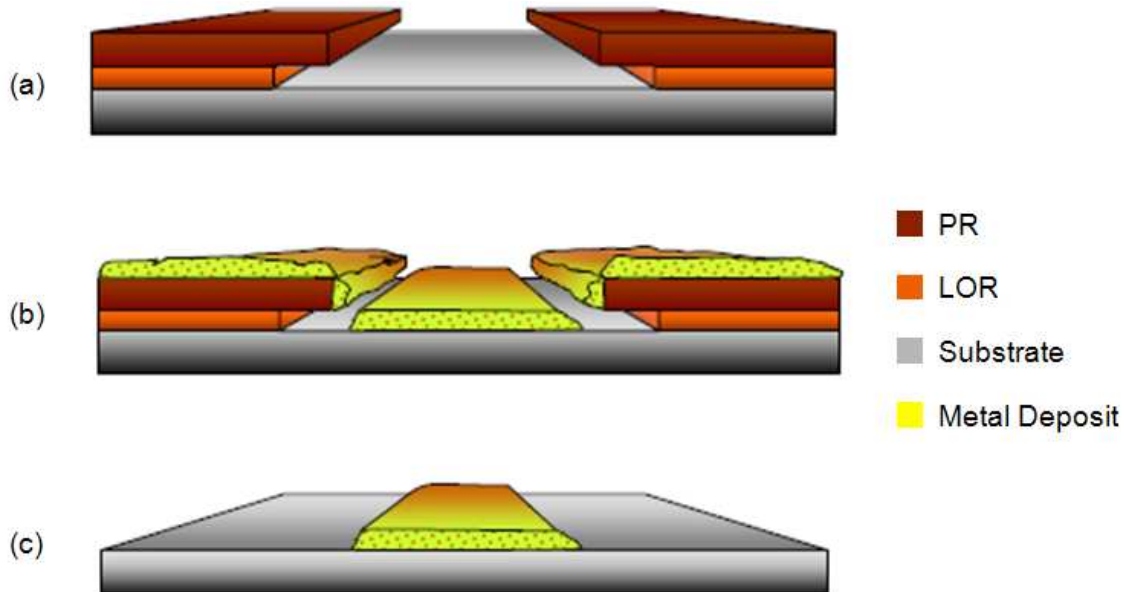


Figure 4.12: LOR is used to prevent residual sidewalls when depositing metals. (a) After LOR and PR are applied and exposed, the LOR developer will remove the PR normally but will overdevelop the LOR and produce an underetch beneath the PR. (b) When metal is deposited, sidewalls are not created because of the underetch. (c) When the PR and LOR are cleaned off, all excess gold is removed as well, leaving behind a clean deposit [28].

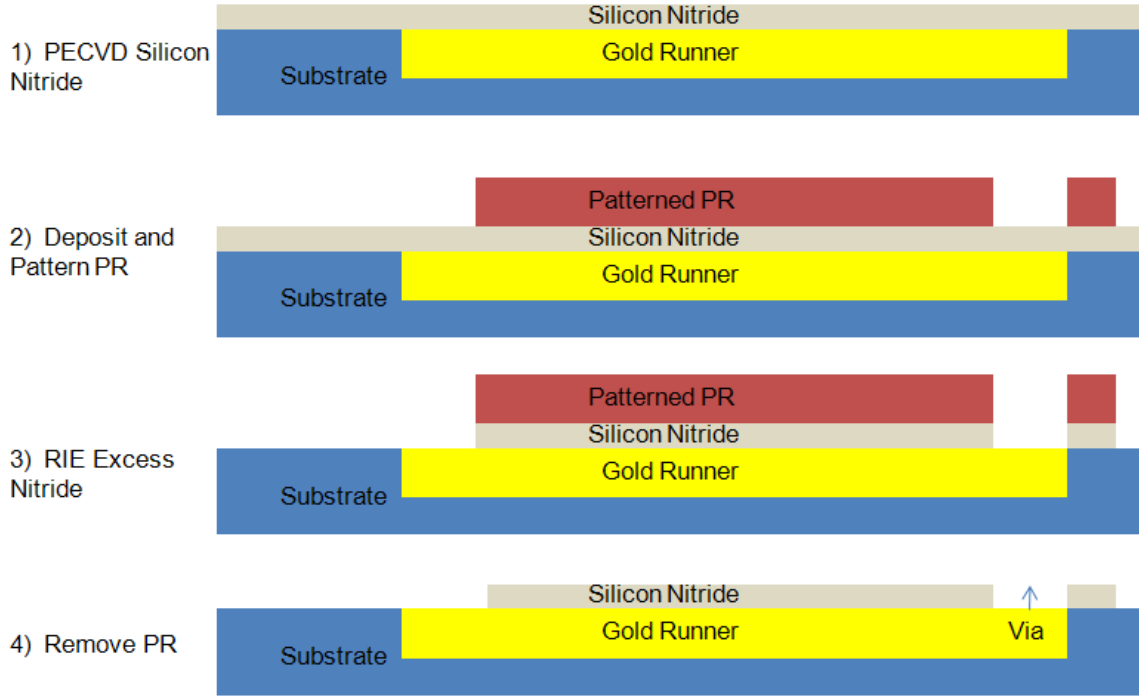


Figure 4.13: Illustration of the process for depositing and patterning the silicon nitride dielectric.

*4.3.2 Dielectric.* The next step was to pattern a dielectric over the runner to allow for a single small current path between the runner and the coil but inhibit shorting at other areas where the coil will cross the runner. A 1000 Å thick layer of silicon nitride was deposited using PECVD over the entirety of the samples. Shipley 1818 PR was then spun on to a thickness of 1.8  $\mu\text{m}$  and patterned with the dielectric lithography mask. An RIE was performed to remove the nitride from everywhere the patterned PR was not. Once the excess nitride was removed, the PR was cleaned off with acetone. Figure 4.13 graphically illustrates the fabrication process used for patterning the dielectric and Figure 4.14 provides an image of the patterned nitride deposit.

*4.3.3 Coil.* The final coil deposit made use of the LOR discussed in the previous section in order to overcome any additional sidewall issues. MicroChem LOR3A spreads to a thickness of approximately 0.4  $\mu\text{m}$ , therefore in order to deposit 1  $\mu\text{m}$  of gold, at least three layers of LOR3A are required. For all of the coils, three

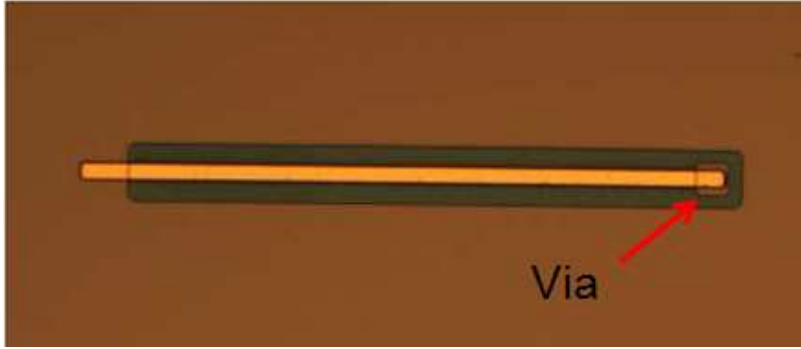


Figure 4.14: Nitride dielectric (greenish is color) after patterning. Note that the majority of the runner where the coil will cross is covered with the nitride and only a small square is open for the via.

layers of LOR3A were spread on and then topped off with one layer of Shipley 1818 PR. This provided approximately  $1.2\ \mu\text{m}$  of LOR and  $1.8\ \mu\text{m}$  of 1818. The coils were patterned and developed and the appropriate amount of gold was deposited for each sample. The excess gold, PR and LOR were removed with tape liftoff and a sonic acetone bath. Upon completing the coils, they were sent to AFRL/RV for dicing into separate  $5000\ \mu\text{m} \times 5000\ \mu\text{m}$  chips. Figure 4.15 provides an image of one of the final

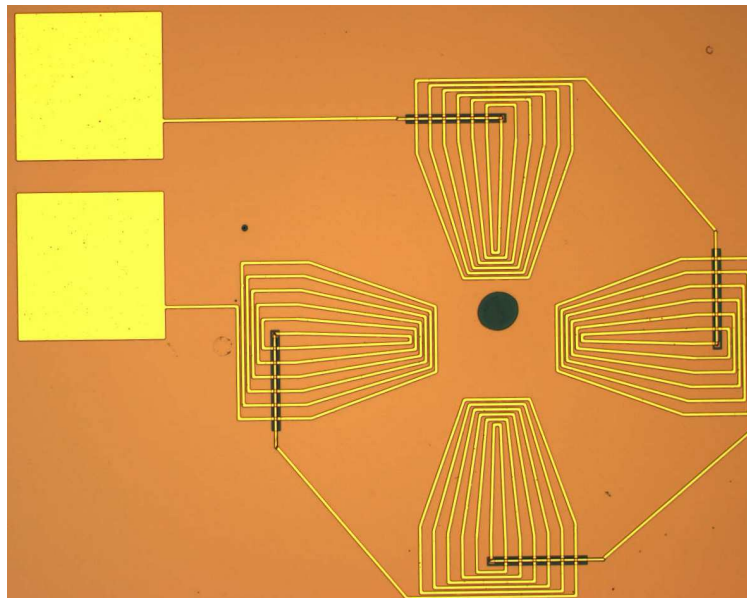


Figure 4.15: Completed 6-Turn Arrayed Coil with line widths of approximately  $10\ \mu\text{m}$ . The dot in the middle of the coils is residual nitride that was not removed, but has no effect on the performance of the coil.

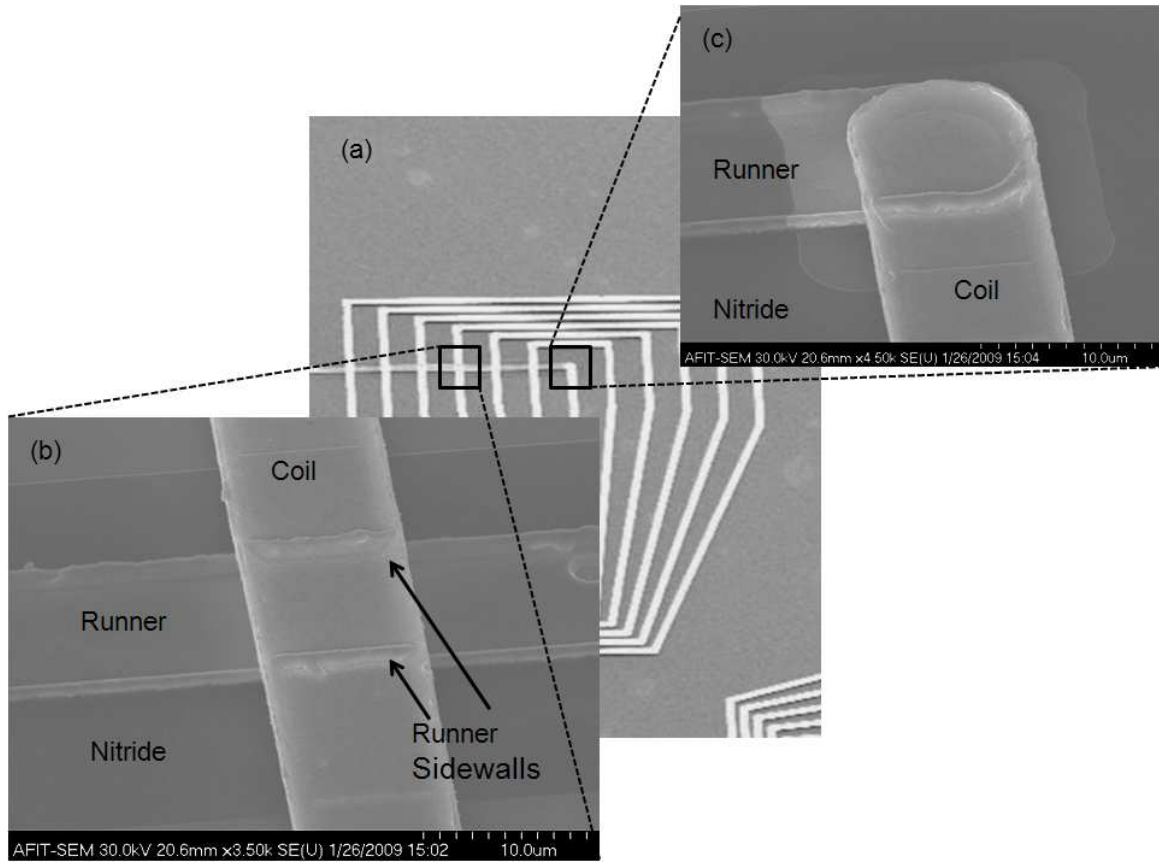


Figure 4.16: SEM images of one of the 6-Turn Coils. (a) provides reference for (b) and (c). (b) shows that the runner sidewalls did not cause the overlapping coil to have any observable sidewall thinning. (c) illustrates how the coil and runner connect at the via inside a nitride hole.

coils.

SEM images provide better detail of the resulting coil. Figure 4.16 provides close up images of the coil and runner interfaces, both at the via and where the coil ran over the runner but was separated with silicon nitride. It is also apparent from this image that the use of the recessed runner did not cause any sidewall thinning of the coil, even with the residual sidewalls of the runner.

#### 4.4 Test Structure Assembly

The test structure was built around an Eagle 860 flip-chip bonder, a LEGO™ Mindstorms NXT servo motor, and micro stages. The Eagle 860 aligns two samples through

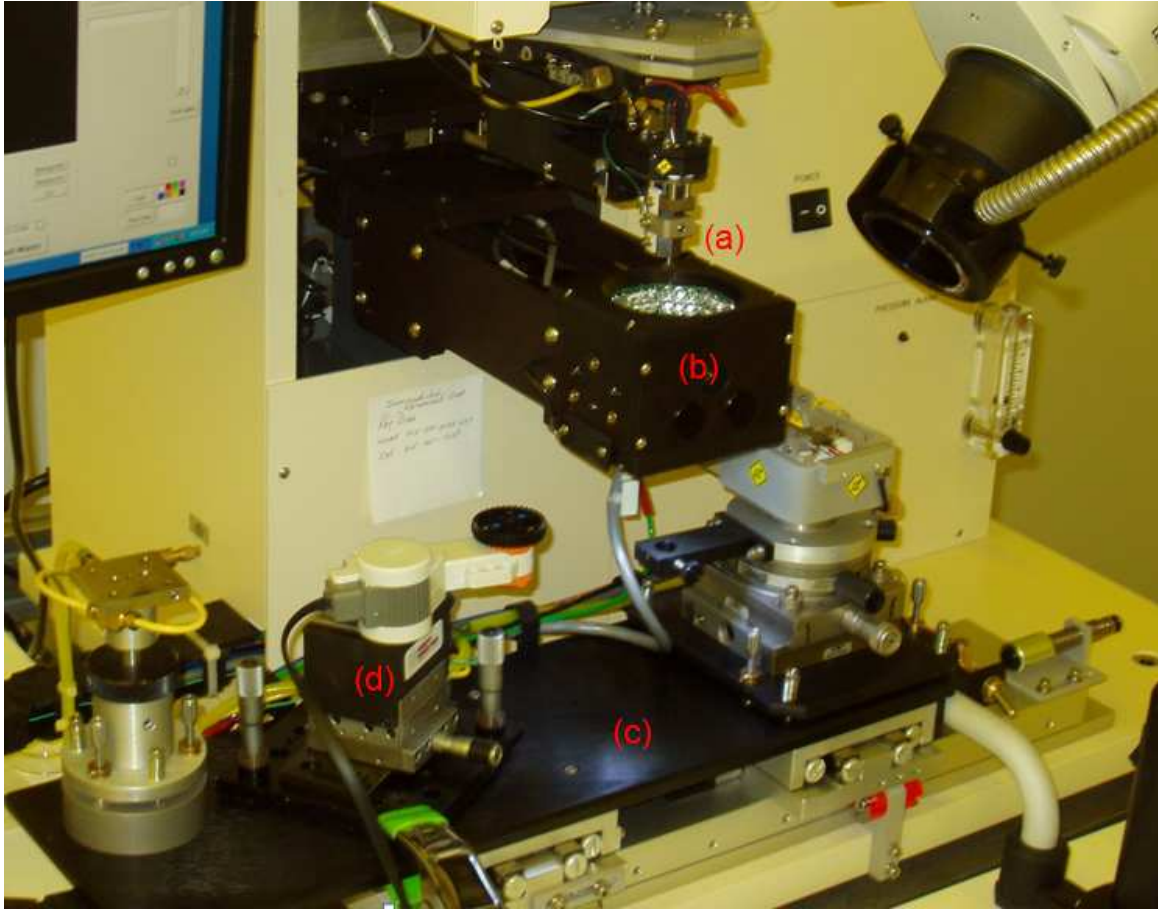


Figure 4.17: The Eagle 860 bonder was used to provide precise alignment of the coil and rotor. (a) marks the vertically adjustable head mount that will hold the inverted coil. (b) is an optical arm that provides imagery of both the head mount chip and the chip on the lower stage and allows for precise alignment of the two. It is retracted once alignment is achieved. (c) is the XY-adjustable stage where the custom rotary stage (d) sits.

the use of a vertically adjustable head mount, a lower XY-adjustable platform, and an optical arm. The optical arm provides the ability to overlay an image of the inverted head mount device with an image of the lower device to ensure that alignment is achieved. Once aligned the optical arm is retracted and the head mount is lowered to the desired position above the rotating sample. These components are identified in Figure 4.17.

In order to use the Eagle 860 for the micro-generator testing, the coil will be attached to the head mount and the magnetic rotors will be on a custom rotating

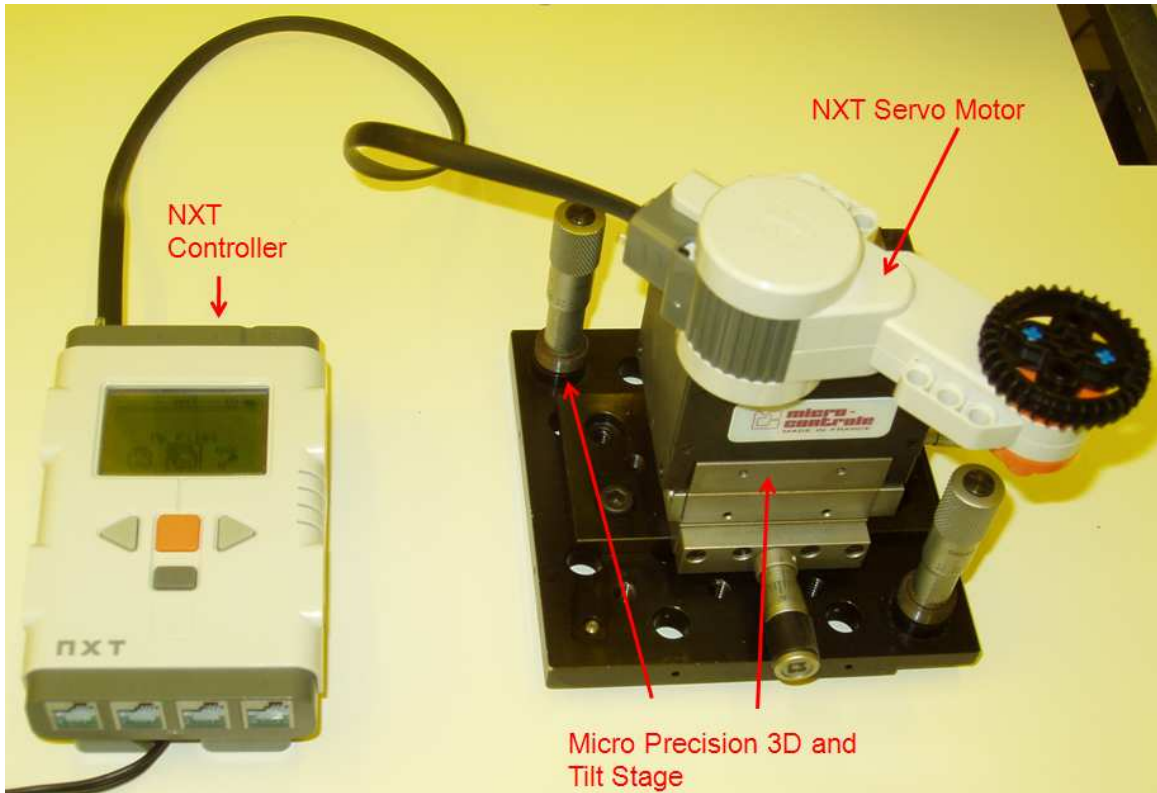


Figure 4.18: This custom stage was designed and built for testing the micro-generator. The Lego™ Mindstorms NXT servo motor and controller provide the rotation while the microstages assist in alignment.

stage on the bonder's lower platform. The custom stage was assembled using the servo motor, an XYZ microstage and a tilt adjustable stage. Figure 4.18 provides a picture of the assembled stage. A program was written that provided a rotation rate of 40 rpm, the rate that Sprecher predicted would be induced by blood-flow [5], for the servo motor using the LEGO™ Mindstorms NXT software and controller.

To determine the power output of the generator, an Agilent Multimeter will be used to measure a voltage drop in the configuration discussed in Chapter III. To facilitate measurements, the coil was placed into a MEMs package, like the one pictured in Figure 4.19. The coil chip was mounted in the recess of the package using double-sided tape and wire bonded at AFRL/RV. It was important that the bonding wires be tight to the surface of the coil chip so as to not interfere with rotation when the coil was brought in close to the rotating magnets. Figure 4.20 provides an SEM

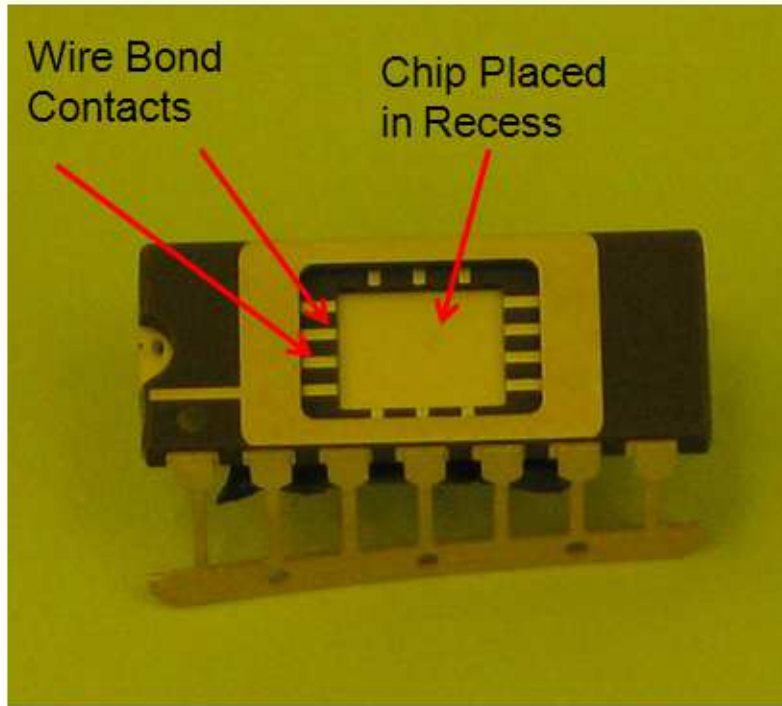


Figure 4.19: This package will be used for testing the coils. The coil chip will be placed in the recess in the middle and wire bonded to the contacts marked. This facilitates measurements by allowing the multimeter leads to be attached to the larger pins of the package.

image of the chip after being bonded to the package and illustrates how tight the wires were to the surface of the chip. The bonding was so tight that some bonding wires actually created an electric short across the gold lines that were used to assist in the dicing process of the individual samples. However, the packaged chip shown in Figure 4.20 did not short as is the case for a number of other packaged samples and will be used in testing.

#### ***4.5 Chapter Summary***

As discussed in this chapter, much of the fabrication effort was dedicated to the characterization of some of the processes required, such as the AZ P4620 PR and the nickel electroplating bath. In the end, the devices were fabricated as intended and the envisioned generator and test structure were prepared for the next step, testing.

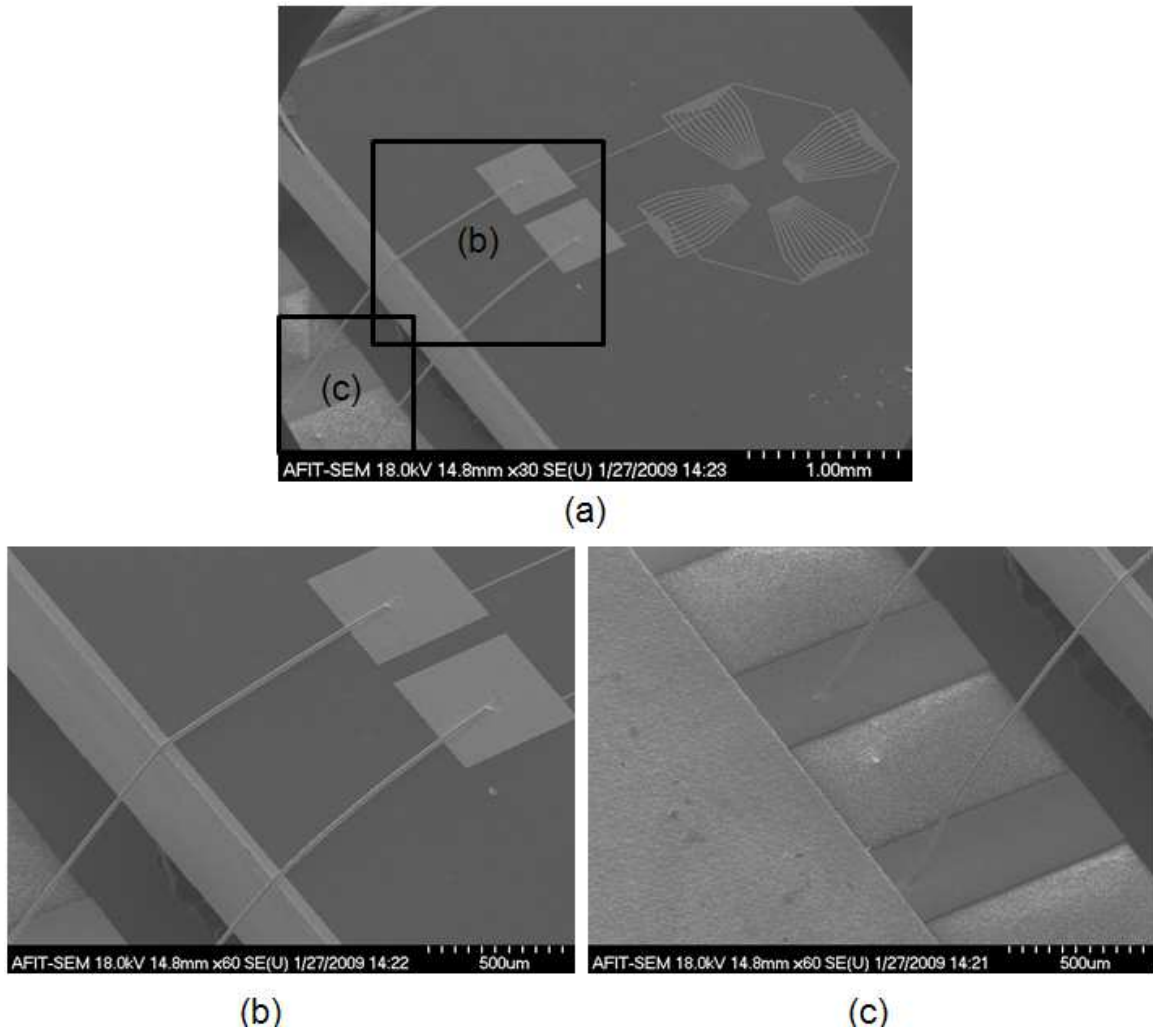


Figure 4.20: SEM images of coil chip bonded to package. (a) provides an image of the chip in the MEMS packaging and provides reference for (b) and (c). (b) shows that the wires were bonded extremely tight to the surface of the chip ensuring that the wires do not make contact with the rotor when they are placed in close proximity. (c) illustrates how the wires were bonded to package. It is noted that some wires were bonded so tight that they actually shorted with the gold dicing line around the perimeter of the sample. This sample, although it appears to have shorted, did not. This was verified by measuring the resistance of the packaged coil and comparing it to the resistance of the coil prior to packaging.

## V. Testing and Results

After fully fabricating the coil, magnets and testing apparatus the micro-electromagnetic generator was ready for testing. This chapter will discuss the results of the fabrication of each portion of the generator as well as the testing apparatus. The resulting power output of the device as a whole will also be measured and presented. Appendix D contains the raw data collected from measurements and testing.

### 5.1 *Rotor Magnets*

Three rotor magnet slides were plated with nickel and diced. Two of the slides, samples SH-M4 and SH-M5, were plated to thicknesses ranging from 12 to 18  $\mu m$  and one slide, sample SH-M3, was plated to thicknesses in the range of 8 to 14  $\mu m$ . (The variation in thickness was due to the variation in current density across the sample as discussed in the previous chapter.) SH-M5 experienced severe delamination and was not used for further testing. SH-M4 showed peeling on some of the rotors but not all. SH-M3 was the sample that experienced no peeling at all and one of the rotors is imaged in Figure 4.5. All thickness measurements of the rotors were taken by a Tencor Profilometer and are detailed in Appendix D.

After being magnetized as discussed in the last chapter, the residual magnetization was measured using the Gauss meter that is connected to the Hall Measurement System. The flux density of both the magnets polarized by the Hall magnet and those polarized with the hot plate and NIB magnets was almost unmeasurable with the gauss meter. For example, the flux density of ambient air was in the range of 0.1 Gauss and, when the magnets were placed in close proximity of the Gauss meter, a variation of approximately 0.1 Gauss was observed. Given that this fluctuation is well within the domain of error of the Gauss meter, accurate measurements were not acquired.

It was not initially understood why the rotors did not retain an appreciable magnetic field. As shown in Figure 4.8, the nickel rotors can be significantly polarized.

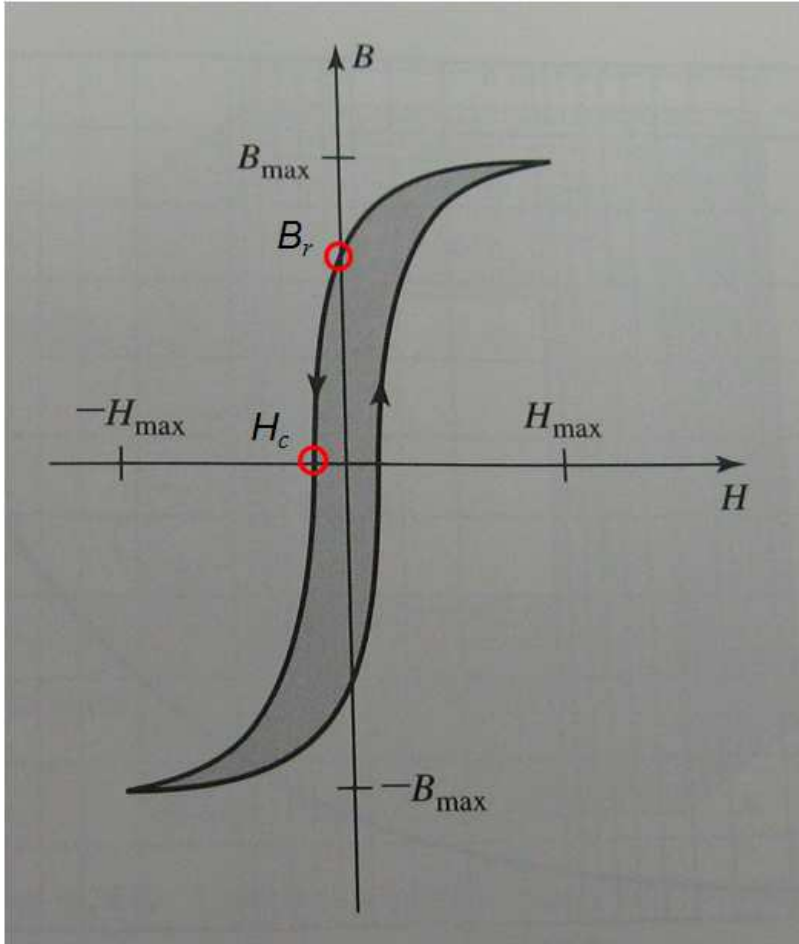


Figure 5.1: Example of  $B$ - $H$  Curve [29].

Further research and guidance provided an answer as to why the residual magnetic field was lost so quickly.

Magnetic materials are typically characterized by curves known as a hysteresis loop or  $B$ - $H$  curve, like the one shown in Figure 5.1. The point where the curve crosses the  $B$  axis, annotated as  $B_r$ , is referred to as the residual flux density or remanent magnetization of the material. This is the value of the flux density that will remain after being magnetized to saturation, should no additional energy be added to the system. The point that the loop crosses the  $H$  axis, annotated as  $H_c$ , is the coercivity of the material. Coercivity is defined as the amount of force required to reduce the flux density back to zero after being magnetized to saturation. Materials that have a high coercivity are known as “hard magnets” whereas a low coercivity

material is referred to as a “soft magnet”. In addition, coercivity is typically higher for materials that have defects in their atomic structures. Although, the defects also cause a reduction in the flux density [18, 29, 30].

These two values, coercivity and remanent flux density, are extremely important for the magnetic material in a electromagnetic generator. Obviously, a high remanent flux density is desired to induce maximum current in the conducting coil, but a high coercivity is desired as well so that ambient energy and forces, such as small bumps and temperature changes, do not demagnetize the magnet. Permanent magnets are permanent due to their extremely high coercivity values.

The coercivity of the electroplated nickel rotors was measured with a Vibrating Sample Magnetometer (VSM) at the Air Force Research Laboratory/Propulsion Directorate (AFRL/RZ). Figure 5.2 contains the resulting  $B-H$  curve with the coercivity circled. The coercivity was measured to be approximately 90 Oersteds. The low end of permanent magnets have a coercivity of 2,000 to 3,000 Oersteds [30]. It

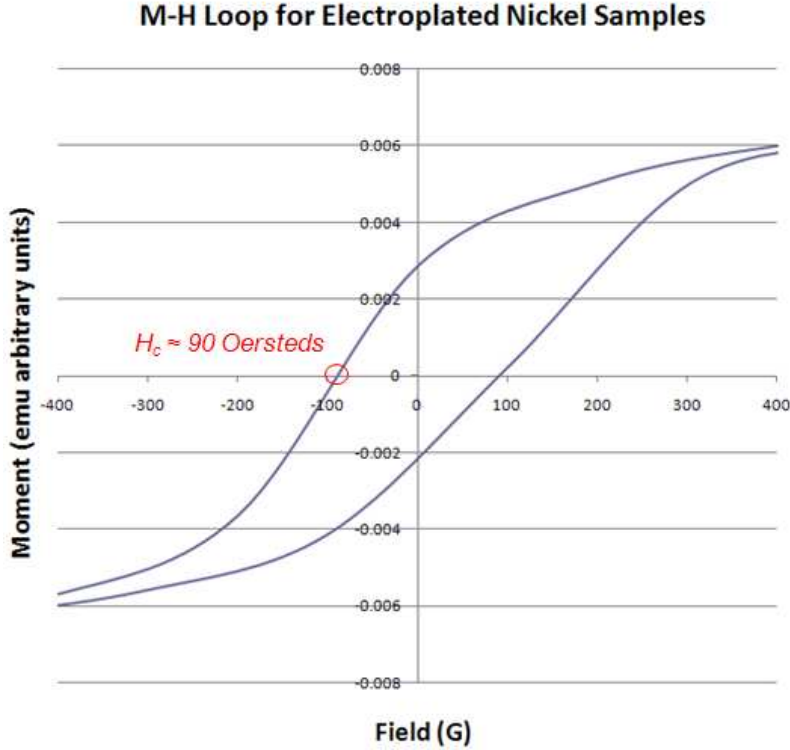


Figure 5.2:  $B-H$  curve for electroplated nickel rotors measured with a VSM.

turns out that all nickel, no matter how it is deposited, produces very soft magnets, as does annealed iron. Even though these materials are capable of acquiring a powerful remanent flux density, they cannot maintain that density as they experience external forces. This is the reason that the nickel magnets exhibited high magnetic flux characteristics when placed near the NIB magnets but the flux was imperceptible when measurement was attempted. The movement of the samples with the tweezers was evidently sufficient energy to randomize the poles that had just been polarized.

## 5.2 *Stator Coils*

The goal in fabricating the coils was to create a low resistance electrical path that would be mutually orthogonal to the  $B$  field and varying flux density. In total, six slides of coils completed the fabrication process: two slides of each of the desired thicknesses, 0.5, 0.75, and 1  $\mu m$ . The first step for determining how well the coils were fabricated was to measure the resistance of the coils. Resistances were taken using an Agilent multimeter connected to the two pads on each coil. The results of those measurements can be found in Table D.2.

As discussed in the design portion of this thesis, the line widths of all of the coils was intended to be 10  $\mu m$ . However, when fabricating at this scale, variations are typical. For this reason and to determine how well calculated resistance values match to experimental results, a Tencor Profilometer at AFRL/RV was used to attempt to measure the average final line widths and thicknesses of each type of coil on each slide sample. With that data, the resistances were calculated and compared with the average of the reasonable measured values in Table 5.1.

As can be observed in Table 5.1 and Table D.2, the majority of the 0.5  $\mu m$  coils and a few of the 0.75 and 1  $\mu m$  coils exhibited extremely high resistance values. A conclusive reason for such a high resistance was not found. One potential reason is that some residual PR was present prior to the final gold coil deposit. This would result in a barrier of PR between the coil and runner and would increase the resistance. The discrepancies in the other predicted and experimental results were attributed to

Table 5.1: Calculation of resistance of coil based on measured dimensions using Microsoft Excel. Length was calculated using L-Edit. The average of the measured resistances is provided for comparison.

		Coil Measured	Thickness ( $\mu\text{m}$ )	Width ( $\mu\text{m}$ )	Total Length ( $\mu\text{m}$ )	Calculated Resistance from Measured Dimensions ( $\Omega$ )	Average of Measured Resistances* ( $\Omega$ )
			$A = W \times T$			$R = \frac{\rho L}{A}$	
$0.5\ \mu\text{m}$	C6	Coil #1	0.52	15.06	47867.43	136.47	3000.00
		12-Turn #3	0.51	18.26	113469.34	272.22	239.70
		6-Turn #3	0.45	15.24	43553.43	139.60	1230.00
	C9	Coil #1	0.50	15.00	47867.43	141.30	44000.00
		12-Turn #1	0.60	15.00	113469.34	279.13	209.00
$0.75\ \mu\text{m}$	C5	Coil #1	0.77	13.96	47867.43	99.24	113.40
		12-Turn #4	0.75	14.63	113469.34	229.81	50.60
		6-Turn #3	0.67	13.92	43553.43	104.11	47.19
	C8	Coil #1	0.75	13.27	47867.43	105.96	203.31
		12-Turn #4	0.77	15.46	113469.34	212.33	120.45
		6-Turn #2	0.76	14.22	43553.43	88.72	46.47
$1\ \mu\text{m}$	C10	Coil #1	0.97	10.66	47867.43	102.50	51.92
		Coil #4	0.99	14.45	47867.43	74.18	51.92
		6-Turn #3	1.05	13.55	43553.43	67.97	75.30
	C7	Coil #1	1.06	14.41	47867.43	69.19	97.68
		12-Turn #4	1.05	13.59	113469.34	176.22	39.33
		6-Turn #6	1.04	13.39	43553.43	69.58	33.24

\* Resistances that were excessively high were ignored for averaging of 0.75 and 1  $\mu\text{m}$  samples

small variations in the width and height of the coil and runner. In addition, the resistivity value,  $\rho$ , that was used in the calculations was a bulk gold measurement. A thin film resistivity measurement of the evaporated gold used in fabrication was not performed, but would most likely differ somewhat from that of the bulk resistivity value and could account for some of the variations in the resistance measurement data as well.

### 5.3 Testing Apparatus

The test structure performed as intended. Double sided tape was used to mount the coil and package to the head mount of the Eagle 860 because the built-in vacuum

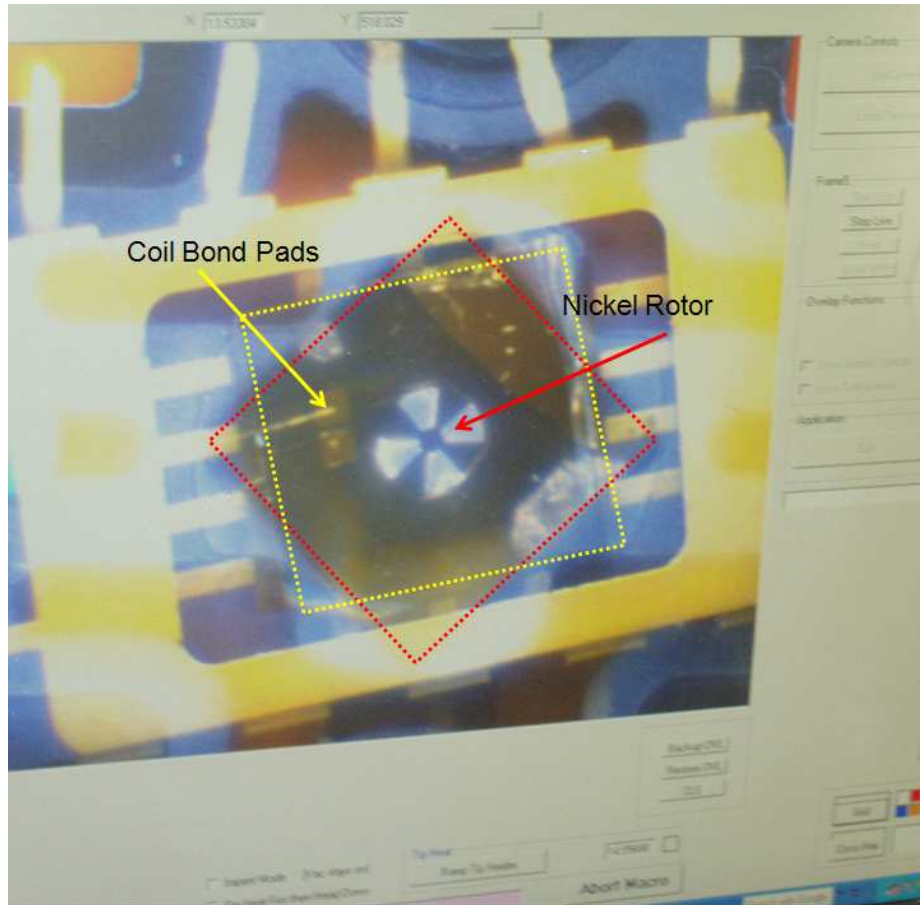


Figure 5.3: The Eagle 860 provides live partially transparent camera feeds to assist in the alignment of the upper and lower samples. This image shows the overlay of the rotor chip (outlined in red) and the coil chip (outlined in yellow) as they were aligned.

was not strong enough to support the package, coil chip and multimeter leads. The Eagle 860 provided very good imaging to ensure that the coil and the rotors were aligned well. Figure 5.3 provides a picture of the interface used to align the coil and rotor.

Once aligned, the head mount was moved down to a position within a few millimeters of the rotor. Figure 5.4 provides an image of the testing apparatus in this position. The original intent was to bring the head mount into contact with the rotor and then retract the head mount a defined amount, approximately  $100\text{ }\mu\text{m}$ , for testing. (The head mount position can be measured at  $0.05\text{ }\mu\text{m}$  precision.) However,

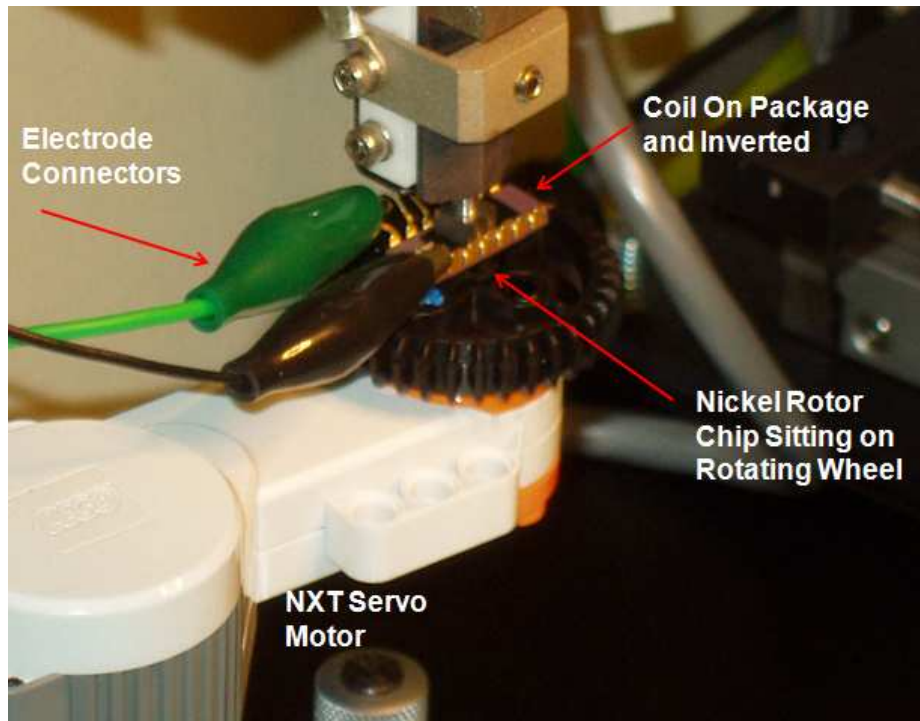


Figure 5.4: Image of the coil package and rotor in position for testing using the Eagle 860.

the servo motor produced a very slight wobble in the rotating wheel and rotor chip when it was activated. These small variations would most likely cause collisions at such a close proximity. In addition, with the coil chip mounted as it is and with the wobble, such contact would more than likely break the bonds that are connecting the chip to the package. Therefore, it was decided not to bring the coil into full contact for precise distance measurements. Instead, the distance between the coil and rotor was visually observed and the head mount was stopped when the sample was within 1 to 2 *mm* in order to protect the head mount of the Eagle 860. This, of course, reduces the strength of the magnetic field experienced by the coil, but it was decided that for feasibility testing this was acceptable. With the coil and rotor in this position, the leads from the multimeter were attached to the pins on the package.

## 5.4 *Micro-Generator*

A  $10\text{ K}\Omega$  resistor was used as the load to measure the power output of the generator. The Agilent Multimeter has an AC voltage precision of  $0.001\text{ mV}$ . Using this setting, no voltage drop was observed for any of the coils or magnets. Given that the magnets were not retaining their flux density due to the “softness” of the nickel, this was not surprising.

However, in order to verify that no current was being produced, a Keithley PicoAmmeter was used to measure the current output of the device. The picoammeter has a current measurement resolution of  $2\text{ nA}$ . The resistor was removed from the circuit and the leads were attached to each electrode for current measurements. No current was measured in this configuration either.

## 5.5 *Chapter Summary*

This chapter presented the results of measuring and testing the rotor and coil of the micro-generator as well as the generator as a whole. In addition, a discussion of the functionality and process of using the testing apparatus was included. With the failure of the nickel magnets, the micro-generator was unable to produce a measurable current or voltage.

## VI. Conclusions

This chapter will begin by providing a summary of the scientific contributions made during this effort. In addition, recommendations for future work based upon the lessons learned during this research will be presented.

### 6.1 *Scientific Contributions*

First and foremost, this thesis has shown that the use of electroplated nickel as a magnetic rotor for a micro-electromagnetic generator is not feasible. However, the new designs of the rotors and coils presented in this thesis provide a solid basis for future efforts in developing a micro-electromagnetic generator. The angular coil and toroidal rotor design meet the electromagnetic orientation requirements to properly induce current flow for a generator. Simply switching the material being deposited for the rotors would lead to the fabrication of a working generator.

The trough and runner deposition process is also a very important finding of this thesis. It was shown that one could successfully overlay evaporated wires without concern of thinning sidewalls. While it is true that the thinning sidewalls could be avoided by sputtering the metal deposit instead of using evaporation, sputtering is not always desired for some applications. Therefore, this finding allows the use of the optimal deposition method for the application when wires must be overlaid.

### 6.2 *Lessons Learned and Recommendations*

In an effort to facilitate future research in this field, some recommendations for follow-on research are provided here. These recommendations are derived from the difficulties experienced in this research and from ideas that were not tested due to time constraints.

*6.2.1 Sample Selection.* Due to the rectangular shape of the samples used for this effort, it was very difficult to achieve a consistent PR spread for patterning. This in turn lead to varying levels of PR thicknesses across the sample and thus varying

resolution after exposure and development. These issues could be easily addressed by using a circular sample instead of the rectangular samples. Not only would this save time in characterizing PRs for custom thicknesses, but using the circular samples would also lead to crisper deposits and etches. In addition, electroplating electrodes used at AFRL/RZ are intended for circular 2-inch wafers, thus more uniform current densities, and plating thicknesses, would most likely be observed as well.

*6.2.2 LOR for Runner Deposit.* As discussed in Chapter IV, the sidewalls that were observed on the edges of the runner could most likely be avoided with the use of LOR. However, this might also lead to troughs that are wider than the runner deposit because of the underetch associated with the LOR. The RIE will most likely etch to the edge of the LOR, whereas the gold deposit will only be to the edge of the overarching PR. (Refer to Figure 4.12.) Experimentation could easily identify if this is the case.

*6.2.3 Use of a High Precision Rotary Stage.* The wobble that was observed using the LEGO<sup>TM</sup> servo motor limited how close the coil and rotor were placed relative to one another, which in turn reduced the magnetic field strength experienced within the coil. The acquisition of a high precision rotary stage would eliminate this limitation and would allow for these devices to be much closer in proximity.

*6.2.4 Electromagnetic Modeling Tools.* Modeling of the micro-generator was not accomplished with this thesis work because a tool for such modeling was not available at AFIT. However, recently it was discovered that AFRL/RZ does possess tools that could process such models. Any follow-on research should start with these modeling tools. Various magnetic materials could be investigated and potential power output could be determined.

*6.2.5 Magnetic Material Selection.* Pure electroplated nickel is not a practical material to be used for electromagnet generators, as observed in this effort. A

sputtered nickel deposit might result in more defects and thus a higher coercivity. Optimally, though, a known permanent magnet material such as steel alloys or rare-earth magnets (neodymium and samarium-cobalt) would be used. In order to use one of these materials, a MEMS and IC compatible micro-deposition and patterning process would need to be identified [18]. Engineers at AFRL/RZ did say that materials such as NIB have been deposited via sputtering and pulse laser deposition (PLD) [30]. However, with sputtering and PLD, a method of etching the excess material is required as well. Obviously, more research is needed in this area.

*6.2.6 Turbine Integration, Packaging and Power Conditioning.* Once the micro-generator is shown to produce power during rotation, the remaining parts of the MFPG device would need to be fully designed, fabricated and tested. Additional areas of research include: the fabrication of a turbine and a process for attaching it to the rotor, fully fabricating a package to safely contain the generator while at the same time allowing blood flow to actuate the turbines, and a method for conditioning the power output of the generator for use with IC circuitry.

*6.2.7 Piezoelectric Research.* In Chapter 2, energy harvesting through the use of piezoelectric materials was briefly discussed. A piezoelectric solution for harvesting ambient energy seems to offer many advantages to that of using an electromagnetic generator. Firstly, piezoelectric harvesters require minimal movement for power generation, whereas an electromagnet generator generally requires significant mechanical motion in order to induce current flow. By reducing the amount of mechanical motion, one increases the lifespan of the device and reduces the complexities of design. In addition the power output potential of piezoelectrics are on par with those of electromagnetic generators [9, 12]. Lastly, piezoelectrics could potentially harvest the ambient kinetic energy of vibrations in almost any part of the body, eliminating the need to place the device in bloodflow as was the intention of the micro-electromagnetic generator. Additional research into the methods of depositing

piezoelectrics at the microscopic level could lead to exciting and very useful techniques of harvesting ambient energy of bio-implanted devices.

### ***6.3 Conclusion***

A working micro-generator, such as the one envisioned in this thesis, would lead to a new paradigm of power generation and a revolution in the possibilities of biomedical engineering. There is no doubt that research should be continued. If one could identify a method of depositing a rare-earth magnetic material in a MEMS compatible manner, the designs presented here would provide the remaining processes to create the active portion of a micro-generator.

## Appendix A. Supporting Calculations

This appendix contains calculations used in the analysis of engineering tradeoffs.

Resistance Added by Seed Layer				
Material	Length ( $\mu\text{m}$ )	Width ( $\mu\text{m}$ )	Thickness ( $\mu\text{m}$ )	Resistance ( $\Omega$ )
		$A = W \times T$		$R = \frac{\rho L}{A}$
Chromium	2.00E-02	10	10	0.0000250
Titanium	2.00E-02	10	10	0.0000840

Increasing # of Coil Turns increases Length which increases Resistance					
Material	Length ( $\mu\text{m}$ )	Width ( $\mu\text{m}$ )	Thickness ( $\mu\text{m}$ )	Resistance ( $\Omega$ )	# of Coil Turns
		$A = W \times T$		$R = \frac{\rho L}{A}$	
Gold	1182.423	10	1	3	1
Gold	2603.783	10	1	6	2
Gold	4239.299	10	1	9	3
Gold	6088.528	10	1	13	4
Gold	8149.803	10	1	18	5
Gold	10424.08	10	1	23	6
Gold	12910.24	10	1	29	7
Gold	15606.81	10	1	35	8
Gold	18513.18	10	1	41	9
Gold	21625.06	10	1	48	10
Gold	24942.98	10	1	55	11

Material	Resistivity $\rho$ ( $\Omega\text{-}\mu\text{m}$ )
Copper	1.68E-02
Gold	2.21E-02
Aluminum	2.65E-02
Tungsten	5.28E-02
Zinc	5.90E-02
Nickel	6.93E-02
Chromium	1.25E-01
Titanium	4.20E-01

Figure A.1: Resistance Calculations using Microsoft Excel<sup>TM</sup>. Lengths were found by using L-Edit's area calculator to find the area of each turn and dividing by the width of the lines, 10  $\mu\text{m}$ .

Area of Coils			
	Width ( $\mu\text{m}$ )	Length ( $\mu\text{m}$ )	Area ( $\mu\text{m}^2$ )
12-turn	2169	2169	4704561
6-turn	1768	1764	3118752
12-turn Coil requires 51% more surface area than the 6-turn Coil			

Figure A.2: Surface area calculations and comparisons using Microsoft Excel<sup>TM</sup>.

### Nickel Electroplating Parameter Calculations

#### Wafer Samples (Non-Patterned)

$W\_Fwd\_Cur := 0.8A$	$W\_Rev\_Cur := 0.525A$	Optimal Currents found for 3" Wafers
$W\_Area := \pi \cdot (1.5in)^2$	$W\_Area = 45.604\text{ cm}^2$	3" wafer Area
$Fwd\_Dens := \frac{W\_Fwd\_Cur}{W\_Area}$	$Fwd\_Dens = 17.542 \frac{mA}{cm^2}$	Optimal Forward Current Density
$Rev\_Dens := \frac{W\_Rev\_Cur}{W\_Area}$	$Rev\_Dens = 11.512 \frac{mA}{cm^2}$	Optimal Reverse Current Density

#### Small Patterned Samples

$Sample := (4.5 \cdot 1.5)\text{cm}^2$	$Sample = 6.75\text{ cm}^2$	Total Size of Samples used for Nickel Deposition
$PR\_Coverage := 643554211.774\mu\text{m}^2$	$PR\_Coverage = 6.436\text{ cm}^2$	Amount of Slide Covered in Photoresist (Calculated with L-Edit)
$Tot\_Coverage := PR\_Coverage - 0.5 \cdot 5000\mu\text{m} \cdot 5000\mu\text{m}$	$Tot\_Coverage = 6.311\text{ cm}^2$	Total Amt of slide covered in PR after contact points are cleaned off
$Exposed\_Seed := Sample - Tot\_Coverage$	$Exposed\_Seed = 0.439\text{ cm}^2$	Total Area of Exposed Seed
$New\_Fwd\_Cur := Exposed\_Seed \cdot Fwd\_Dens$	$New\_Fwd\_Cur = 0.0077\text{ A}$	Forward Current to be used for patterned samples
$New\_Rev\_Cur := Exposed\_Seed \cdot Rev\_Dens$	$New\_Rev\_Cur = 0.0051\text{ A}$	Reverse Current to be used for patterned samples

#### Fwd to Rev Ratio

$\frac{Fwd\_Dens}{Rev\_Dens} = 1.524$		Optimal Ratio of Fwd to Rev current found with non-patterned samples
$New\_Fwd\_Dens := \frac{0.08A}{Exposed\_Seed}$	$New\_Fwd\_Dens = 182.042 \frac{mA}{cm^2}$	New Fwd Current Density used to overcome inaccuracies of power supply
$New\_Rev\_Dens := \frac{0.053A}{Exposed\_Seed}$	$New\_Rev\_Dens = 120.603 \frac{mA}{cm^2}$	New Rev Current Density used to overcome inaccuracies of power supply

Figure A.3: Plating seed surface and current density calculations using MathCad™.

## Appendix B. Lithographic Mask Design

This appendix contains the MEMS Pro L-Edit designs used for fabrication of the micro-generator presented in this thesis. The mask was submitted to Photo Sciences, Inc. using their FastTrack service. The mask was fabricated using a soda-lime substrate with patterned chrome as the masking material. The title on the mask is Shields\_Coil\_Mask. The designs were created using one layer of the L-Edit framework, Poly-0 (orange in the images). The Poly-0 designates the dark portions of the mask. Areas without the Poly-0 designate the light areas. The mask is intended to be used with positive photo-resists, meaning that the light areas of the mask will be developed off.

The mask substrate is a 4" square, but the mask aligner that is used by AFIT, an EVG 620, only uses a 3" circle of that mask for patterning. Given that each of the devices to be fabricated required only  $5000 \times 5000 \mu m^2$ , multiple smaller masks were included on a single 4" mask. In total, 7 smaller masks with dimensions of  $45 \times 15 mm^2$  were included. Figure B.1 provides an image of the L-Edit design.

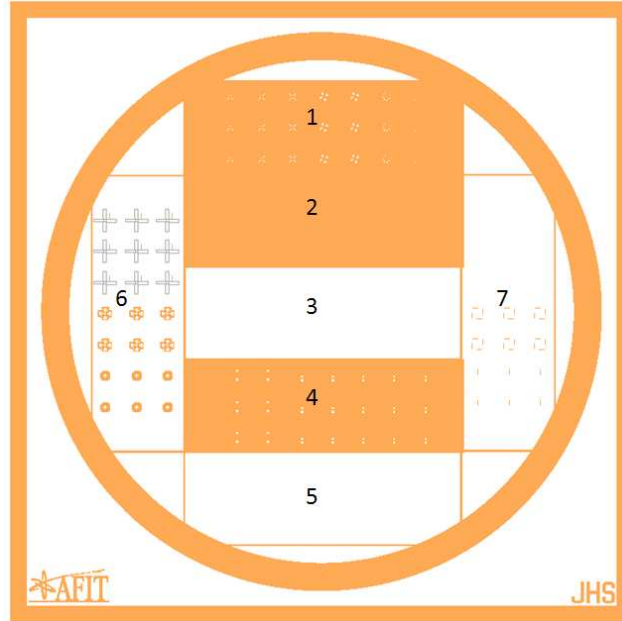


Figure B.1: Full L-Edit Mask. The patterning area of the mask, a 3" circle, was divided into 7 smaller slide masks as marked.

Table B.1: Functions of Micro-Generator Submasks

#	Slide Mask Function	Figure References
1	<b>Magnet Nickel Deposit</b> Pattern for depositing nickel for the rotor magnets.	B.3
2	<b>Coil Runner Etch and Deposit</b> Pattern for etching troughs for the coil runner and depositing gold into it.	B.4
3	<b>Coil Nitride Etch</b> Pattern for etching the silicon nitride from everywhere it is not needed and leaving a layer to separate the runner from the coil.	B.5, B.6
4	<b>Final Coil Deposit</b> Pattern for depositing the coil and pads for each stator coil.	B.7
5	<b>Magnet Nickel Plating Seed Etch</b> Pattern for etching the seed off of the rotor magnet slide should it be needed.	B.8
6	<b>Coil Plating Seed Etch</b> Pattern for etching the seed off of the stator coil slide should electroplating be used for depositing the coil metal.	B.9
7	<b>Runner Plating Seed Etch</b> Pattern for etching the seed off of the stator coil slide should electroplating be used for depositing the coil runner.	B.10

Each rectangular slide area consists of three rows and nine columns, resulting in twenty-seven  $5000 \times 5000 \mu m^2$  squares. The three squares on either end are for alignment purposes only, leaving the 7 columns in between, or 21 squares, for useful structure patterns. The alignment marks used are represented in Figure B.2. The 7 slides are of two varieties—rotor magnet and stator coil—and are intended for different processing steps of each respectively. The rotor magnet slides consist of three 80, 120 and  $160 \mu m$  rectangular arm rotors, six 4-arm toroidal rotors, and three 8 and 32-arm toroidal rotors. The stator coil slides consist of six single concentric circle coils, six 12-turn arrayed angular coils and nine 6-turn arrayed angular coils. The functions of each of the slides and their associated zoomed in figure references are listed in Table B.1.



Figure B.2: Submask Alignment Marks. These marks were placed at the ends of each row of each submask. They assist with the accurate alignment of each consecutive processing step.

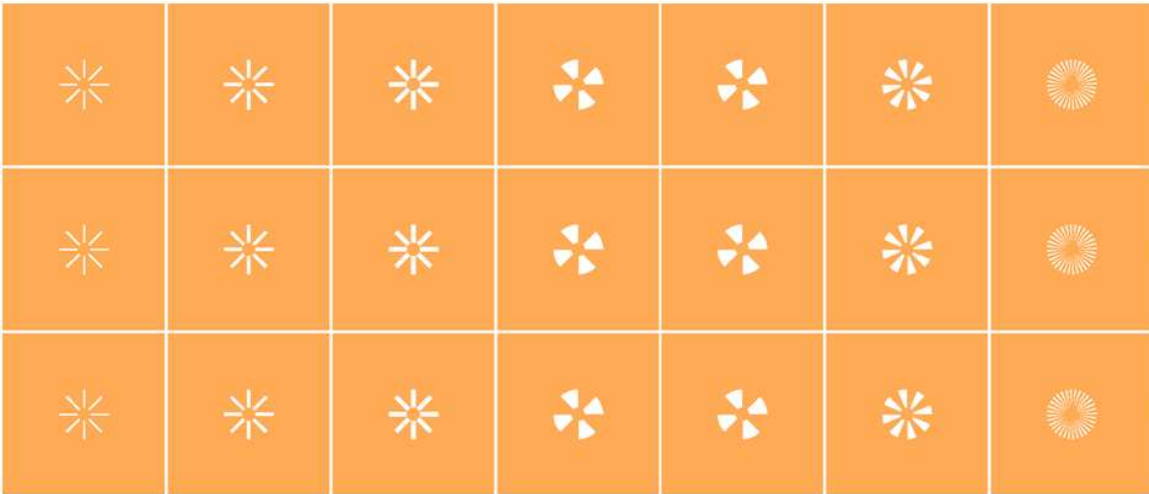


Figure B.3: Submask 1 - Magnet Deposit. Pattern for depositing nickel for the rotor magnets. Columns from left to right are:  $80\ \mu m$  rectangular arm rotors,  $120\ \mu m$  rectangular arm rotors,  $160\ \mu m$  rectangular arm rotors, two columns of 4-arm toroidal rotors, 8-arm toroidal rotors, and 32-arm toroidal rotors.

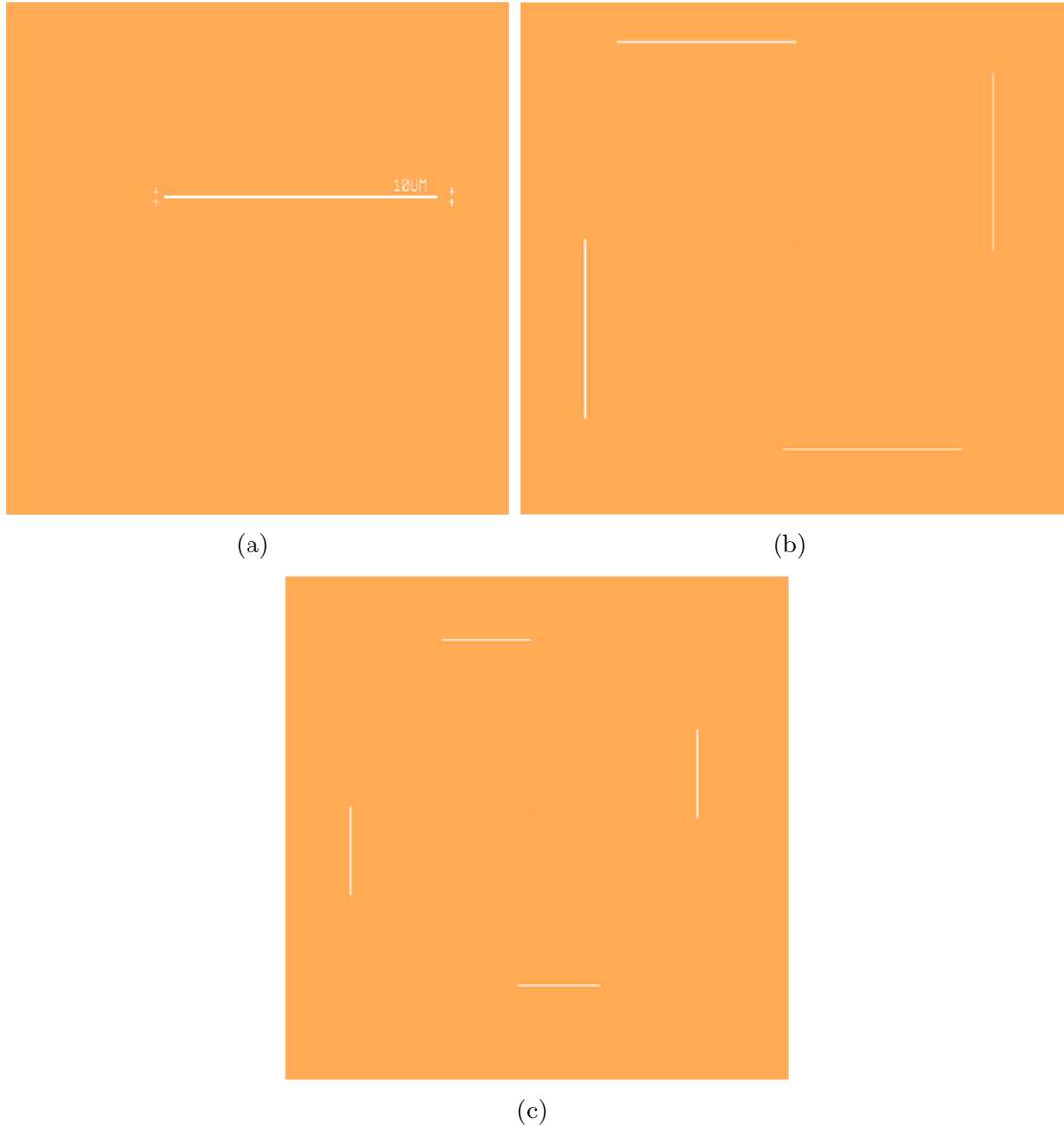


Figure B.4: Submask 2 - Coil Runner Etch and Deposit. Pattern for etching troughs for the coil runner and depositing gold into it. Given that an image of the entire slide does not provide enough resolution to view the details of the runners, zoomed in views are provided of each variation on the slide. (a) Represents the runner for the concentric coil (columns 1 and 2 of the mask), (b) represents the 12-turn arrayed angled runners (columns 3 and 4) and (c) represents the 6-turn arrayed angled runners (columns 5, 6 and 7).

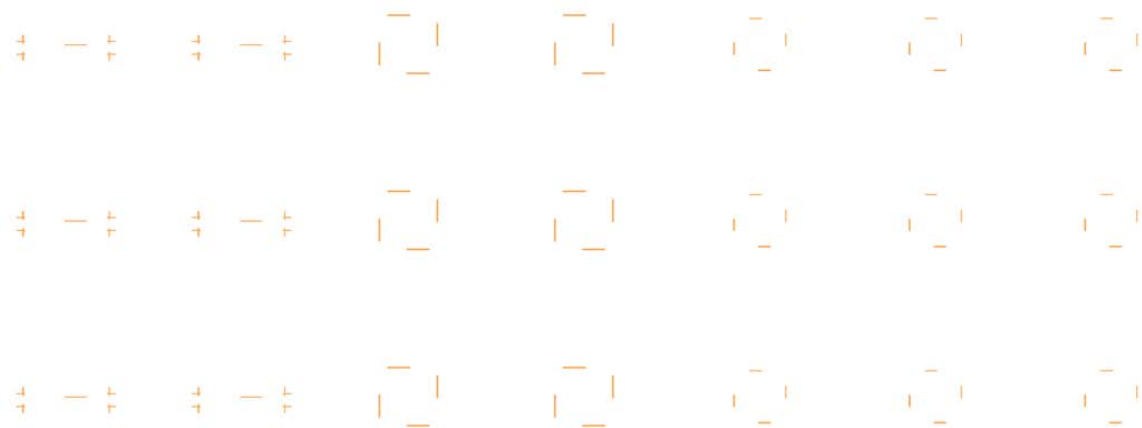
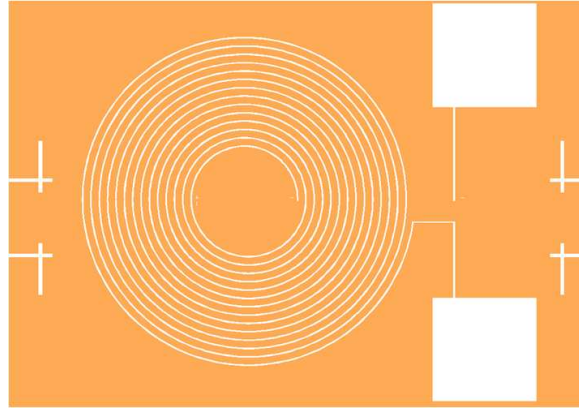


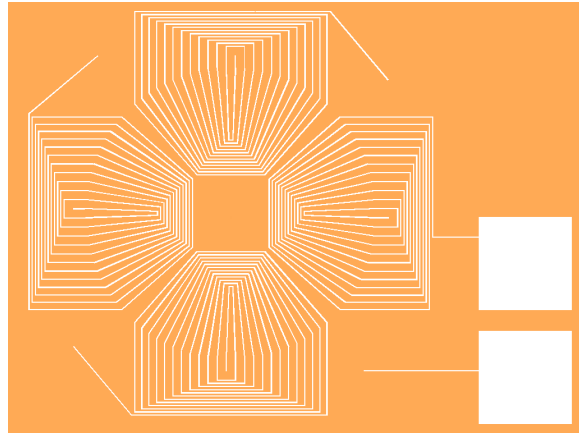
Figure B.5: Submask 3 - Coil Nitride Etch. Pattern for etching the silicon nitride from everywhere it is not needed and leaving a layer to separate the runner from the coil.



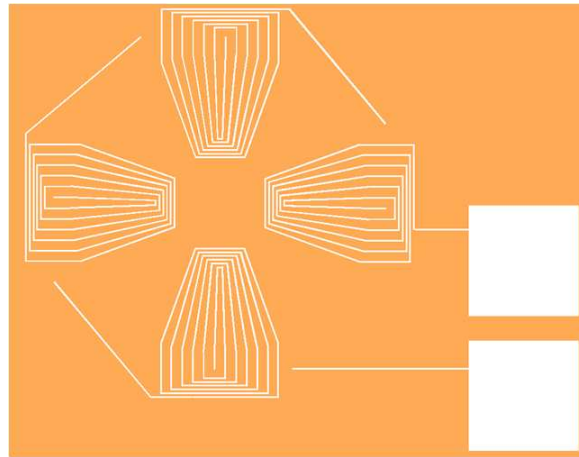
Figure B.6: Submask 3 - Zoomed in Nitride Etch Holes. Small holes were made into the nitride protective layer to provide vias between the coil and the runner.



(a)



(b)



(c)

Figure B.7: Submask 4 - Final Coil Deposit. Pattern for depositing the coil and pads for each stator coil. Given that an image of the entire slide does not provide enough resolution to view the details of the coils, zoomed in views are provided of each variation on the slide. (a) Represents the the concentric coil (columns 1 and 2 of the mask), (b) represents the 12-turn arrayed angled coils (columns 3 and 4) and (c) represents the 6-turn arrayed angled coils (columns 5, 6 and 7).



Figure B.8: Submask 5 - Magnet Nickel Plating Seed Etch. Pattern for etching the seed off of the rotor magnet slide. This mask was not used in this effort because the seed layer was not expected to significantly influence the output of the generator.

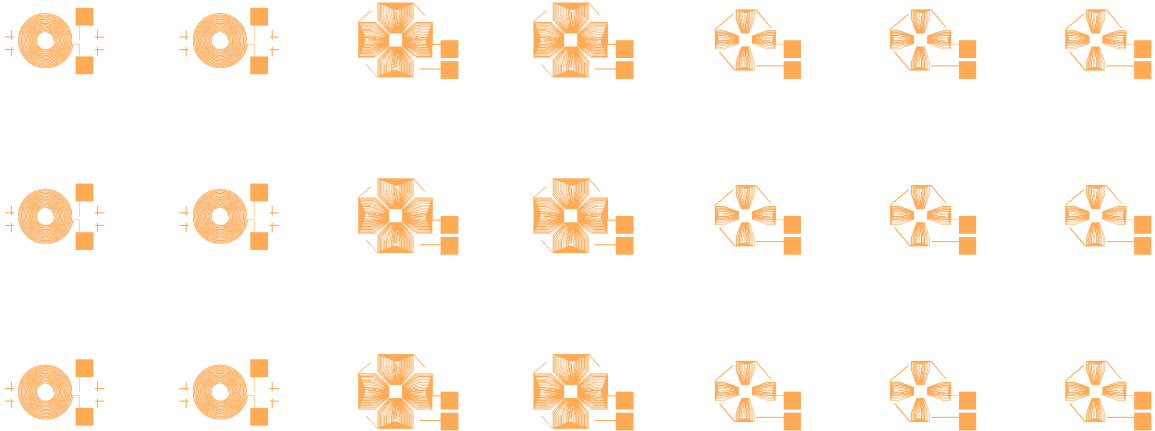


Figure B.9: Submask 6 - Coil Plating Seed Etch. Pattern for etching the seed off of the stator coil slide should electroplating be used for depositing the coil metal. This mask was not used in this effort because the gold was evaporated and not electroplated.

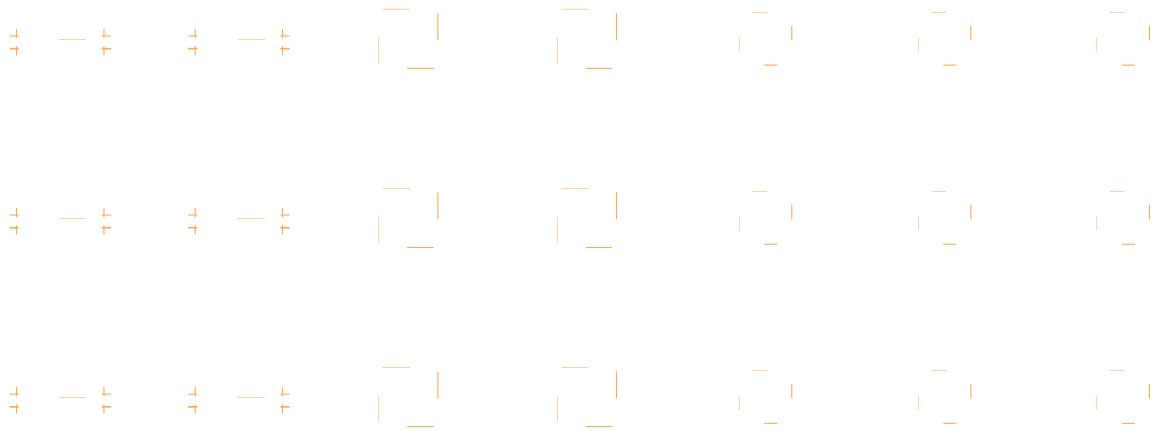


Figure B.10: Submask 7 - Runner Plating Seed Etch. Pattern for etching the seed off of the stator coil slide should electroplating be used for depositing the coil runner. This mask was not used in this effort because the gold was evaporated and not electroplated.

## *Appendix C. Fabrication Methods*

This appendix provides the process followers and input parameters used for the fabrication of the micro-generator as presented in this thesis.

Table C.1: Process for etching a trough for the runner and depositing metal.

Process Step – Trough Etch and Runner Deposit	Notes	Date/Time
<b>Inspect Wafer:</b> Note any defects	<u>Start Date</u> <u>Start Time</u>	
<b>Solvent Clean (if needed):</b> 20 sec acetone rinse at 500 rpm 20 sec isopropyl alcohol rinse at 500 rpm Dry with nitrogen at 500 rpm Dry wafer with nitrogen on clean texwipes		
<b>Dehydration Bake:</b> 1 min 110°C hot plate bake		
<b>1818 Application:</b> Flood wafer with 1818 5 sec Spread at 500 rpm 30 sec Spin at 4,000 rpm 75 sec at 110°C Cool for a minimum of 2 minutes to allow photoresist to set Inspect wafer under microscope and look for <input type="checkbox"/> Bubbles <input type="checkbox"/> Even Application		
<b>Expose 1818:</b> Align to runner mask 3.5 sec timed exposure on EVG 620		
<b>1818 Develop:</b> 30 sec develop with 351 Developer at 500 rpm 30 sec DI rinse at 500 rpm Dry with nitrogen at 500 rpm Dry wafer with nitrogen on clean texwipes		
<b>Asher Descum:</b> 10 min, 75 W, LFE Barrel Asher		
<b>Profilometer Measurement:</b> Measure photoresist step height Top:                      Center:                      Bottom:		
<b>RIE Trough:</b> RIE to desired depth and verify by comparing to original profilometer measurements (done at AFRL/Ry)		
<b>Metal Deposition:</b> Evaporate desired metals		
<b>Lift Off Excess Metal and Clean off PR:</b> Place devices in vibrating bath of acetone until all excess gold is removed Acetone/methanol rinse at 500 rpm Dry with nitrogen and 110°C, 2 min Inspect wafer under microscope and look for <input type="checkbox"/> Desired Metal Coverage <input type="checkbox"/> Good Adhesion <input type="checkbox"/> Clean Devices Around Metal Repeat as necessary until surface appears clean and free of excess PR and gold		

Table C.2: Process for depositing the barrier nitride and patterning it.

Process Step – Silicon Nitride Deposit and Etch	Notes	Date/Time
<b>Inspect Wafer:</b> Note any defects	<u>Start Date</u>	
	<u>Start Time</u>	
<b>Solvent Clean (if needed):</b> 20 sec acetone rinse at 500 rpm 20 sec isopropyl alcohol rinse at 500 rpm Dry with nitrogen at 500 rpm Dry wafer with nitrogen on clean texwipes		
<b>Dehydration Bake:</b> 1 min 110°C hot plate bake		
<b>Asher Descum:</b> 10 min, 75 W, LFE Barrel Asher to ensure clean surface SiN		
<b>Silicon Nitride Deposit:</b> PECVD nitride to 1000 Angstroms or desired thickness (AFRL/Ry)		
<b>Solvent Clean:</b> 20 sec acetone rinse at 500 rpm 20 sec isopropyl alcohol rinse at 500 rpm Dry with nitrogen at 500 rpm Dry wafer with nitrogen on clean texwipes		
<b>Dehydration Bake:</b> 1 min 110°C hot plate bake		
<b>1818 Application:</b> Flood wafer with 1818 5 sec Spread at 500 rpm 30 sec Spin at 4,000 rpm 75 sec at 110°C Cool for a minimum of 2 minutes to allow photoresist to set Inspect wafer under microscope and look for <input type="checkbox"/> Bubbles <input type="checkbox"/> Even Application		
<b>Expose 1818:</b> Align to nitride mask 3.5 sec timed exposure on EVG 620		
<b>1818 Develop:</b> 30 sec develop with 351 Developer at 500 rpm 30 sec DI rinse at 500 rpm Dry with nitrogen at 500 rpm Dry wafer with nitrogen on clean texwipes		
<b>Asher Descum:</b> 10 min, 75 W, LFE Barrel Asher		
<b>RIE Excess Nitride:</b> RIE all excess and verify nitride thickness with profilometer (AFRL/Ry)		
<b>Clean off PR:</b> Acetone/methanol rinse at 500 rpm Dry with nitrogen and 110°C, 2 min Inspect wafer under microscope and look for <input type="checkbox"/> Desired Nitride Pattern		

Table C.3: Process for depositing the metal that forms the coil and pads.

Process Step – Final Gold Coil Deposit	Notes	Date/Time
<b>Inspect Wafer:</b> Note any defects	<u>Start Date</u> <u>Start Time</u>	
<b>Solvent Clean (if needed):</b> 20 sec acetone rinse at 500 rpm 20 sec isopropyl alcohol rinse at 500 rpm Dry with nitrogen at 500 rpm Dry wafer with nitrogen on clean texwipes		
<b>Dehydration Bake:</b> 1 min 110°C hot plate bake		
<b>Triple LOR Application:</b> Repeat 3X Flood wafer with LOR3A 10 sec Spread at 500 rpm 30 sec Spin at 2,000 rpm 2 min at 170°C Cool for a minimum of 2 minutes to allow photoresist to set Inspect wafer under microscope and look for <input type="checkbox"/> Bubbles <input type="checkbox"/> Even Application		
<b>1818 Application:</b> Flood wafer with 1818 5 sec Spread at 500 rpm 30 sec Spin at 4,000 rpm 2 min at 110°C Cool for a minimum of 2 minutes to allow photoresist to set Inspect wafer under microscope and look for <input type="checkbox"/> Bubbles <input type="checkbox"/> Even Application		
<b>Expose 1818:</b> Align to final coil mask 4.1 sec timed exposure on EVG 620		
<b>1818 / LOR Develop:</b> 75 sec develop with LDD26 at 500 rpm Puddle for 10 sec at beginning and middle of development 30 sec DI rinse at 500 rpm Dry with nitrogen at 500 rpm Dry wafer with nitrogen on clean texwipes		
<b>Inspect Resist:</b> Inspect photoresist under microscope If exposed areas still show LOR, repeat development step in 10 sec increments (drying and inspecting after each)		
<b>Asher Descum:</b> 10 min, 75 W, LFE Barrel Asher		
<b>Metal Deposition:</b> Evaporate desired metals (up to 1 micron)		
<b>Lift Off Excess Metal and Clean off PR and LOR:</b> Heat 1165 stripper to 90°C (Hot plate at ~170°C) Press a strip of scotch tape across entire surface of sample and remove the majority of excess metal Place devices in vibrating bath of acetone until all excess gold is removed Acetone/methanol rinse at 500 rpm 15 min soak in 1165 20 sec DI rinse 500 rpm Acetone/methanol rinse at 500rpm Dry with nitrogen and 110°C, 2 min Inspect wafer under microscope and look for <input type="checkbox"/> Desired Metal Coverage <input type="checkbox"/> Good Adhesion Repeat as necessary until surface appears clean and free of excess LOR		

Table C.4: Process for 24  $\mu\text{m}$  Thick AZ P4620 Photoresist and Electroplating Nickel to Desired Thickness

Process Step – Electroplating Nickel Rotors	Notes	Date/Time
<b>Inspect Wafer:</b> Note any defects Solvent clean only if needed	<u>Start Date</u> <u>Start Time</u>	
<b>Solvent Clean (if needed):</b> 20 sec acetone rinse at 500 rpm 20 sec isopropyl alcohol rinse at 500 rpm Dry with nitrogen at 500 rpm Dry wafer with nitrogen on clean texwipes		
<b>Dehydration Bake:</b> 1 min 110°C hot plate bake		
<b>1st AZ P4620 Application:</b> Flood wafer with AZ P4620 3 sec Spread at 300 rpm 60 sec Spin at 1900 rpm, Film thickness is $\sim 10\mu\text{m}$ Clean edges with Acetone on swab 85 sec 110°C Hot Plate Bake		
<b>2nd AZ P4620 Application:</b> Flood wafer with AZ P4620 again 3 sec Spread at 300 rpm 60 sec Spin at 1600 rpm, additional film thickness is $\sim 14\mu\text{m}$ for a total of $\sim 24\mu\text{m}$ . Clean edges with Acetone on swab 165 sec 110°C Hot Plate Bake		
<b>Expose with Mask:</b> Align Mask 680 mJ/cm <sup>2</sup> Fixed Dose Exposure using AFIT EVG 620		
<b>Develop:</b> 5 sec wet wafer with DI water at 250 rpm 210 sec develop with AZ 400K:DI water (1:4) at 250 rpm 30 sec DI water rinse at 250 rpm 20 secs Spin dry at 4000 rpm Dry back of wafer with nitrogen on clean texwipes		
<b>Inspect Resist:</b> Inspect photoresist under microscope		
<b>Profilometer Measurement:</b> Measure photoresist step height Top:                      Center:                      Bottom:		
<b>Electroplate Nickel (AFRL/RV Cleanroom):</b> Clean off electrode contacts Calculate exposed seed surface area Calculate current required for current densities of 182 mA/cm <sup>2</sup> Forward and 121 mA/cm <sup>2</sup> Reverse. This provides a deposition rate of 0.4 $\mu\text{m}/\text{min}$ . Calculate Amp-minutes required for desired thickness. Input parameters into Dynatronix power supply. Run electroplating bath.		
<b>Profilometer Measurement:</b> Measure new step height and verify thickness of deposit Top:                      Center:                      Bottom:		
<b>Clean off AZ P4620</b> 2 minute soak in Acetone 30 sec rinse with Methanol at 3000 rpm 10 sec dry with Nitrogen at 3000 rpm 2 minute soak in AZ 400K Developer 30 sec rinse in DI water at 500 rpm 10 sec dry with Nitrogen at 3000 rpm		

## Appendix D. Experimental Raw Data

This appendix contains the measurements and raw data collected during this effort. Figure D.1 provides the referencing scheme used to discuss the results of the measurements and testing of the rotors whereas Figure D.2 provides the referencing scheme used to discuss the coils. Only two rows were fabricated on each slide sample due to the edge beading of the PR.

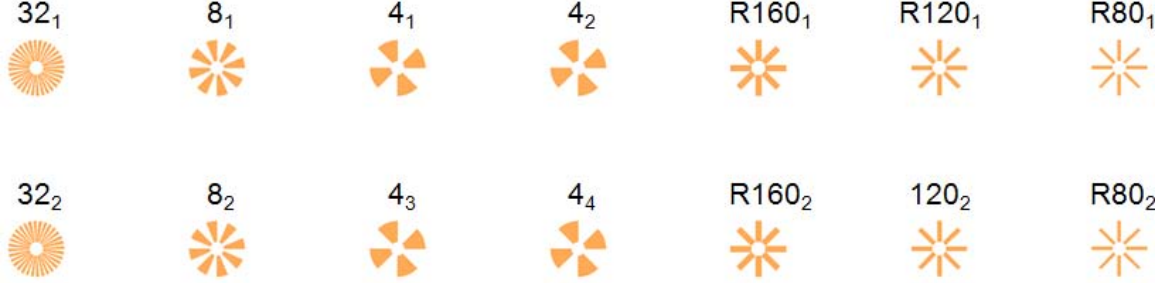


Figure D.1: Rotor Referencing Scheme. With 32 Arm Toroidal Rotors on the left, the numbering scheme is as above. (32  $\rightarrow$  32 Arm Toroidal; 8  $\rightarrow$  8 Arm Toroidal; 4  $\rightarrow$  4 Arm Toroidal; R160  $\rightarrow$  160  $\mu\text{m}$  Rectangular Arm; R120  $\rightarrow$  120  $\mu\text{m}$  Rectangular Arm; and R80  $\rightarrow$  80  $\mu\text{m}$  Rectangular Arm.)



Figure D.2: Coil Referencing Scheme. With the Single Concentric Coils on the left, the numbering scheme is as above. (CC  $\rightarrow$  Single Concentric; 12AC  $\rightarrow$  12-Turn Angular; and 6AC  $\rightarrow$  6-Turn Angular.)

Table D.1: Profilometer Measurements of Rotors. The minimum thickness and the max thickness are presented to illustrate the variations in thickness observed.

<b>SH-M3</b>	Height ( $\mu\text{m}$ )	
	Min	Max
32 <sub>1</sub>	8	
32 <sub>2</sub>	11	14
8 <sub>1</sub>	9	10
8 <sub>2</sub>	13	14
4 <sub>1</sub>	7	8
4 <sub>2</sub>	7	8
4 <sub>3</sub>	10	
4 <sub>4</sub>	8	9
R160 <sub>1</sub>	8	9
R160 <sub>2</sub>	8.5	9.5
R120 <sub>1</sub>	8	10
R120 <sub>2</sub>	10	11
R80 <sub>1</sub>	7	9
R80 <sub>2</sub>	11	13

<b>SH-M4</b>	Height ( $\mu\text{m}$ )	
	Min	Max
32 <sub>1</sub>	10	
32 <sub>2</sub>		
8 <sub>1</sub>	13	14
8 <sub>2</sub>		
4 <sub>1</sub>	14	16
4 <sub>2</sub>	14	17
4 <sub>3</sub>		
4 <sub>4</sub>		
R160 <sub>1</sub>	14	17
R160 <sub>2</sub>		
R120 <sub>1</sub>	15	18
R120 <sub>2</sub>		
R80 <sub>1</sub>	12	18
R80 <sub>2</sub>		

Table D.2: Resistance measurements of coils and associated notes about each. Those highlighted appear to be well fabricated and were used to calculate the average resistance for each type of coil on each sample.

0.5 $\mu\text{m}$ Thick Coils				0.75 $\mu\text{m}$ Thick Coils				1 $\mu\text{m}$ Thick Coils			
C9				C8				C7			
Type	#	R ( $\Omega$ )	Notes	#	R ( $\Omega$ )	Notes		#	R ( $\Omega$ )	Notes	
CC	1	62000	Good	1	248.4	Good		1	85.9	Narrowing of coils	
	2	44000	Good	2	230.9	Good		2	62	Wider Coils	
	3	63000	One Small Cut	3	173.12	Good		3	78.8	some lift off and narrowed	
	4	62000	One Small Cut	4	160.8	Good		4	164	cut in half	
12AC	1	209	Really Good	1	7180	break		1	52.8	coils broken in 2 places	
	2	1636	Really Good	2	6600	short		2	34.2	Looks good	
	3	65000	Looks Good	3	104.7	Good		3	36.7	cut off part	
	4	65000	Looks Good	4	136.2	lift off		4	33.6	a short and liftoff	
6AC	1	58800	Looks Good	1	7000	nitride off		1	42.4	one short	
	2	65000	Looks Good	2	9000	nitride off		2	41.3	looks good	
	3	2.96	Pads Connected	3	GONE			3	Gone		
	4	67000	Looks Good	4	45.5	nitride off		4	27.7	looks good	
	5	75000	Looks Good	5	43.8	nitride off		5	27.6	maybe short	
	6	GONE	No Pads	6	50.1	nitride off		6	27.2	short	
C6				C5				C10			
Coil	1	7150	line cut	1	6803	Good		1	76.2	Good	
	2	25500	multiple cuts	2	4062	Good		2	2.87	All Gold	
	3	GONE		3	4920	broken and narrowing		3	41	okay	
	4	3000	multiple cuts	4	113.4	Good		4	38.57	Huge Pad	
12-Turn	1	10262	Good	1	852	one cut		1		All Gold	
	2	1064	barely overlapped	2	645	Good/debris on runner		2		All Gold	
	3	239.7	Bridging	3	50.6	small overlaps		3		All Gold	
	4	2000	bridging/cuts	4	50.6	line issues		4		All Gold	
6-Turn	1	13750	Looks Good	1	51.77	Good		1		All Gold	
	2	1230	Looks Good	2	1020	debris on runner		2		All Gold	
	3	45000	Very Thin Lines	3	6600	good		3	75.3	Partial Overlap/Nitride Missing	
	4	1815	line cuts	4	36.3	Good		4		All Gold	
	5	3500	barely overlapped	5	45.6	Good		5		All Gold	
	6	13000	lines lifted off	6	55.1	Good		6		All Gold	

Table D.3: Calculation of predicted resistance of coil should all thicknesses and widths match up to design. Length was calculated using L-Edit.

Design	Runner Length ( $\mu\text{m}$ )	Coil Length ( $\mu\text{m}$ )	Total Length ( $\mu\text{m}$ )	Width ( $\mu\text{m}$ )	Thickness ( $\mu\text{m}$ )	Resistance ( $\Omega$ )
				$A = W \times T$		$R = \frac{\rho L}{A}$
Concentric	760	47107.4316	47867.432	10	1	106
12-Turn	2972.2	110497.1429	113469.34	10	1	251
6-Turn	1529	42024.4321	43553.432	10	1	96
Concentric	760	47107.4316	47867.432	10	0.75	141
12-Turn	2972.2	110497.1429	113469.34	10	0.75	335
6-Turn	1529	42024.4321	43553.432	10	0.75	129
Concentric	760	47107.4316	47867.432	10	0.5	212
12-Turn	2972.2	110497.1429	113469.34	10	0.5	502
6-Turn	1529	42024.4321	43553.432	10	0.5	193

## Bibliography

1. R. C. Johnson, "Energy harvesting matures with growth of wireless sensor networks," *Electronic Engineering Times*, p. 17, December 3 2007.
2. S. Rodgers and J. Sniegowski, "New five-level layering process pioneered by sandia promises more reliable, complex micromachines." Sandia National Laboratories, September 1999. Available at <http://www.sandia.gov/media/NewsRel/NR1999/layer.htm>.
3. G. T. A. Kovaks, *Micromachined Transducers Sourcebook*. WCB/McGraw-Hill, 1998.
4. K. Fu, A. J. Knobloch, F. C. Martinez, D. C. Walther, C. Fernandez-Pello, A. P. Pisano, D. Liepmann, K. Miyaska, and K. Maurta, "Design and experimental results of small-scale rotary engines," in *Proceedings of 2001 ASME International Mechanical Engineering Congress and Exposition*, November 2001.
5. A. J. Sprecher, "Microfluidic power generation," Master's thesis, Air Force Institute of Technology, 2008.
6. I. Buchmann, "Battery university," February 2007. Available at <http://www.batteryuniversity.com>.
7. Anonymous, "The reality behind Moore's law," *Cyber Aspect*, January 2008. Available at [http://www.cyber-aspect.com/features/feature\\_article.asp?art=104](http://www.cyber-aspect.com/features/feature_article.asp?art=104).
8. Anonymous, "In search of the perfect battery," *The Economist*, March 6 2008. Available at [http://www.economist.com/displaystory.cfm?story\\_id=10789409](http://www.economist.com/displaystory.cfm?story_id=10789409).
9. B. S. Lee, P. J. Shih, J. J. He, W. P. Shih, and W. J. Wu, "A study of implantable power harvesting transducers," in *Proceedings of SPIE - The International Society for Optical Engineering, Sensor Systems and Networks: Phenomena, Technology, and Applications for NDE and Health Monitoring*, vol. 6530, 2007.
10. C. B. Williams and R. B. Yates, "Analysis of a micro-electric generator for microsystems," *Sensors and Actuators A: Physical*, vol. 52, no. 1-3, pp. 8-11, 1996.
11. O. Cugat, "Magnetic micro-actuators and systems (MAGMAS)," *IEEE Transactions on Magnetics*, vol. 39, no. 6, pp. 3607-3612, 2003.
12. D. P. Arnold, "Review of microscale magnetic power generation," *IEEE Transactions on Magnetics*, vol. 43, no. 11, p. 3940(12), 2007.
13. E. Lefeuvre, A. Badel, C. Richard, L. Petit, and D. Guyomar, "Optimization of piezoelectric electrical generators powered by random vibrations," in *Dans Symposium on Design, Test, Integration and Packaging (DTIP) of MEMS/MOEMS*, 2006.

14. P. D. Mitcheson, T. C. Green, E. M. Yeatman, and A. S. Holmes, "Architectures for vibration-driven micropower generators," *Journal of Microelectromechanical Systems*, vol. 13, no. 3, pp. 429–440, 2004.
15. B. H. Stark, P. D. Mitcheson, P. Miao, T. C. Green, E. M. Yeatman, and A. S. Holmes, "Converter circuit design, semiconductor device selection and analysis of parasitics for micropower electrostatic generators," *IEEE Transactions on Power Electronics*, vol. 21, no. 1, pp. 27–37, 2006.
16. G. L. Pollack and D. R. Stump, *Electrictromagnetism*. Addison Wesley, 2002.
17. P. Kiamah, *Electrical Equipment Handbook*. McGraw-Hill Higher Education, 2003.
18. P. S. Neelakanta, *Handbook of Electromagnetic Materials*. CRC Press, 1995.
19. W. Brown, *Handbook of Chemistry and Physics*. McGraw-Hill, 1958.
20. T. C. Leichle, M. V. Arx, and M. G. Allen, "A micromachined resonant magnetic field sensor," *14th IEEE International Conference on Micro Electro Mechanical Systems*, pp. 274–277, 2001.
21. G. D. Bari, "Nickel plating," *ASM Handbook*, vol. 5, 1994.
22. D. R. Lide, ed., *CRC Handbook of Chemistry and Physics*. CRC Press, 2003.
23. J. Dean, ed., *Lange's Handbook of Chemistry (15th Edition)*. McGraw-Hill, 1999.
24. G. S. May and S. M. Sze, *Fundamentals of Semiconductor Fabrication*. John Wiley and Sons, Inc, 2004.
25. "AZ P4000 Thick Film Photoresist Datasheet." AZ Electronic Materials, 2005. Available at [http://www.az-em.com/PDFs/p4000/az\\_p4000.pdf](http://www.az-em.com/PDFs/p4000/az_p4000.pdf).
26. A. Ciszewski, S. Posluszny, G. Milczarek, and M. Baraniak, "Effects of saccharin and quaternary ammonium chlorides on the electrodeposition of nickel from a watts-type electrolyte," *Surface and Coatings Technology*, vol. 183, pp. 127–133, May 2004.
27. M. Williams, "Electroplating lab notebook." AFRL/RD Devices Cleanroom, 2004.
28. "LOR and PMGI Resist Datasheet." MicroChem, 2008. Available at <http://www.microchem.com>.
29. A. Fitzgerald, C. Kingsley, and S. D. Umans, *Electric Machinery - Sixth Edition*. McGraw-Hill Handbooks, 2003.
30. Z. Turgut, "Electromagnetics discussion," January 2007. Air Force Research Lab/Propulsion Directorate, Wright-Patterson Air Force Base.

## *Vita*

James H. Shields was born in Athens, GA in 1979 and raised for the majority of his youth in Chickamauga, GA. He graduated from Gordon Lee High School in 1997 and began his undergraduate program in Computer Engineering at Brigham Young University (BYU) in Provo, UT on an Air Force ROTC scholarship that same year. He put his studies on hold from 1998 to 2000 to serve a two year mission in northern Argentina for The Church of Jesus Christ of Latter-Day Saints. Upon returning from his mission, James picked up his studies at BYU and received his BS in Computer Engineering and a commission into the United States Air Force in 2003. His first assignment was to the Air Force Research Lab, Human Effectiveness Directorate in Mesa, AZ where he was a program manager and research engineer for the Intelligence, Surveillance, and Reconnaissance Training Research Group. In 2007 he began his Masters program in Microelectronics and MEMS at the Air Force Institute of Technology. Upon graduation in March 2009, James will be working with the Nano/Bio Technology Branch at the Air Force Research Lab, Materials Directorate.

Permanent address: 2950 Hobson Way  
Air Force Institute of Technology  
Wright-Patterson AFB, OH 45433

REPORT DOCUMENTATION PAGE					Form Approved OMB No. 0704-0188	
<p>The public reporting burden for this collection of information is estimated to average 1 hour per response, including the time for reviewing instructions, searching existing data sources, gathering and maintaining the data needed, and completing and reviewing the collection of information. Send comments regarding this burden estimate or any other aspect of this collection of information, including suggestions for reducing this burden to Department of Defense, Washington Headquarters Services, Directorate for Information Operations and Reports (0704-0188), 1215 Jefferson Davis Highway, Suite 1204, Arlington, VA 22202-4302. Respondents should be aware that notwithstanding any other provision of law, no person shall be subject to any penalty for failing to comply with a collection of information if it does not display a currently valid OMB control number. PLEASE DO NOT RETURN YOUR FORM TO THE ABOVE ADDRESS.</p>						
1. REPORT DATE (DD-MM-YYYY)		2. REPORT TYPE		3. DATES COVERED (From — To)		
26-03-2009		Master's Thesis		Sept 2007 — Mar 2009		
4. TITLE AND SUBTITLE  Power Generation by Harvesting Ambient Energy with a Micro-Electromagnetic Generator				5a. CONTRACT NUMBER		
				5b. GRANT NUMBER		
				5c. PROGRAM ELEMENT NUMBER		
6. AUTHOR(S)  James H. Shields, Capt, USAF				5d. PROJECT NUMBER  ENG08-180		
				5e. TASK NUMBER		
				5f. WORK UNIT NUMBER		
7. PERFORMING ORGANIZATION NAME(S) AND ADDRESS(ES) Air Force Institute of Technology Graduate School of Engineering and Management (AFIT/EN) 2950 Hobson Way WPAFB OH 45433-7765				8. PERFORMING ORGANIZATION REPORT NUMBER  AFIT/GE/ENG/09-42		
9. SPONSORING / MONITORING AGENCY NAME(S) AND ADDRESS(ES) Nancy Kelley-Loughnane, PhD Applied Biotechnology Branch Area B, Bldg 837, 2729 R Street Wright Patterson Air Force Base, OH 45433-5707 (Nancy.Kelley-Loughnane@wpafb.af.mil, (937) 904-9498)				10. SPONSOR/MONITOR'S ACRONYM(S)  711 HPW/RHPB		
				11. SPONSOR/MONITOR'S REPORT NUMBER(S)		
12. DISTRIBUTION / AVAILABILITY STATEMENT  Approval for public release; distribution is unlimited.						
13. SUPPLEMENTARY NOTES						
14. ABSTRACT This thesis investigated the potential power output of micro-electromagnetic generators fabricated using typical microfabrication materials and techniques. The design was intended to eliminate the need for batteries in bio-implanted or remote electronic devices. Such a micro-generator could harvest ambient energy and power such devices indefinitely. Using electromagnetic theory, designs for the magnet's stator coil and rotor magnets were optimized to produce maximum current density. A method for overlaying two evaporated gold wires was devised and successfully fabricated in order to avoid side-wall thinning of the conductive coils. Once fabricated, the ferromagnetic nickel rotors were magnetized with an electromagnet. Testing of the magnets showed that the nickel rotors were able to be highly magnetized when placed near a strong field, but, upon removal from the field, the magnetization quickly dissipated. It was determined that the coercivity of electroplated nickel was too low for the rotor magnets to retain a field for any appreciable amount of time. Testing of the micro-generator revealed that power output did not exceed 2 nA, thus nickel does not maintain the flux density required for such a generator and different materials should be investigated.						
15. SUBJECT TERMS  Microelectromechanical Systems (MEMS), Microfabrication, Energy Harvesting, Electromagnetic Generator, Microgenerators, Power Generation						
16. SECURITY CLASSIFICATION OF:			17. LIMITATION OF ABSTRACT	18. NUMBER OF PAGES	19a. NAME OF RESPONSIBLE PERSON	
a. REPORT	b. ABSTRACT	c. THIS PAGE			Lavern Starman, Maj, USAF	
U	U	U	UU	116	19b. TELEPHONE NUMBER (include area code) (937)255-3636 ext4618; Lavern.Starman@afit.edu	